Modelling and Characterization of Porous Fabric Reinforcement Permeability and Compressibility in Composite Materials Manufacturing

by

Deniz Sayınbaş

A dissertation submitted to the
Graduate School of Sciences and Engineering
in Partial Fulfillment of the Requirements for
the Degree of

Master of Science
in
Mechanical Engineering

September 2022

Modelling and Characterization of Porous Fabric Reinforcement Permeability and Compressibility in Composite Materials Manufacturing

Koç University

Graduate School of Science and Engineering

This is to certify that I have examined this copy of a master's thesis by

Deniz Sayınbaş

and have found that it is complete and satisfactory in all respects,

and that any and all revisions required by the final

examining committee have been made

Committee Members:

_____

Prof. Murat Sözer (Advisor)

_____

Prof. Metin Muradoglu

_____

Assoc. Prof. Barış Çağlar

Date: _____

ABSTRACT

Modelling and Characterization of Porous Fabric Reinforcement Permeability and Compressibility in Composite Materials Manufacturing

Deniz Sayınbaş

Master of Science in Mechanical Engineering

September 2022

Through-thickness permeability of an E-glass non-crimp fabric (NCF) was modeled and characterized experimentally. Characterization setup used previously in various studies was modified. The number of layers used in an experiment was reduced and a new approach was designed to adjust the fiber volume fraction of the fabric preform. In-plane permeability components of a biaxial fabric was characterized by 2D (radial) flow experiment. Scatter between experimental results was observed similar to previous results in literature. Compressibility of a NCF was characterized using a vacuum infusion setup, pressure regulator and structured light scanning (SLS) system. Compared to previous study in our research lab, a new experimental SLS schedule was designed and tested for compressibility characterization. The accuracy of a single SLS measurement was low, however it was shown that repeated measurements had a better accuracy which made our SLS system suitable to monitor the part thickness variation with time. The variation of fiber volume fraction within the porous tows of a woven fabric was numerically investigated using ANSYS Fluent. In general, permeability of a tow assembly in a unit cell with spatially varying fiber volume fraction was lower than uniformly distributed fiber volume fraction. A dual scale model was prepared and verified by comparing its results with another study and its case studies available in the literature. Our model allows accounting any local variation in fiber volume fraction. This thesis contributes to the literature by presenting a new approach in modelling of fabric reinforcement permeability and compressibility which accounts for the non-uniformity of fiber distribution and the local variation of fiber volume fraction. Thus, it can be a guide to an appropriate model for different levels of fiber nesting of compacted fabric layers, as observed in composite manufacturing processes such as resin transfer molding and vacuum infusion.

ÖZET

Kompozit Malzeme İmalatında Gözenekli Kumaş Takviye Geçirgenliği ve Sıkıştırılabilirliğinin Modellenmesi ve Karakterizasyonu

Deniz Sayınbaş

Makine Mühendisliği, Yüksek Lisans

Eylül 2022

Kıvrımsız E-cam elyafın kalınlık yönünde geçirgenliği modellendi ve deneysel olarak karakterize edildi. Daha önce çeşitli çalışmalarda kullanılmış kalınlık yönünde geçirgenlik deney düzeneği modifiye edildi. Deneyde kullanılan katman sayısı düşürüldü ve numunenin elyaf hacim oranını değiştirmek için yeni bir yaklaşım tasarlandı. İki eksenli (biaxial) E-cam elyafın geçirgenlik komponentleri iki boyutlu (radyal) geçirgenlik deney düzeneği ile karakterize edildi. Deney sonuçları arasındaki değişkenlik literatürde olan çalışmalara benzer şekilde gözlemlendi. Kıvrımsız E-cam elyafın sıkıştırılabilirliği Vakum Destekli Reçine Transfer Kalıplama (VARTM) ve Yapısal Aydınlatma ile Tarama (Structural Light Scanning (SLS)) deney düzeneği kullanılarak karakterize edildi. Daha önce laboratuvarımızda yapılmış bir araştırmada kullanılandan farklı, yeni bir deneysel takvim tasarlandı ve sıkıştırılabilirlik karakterizasyonu için test edildi. Tek bir SLS ölçümünün doğruluğu düşüktü, ancak, tekrarlanan ölçümler arasındaki doğruluk yüksekti ve bu da SLS sisteminin parça kalınlığı ölçmek için uygun olabileceğini göstermektedir. Dokuma kumaşın gözenekli elyaf demetlerindeki elyaf hacim oranı varyasyonu numerik olarak ANSYS Fluent'te incelendi. Genel olarak, birim hücredeki fiber demetlerinin geçirgenliği, uzaysal olarak değişen elyaf hacim oranı kullanıldığında, sabit elyaf hacim oranı kullanılan modele göre daha düşük bulundu. İki dereceli akış modeli ANSYS Fluent'te hazırlandı ve literatürde olan bir çalışmanın sonuçları ile doğrulandı. Hazırladığımız model, elyaf hacim oranının lokal değişkenliğini kapsayacak şekilde geliştirildi. Bu çalışmanın kompozit araştırmalarına katkısı, kompozit üretiminde kullanılan kumaşların modellenmesine yönelik, kumaşlardaki elyaf hacim oranı değişkenliğini ve elyaf dağılımındaki değişkenliği hesaba katan bir modelleme yaklaşımının sunulmasıdır. Bu yüzden Reçine Transfer Kalıplama (RTM) ve vakum infüzyon gibi kompozit üretim süreçlerinde sıkıştırılmış elyaf katmanlarının farklı seviyelerde elyaf yerleştirmesi için uygun bir model için rehber alınabilir.

ACKNOWLEDGEMENTS

I would like to thank my advisor Prof. Murat Sözer. I am deeply indebted for his patience, support and guidance at every stage of my graduate study. I would like to extend my sincere thanks to Assoc. Prof. Barış Çağlar for his support and insightful comments during our meetings. I would also like to thank my thesis committee member Prof. Metin Muradoğlu for his participation with insightful comments.

I am also grateful to the staff of Graduate School of Sciences and Engineering and College of Engineering for their support.

I would like to thank to my colleagues, Hasan Çağlar and Nazlı Köroğlu for their support and patience. I would like to express my appreciation to Hakkı Kızılok, Bax Composites, Tarık E. and ASTAŞ Juki for their support.

Thanks should also go to my dear friends Mert Korkmaz, Seda Kuru, Burak Aykul, Melis Kardeş, Işıdan Şahin, Zeynep Şahin and Onur Karakuş for their supportive friendship and love.

Words cannot express my gratitude to my father Önder, my mother Pınar, my brother Ege, my grandmother Banu and also my dearest Yelda for their support, patience, positive influences, worthless love and keeping me motivated to achieve my goals.

I dedicate this work to the memory of my grandfather Tekin and grandmother Yıldız, who passed away last year.

TABLE OF CONTENTS

LIST OF FIGURES

LIST OF TABLES

Chapter 1:
INTRODUCTION TO COMPOSITE MATERIAL MANUFACTURING AND PROCESS MODELLING

1.1 Introduction

A composite material is produced by consolidating at least two distinct materials to give the composite favorable properties of constituents, suppressing the unfavorable ones. There are different types of manufacturing techniques for composite materials. They vary from labor-intensive hand layup, costly autoclave processing to high volume production processes such as injection molding. Selection of the manufacturing process is usually determined by the material properties and size of the part, cost and cycle time. Among these various composite manufacturing techniques, Liquid Composite Molding (LCM) is one of the most reliable processes for manufacturing of advanced composite parts [1-2]. Polymer composites consist of two main constituents, matrix and reinforcing components which have distinct functions. The main purpose of the matrix is to: (1) hold the fibers together and fix their orientation after it solidifies (i.e., is cured for thermosetting polymers), (2) provide effective load distribution transferring external forces to the fiber network, (3) contributes to normal and shear stress, (4) provide environmental durability protecting the reinforcement from harsh environmental conditions caused by humidity, sunlight, and service temperature. Although both thermoplastic and thermoset polymers can be used as a matrix component, in many cases thermoset polymers are preferred in LCM due to their lower viscosity which decreases the necessary pressure and power during resin injection/infusion. The main functions of the reinforcement component (usually glass, carbon or Kevlar) are the following: (1) supports the structural load, (2) decreases the thermal stresses on the composite providing controlled thermal expansion [1], (3) provides a superior level of specific stiffness (stiffness/density) and specific strength (strength/density) to the material. Compared to other manufacturing techniques where short fibers are used in which short fibers and liquid resin flow together as a suspension system, continuous fibers are usually preferred in LCM (placed in mold pre-injection/infusion). Although the use of continuous fibers limits the geometrical complexity of the part that is produced, it offers superior mechanical properties which can be utilized in load-bearing applications [1].

Many industries such as aerospace, automotive, sporting goods, marine and infrastructure have been replacing metal parts with fiber-reinforced polymer composites due to their superiority in specific strength and specific stiffness over metals [1]. However, compared to metals, composite material manufacturing suffers from non-repeatable and non-standardized manufacturing. The properties of the final product are highly affected by the inherent variability of the material (non-uniform fiber structure in a fabric roll) and, non-repeatable and labor-intensive operations such as fabric cutting, stacking and placement. Uncertainties in process parameters such as viscosity of liquid polymer, permeability of fiber preform, variation in the chemical composition of the material, fiber wash and preform deformation during impregnation contribute to non-repeatability of manufacturing. For many advanced applications in aerospace industry, tight tolerances in part dimensions and mechanical properties are required. The overall cost of composite manufacturing is higher than metal industry. Besides, manufacturing cycle time per part is longer. Engineers try to overcome these challenges too. Thus, it is important to optimize model and process parameters such as mold design, injection conditions and material selection to decrease the variabilities in dimensions and material properties [1-2]. LCM processes have the capability of producing high fiber volume fraction composites (by applied compaction) more consistently requiring lower initial investment compared to other composite manufacturing techniques [18]. However, the process must be accurately modelled to decrease the variability and uncertainties.

1.2 Liquid Composite Molding (LCM)

LCM is a family of composite manufacturing techniques. Essentially, a dry preform (a previously shaped fiber structure by cutting and stacking fabric layers on a tool surface) is placed in a mold, then a liquid thermoset resin is driven by an applied pressure gradient between inlet and ventilation gates to impregnate the dry preform. The most well-known LCM processes are Resin Transfer Molding (RTM) and Vacuum Assisted Resin Transfer Molding (VARTM which is a.k.a. Vacuum Infusion, VI). Fig. 1.1 and Fig. 1.2. illustrate the main steps of RTM and VARTM, respectively.

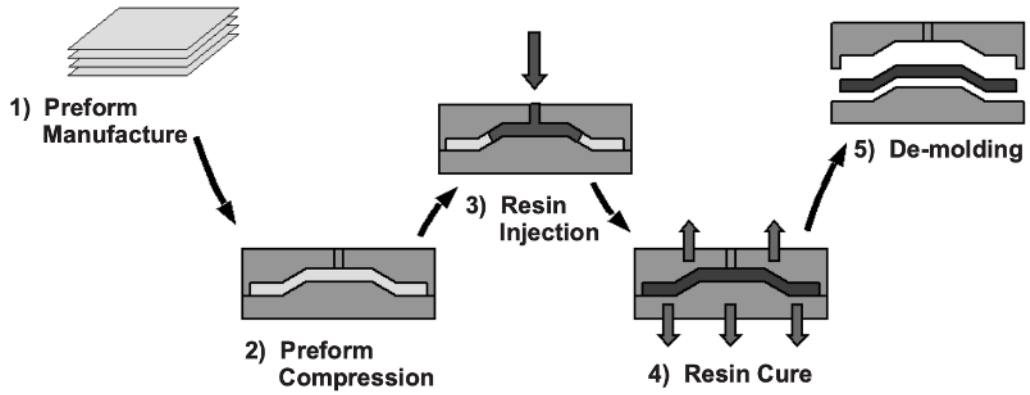

Figure 1.1 Illustration of the steps of Resin Transfer Molding (RTM) process [1]

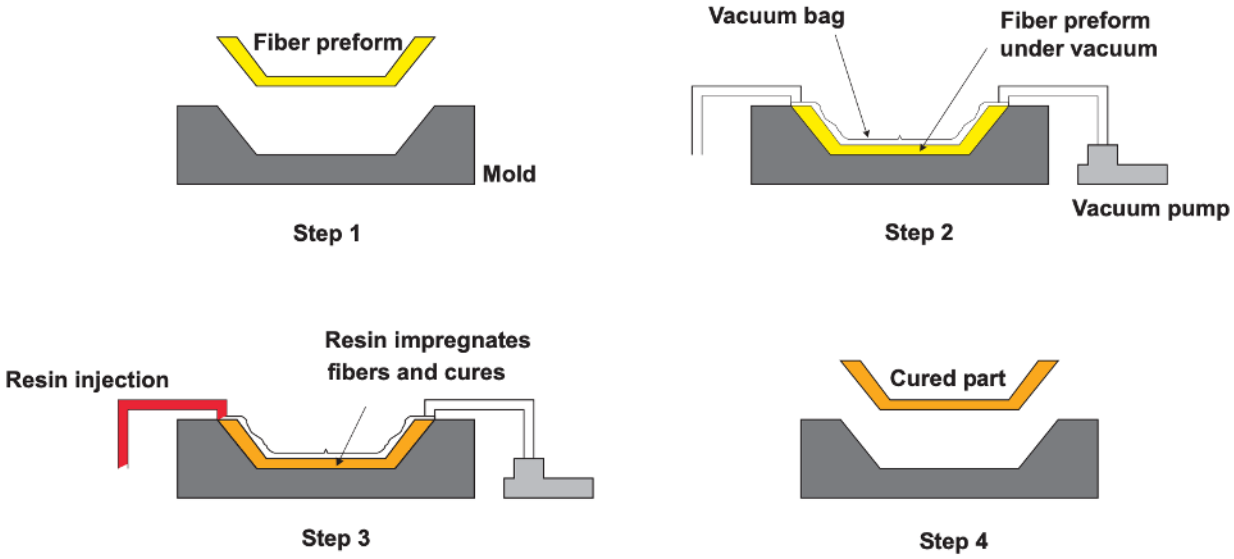

Figure 1.2 Illustration of the steps of Vacuum Assisted Resin Transfer Molding (VARTM) process [1]

RTM and VARTM differ from each other in terms of their molds and resin delivery systems. A double-sided semi-rigid mold is used to compact the fabric and seal it in RTM. Conversely in VARTM, a mold cavity is created by a vacuum bag (used as an upper mold half) which is attached to the semi-rigid lower mold half by a sealant tape. The resin (liquid polymer) is injected from the inlet reservoir to the cavity of the mold by the means of positive inlet pressure or constant flow rate injection machine in RTM, whereas in VARTM, a pressure differential is induced by a vacuum pump that is connected to the exit. Applied pressure differential in VARTM serves two main purposes: (1) compacts the reinforcement material, and (2) drives the resin from inlet to exit through porous fiber preform. Each process

has both pros and cons. An engineer must decide the proper manufacturing process considering the desired physical and mechanical properties of the end product, cost and cycle time. RTM is superior in obtaining high quality parts in terms of mechanical properties and it requires shorter cycle time and thus suitable for high volume manufacturing. On the other, VARTM is superior in producing large parts, and lower equipment and mold cost.

RTM is usually preferred in near-net-shape manufacturing when tight dimensional tolerances are required. Compared to VARTM (in which vacuum pressure compacts vacuum bag), high compaction capability of RTM allows manufacturing of composites with higher fiber volume fraction composites (superior material properties can be achieved). The use of double-sided RTM mold results in a better surface finish on both sides. In contrast, RTM has several drawbacks, mainly in terms of limitations in part dimensions, compared to VARTM. Parts with tens of meters length can be readily manufactured in VARTM, however it is almost impossible to manufacture them in RTM due to requirement of machining and matching the surfaces of mold halves. RTM requires high initial investment for an injection machine and a double-sided rigid mold (which is typically made of steel) with high precision since the two sides of the mold must match almost perfectly. In addition, a clamping equipment or a press is required (the mold must withstand high pressures and apply sufficient compaction force to keep the previously placed fiber reinforcement enclosed).

For some applications, RTM is replaced by VARTM due to its simplicity offering several benefits. Primarily, it requires a lower initial investment cutting down the cost for tooling of the upper half of the mold, and also by providing a simpler solution for mold closure (sealant tape and vacuum bag) and eliminates the need of costly injection machine. Resin propagation can be tracked inside VARTM mold due to the transparent upper mold half (it is typically a nylon bag). Large and complex parts can be readily manufactured by VARTM. However, there are some important limitations/cons of VARTM. The compaction pressure cannot be higher than atmospheric pressure (since the upper half of the mold is open to the atmosphere) which results in lower fiber volume fractions compared to RTM. The use of flexible vacuum bags results in poor dimensional tolerances (thus thickness variation) and high surface roughness on the vacuum bagging side. Compared to RTM in which the cycle

time is relatively short, VARTM requires longer labor time due to skill-intensive vacuum bagging, and longer mold filling time since the pressure differential is limited with a maximum value of one atmospheric pressure [2,4]. As a solution to long mold filling time in VARTM, flow mesh (a.k.a. distribution medium) is placed on top of the fabric preform which facilitates faster resin distribution over the fabric. This method is called Seeman's Composite Resin Infusion Molding Process (SCRIMP), however it requires a carefully designed size and placement of this material, otherwise it may cause entrapment of air pockets in the final part [1].

1.3 Permeability

In the composite material manufacturing industries, the process optimization (to design mold and process parameters) has mostly relied on either the experience of the designer, or experimentation and trial-error methods, which can be significantly costly and time consuming. However, a good understanding of resin flow propagation through porous fiber preform is necessary to ensure complete mold filling is achieved. For this reason, resin flow modelling is often used to optimize the process parameters such as the location of injection and ventilation, flow rate or pressure at inlet and outlet (boundary conditions) which enable the estimation of the mold filling time and help to avoid the macro-scale voids that can be formed in the finished part [1,5-6].

It is a challenging objective to solve classical fluid mechanics' momentum conservation equation through the porous spaces of a fabric architecture due to its complexity. Therefore, the common approach for numerical modelling of resin flow replaces the mentioned momentum equation with of Darcy's Law which establishes an empirical relationship between volume averaged resin velocity and pressure gradient on the macroscopic scale. However, the permeability of the porous medium (fabric) must be characterized under standardized approaches to accurately simulate the resin flow.

The base of many LCM flow simulations relies on an empirical relationship originally developed for flow through sandy/rocky soil by French engineer Henry Darcy (in 19_{th} century). Darcy established an expression, which relates flow rate (thus volume-averaged

velocity) to pressure gradient, for fully saturated, steady-state, creeping flow through a porous medium. This expression, also known as Darcy's Law, is generally given as follows:

$$\overline{\boldsymbol{u}} = -\frac{\mathbf{K}}{\mu} \circ \nabla P \tag{1.1}$$

where $\overline{\boldsymbol{u}}$ is the volume-averaged velocity (a.k.a. Darcy's velocity) vector which is equivalent to the volume flow rate vector per cross-sectional area, μ is the kinematic viscosity of the fluid, ∇P is the pressure gradient and **K** is the permeability tensor of the porous medium. Permeability is defined as the ease of fluid to flow through a porous medium which can also be defined as the inverse of the resistance of the porous medium to flow. In matrix form, Eq. 1.1 can be expressed as follows for 3D Cartesian coordinates:

$$\begin{pmatrix} \bar{u}_x \\ \bar{u}_y \\ \bar{u}_z \end{pmatrix} = -\frac{1}{\mu} \begin{bmatrix} K_{xx} & K_{xy} & K_{xz} \\ K_{yx} & K_{yy} & K_{yz} \\ K_{zx} & K_{zy} & K_{zz} \end{bmatrix} \begin{pmatrix} \partial P/\partial x \\ \partial P/\partial y \\ \partial P/\partial z \end{pmatrix} \tag{1.2}$$

To determine the complete permeability tensor, six scalar components must be known (assuming $K_{ij} = K_{ji}$). This equation (1.2) can be further reduced to (1.3) if the selected coordinate axes overlap with the principal permeability directions of the fabric preform [1]:

$$\begin{pmatrix} \bar{u}_x \\ \bar{u}_y \\ \bar{u}_z \end{pmatrix} = -\frac{1}{\mu} \begin{bmatrix} K_{xx} & 0 & 0 \\ 0 & K_{yy} & 0 \\ 0 & 0 & K_{zz} \end{bmatrix} \begin{pmatrix} \partial P/\partial x \\ \partial P/\partial y \\ \partial P/\partial z \end{pmatrix} \tag{1.3}$$

A good understanding of flow propagation ana capability of numerically solving it is necessary to model mold filling and optimize the process parameters such as the location of injection and ventilation, flow rate or pressure at inlet and outlet (boundary conditions). Thus, it enables the estimation of the mold filling time and help to avoid incomplete mold filling [1,5-6].

1.4 Experimental Permeability Characterization Methods

Permeability is an important parameter that should be characterized to accurately predict the resin flow pattern. It is often characterized by performing experiments under

specific boundary conditions. The two most common experimental methods for permeability characterization are 1D flow experiments and radial flow experiments [7-10]. 1D flow experiments are relatively simpler to set up, however, two separate experiments must be conducted to determine each of two principal permeability components, whereas in radial flow (2D) experiments, both components can be obtained simultaneously by one experiment.

In both 1D and 2D experiments with constant injection pressure, unsaturated (a.k.a unsteady) permeabilities are calculated by recording the flow front location versus time curve. An analytical solution of Darcy's law is fitted to the experimental data to obtain unsaturated permeability. To calculate saturated (or steady) permeability, mass flow rate is measured using cumulated mass (at the outlet container where the resin is collected after it reaches the outlet or, alternatively the change in the mass of inlet reservoir with time) versus time data.

Although commonly accepted experimental permeability characterization approaches are available, literature has many permeability measurement experiments, databases and benchmarking results, which usually have orders of magnitude scatter even on the same fabric, mainly due to variations in material, labor and experimental conditions [11-12].

1.5 Predictive Permeability Characterization Models

Permeability measurement experiments are tedious, time-consuming, and thus not a feasible option to determine permeability, especially when large variety of the fabric structures and their compaction levels (i.e., porosity or fiber volume fractions) are considered. Another potentially efficient approach is to predict permeability by solving mathematical models. Compared to experimental methods, predictive models have the capability to account for the random variations (irregularities) of the fabrics and local permeability variation that may take place in forming stage of the fabrics (which is hard to be characterized experimentally) [13].

Typically, fabric structures used in LCM processes consist of packed fiber bundles (a.k.a. tows or yarns), and they are either woven, uniaxial or stitched together which creates

a dual scale medium, a network of interconnected open channels between bundles (inter-yarn or inter-tow) and empty space between fibers of a bundle (intra-yarn or intra-tow). Typically, at a cross-section of a composite part, inter dimensions are in millimeters and intra dimensions are in micrometers. It is important to model this dual scale medium appropriately for an accurate prediction of permeability. Experimental characterization methods have an overall analysis, but may fail if saturation of intra regions is delayed significantly [13]. However, numerical modeling (such as finite element modeling) is potentially capable of coupling the flows in these dual scales (intra-tow and inter-tow) in complex textile architectures to obtain an overall permeability of a fabric.

Commercially available Computational Fluid Dynamic (CFD) software are often used to model and simulate variety of composite manufacturing processes. Although a woven fabric structure can be discretized and analyzed in the aforementioned manner (dual scale regions in a whole fabric preform), it requires a significant amount of computational time to solve pressure distribution in the whole fabric structure. Instead, the flow domain can be represented as a unit cell of repeatable part of the fabric structure (i.e., a periodic unit cell) which reduces the geometrical complexity and computational time.

In this study, an available through-thickness permeability setup was modified and the through-thickness permeability of a multiaxial non-crimp fabric (NCF) is characterized under steady flow regime using both previous and modified versions of the setup as it will be detailed in Chapter 2. At constant fiber volume fraction, the influence of number of fabric layers and mold cavity height is investigated.

In addition, principal permeabilities of a biaxial fabric was characterized using 2D (radial) flow setup under constant-pressure injection. Variation in experimentally measured through-thickness permeability is evaluated (Chapter 2).

Compressibility of a multiaxial NCF was characterized using Structured Light Scanning (SLS) system. The accuracy of the SLS system was discussed. A new experimental schedule was used to scanning during 3 compaction - decompaction cycles (Chapter 3).

A previously studied dual scale model [22] was pre-solved in ANSYS. After validity of ANSYS solutions was shown by comparing the solutions, the main purpose is account for the non-uniformity and local variation in fiber volume fraction within the fabric structures (by modifying the fiber structure of a regular unit cell) (Chapter 4).

The main contributions of this thesis are (1) a new approach was tested for through-thickness permeability characterization setup in which the fiber volume fraction is adjusted by changing the cavity thickness while keeping the number of layers of the fabric stack the same, (2) the scatter between experimentally measured through-thickness and in-plane permeabilities of different fabrics was studied, (3) a new modelling approach was presented to determine permeability of a fabric structure by accounting for the fabric non-uniformity and the variation in local fiber volume fraction using a commercial software package (ANSYS Fluent).

Chapter 2:
EXPERIMENTAL PERMEABILITY CHARACTERIZATION OF FABRIC PREFORMS

2.1 Materials

Through-thickness permeability of a multiaxial ($-45°/0°/90°/+45°$) E-glass fiber reinforcement was measured for different fiber volume fractions. Silicone oil (Xiameter PMX 200) was used as a test fluid in the experiments.

In radial flow experiments, in-plane permeabilities of a biaxial ($0°/90°$) E-glass fabric (Metyx LT850) was measured at a fixed fiber volume fraction. Similarly, experiments were conducted using silicone oil as a test fluid. Material properties of both reinforcement and silicone oil are given in Table 2.1. Bottom and top view of both reinforcement was shown in Fig. 2.1-2.2.

This study aims to model and measure the permeability and compressibility of reinforcements and does not require any polymer resin since manufacturing of a finished product is out of the scope of this study. Thus, instead of a polymer resin, silicone oil was used as a test fluid in the experiments for several reasons: 1) it is chemically friendly, 2) it is not sticky and thus does not stick to the equipment (i.e., pressure and temperature sensor), 3) easy to clean the equipment afterwards, 4) there are no documents claiming that exposure of silicone oil is unhealthy.

Prior to starting an experiment, the temperature of the silicone oil is measured by a sensor (Keller PAA 35X). As part of a benchmark study among 10+ institutions, viscosity of the silicone oil with respect to temperature was previously measured and provided by Technical University of Munich using a rheometer. As it was done previously in [26], Arrhenius equation, $\mu = Ae^{-E_a/RT}$, was fitted to the temperature-viscosity data by least square method, (see Fig. 2.4) where μ is the viscosity of the silicone oil, T is the temperature, and constants A, E_a and R were determined as 8.3145 $\text{Joule}/°\text{K.mol}$, 2.8858 x$10^{-4}$ Pa.s and -1.4376 x10^{-4} Joule/mol, respectively.

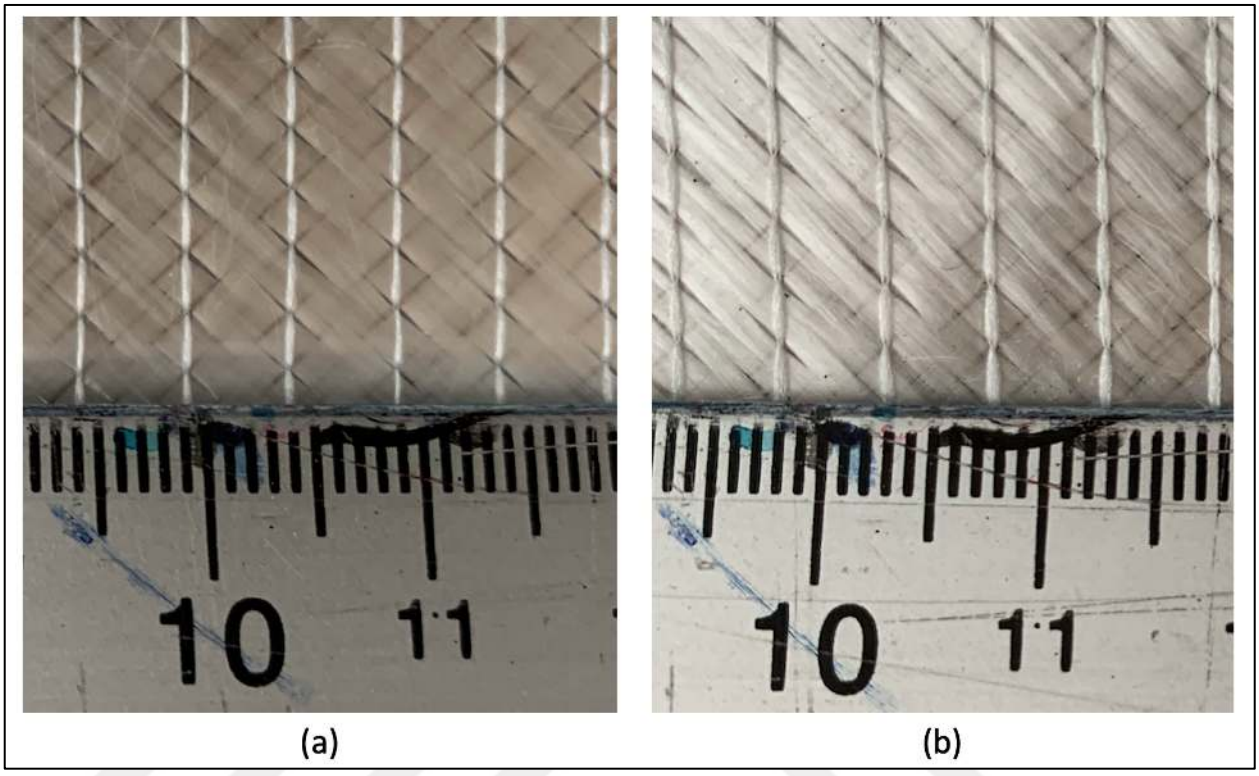

Figure 2.1 (a) top view and (b) bottom view of Saertex E-glass multiaxial non-crimp fabric (NCF)

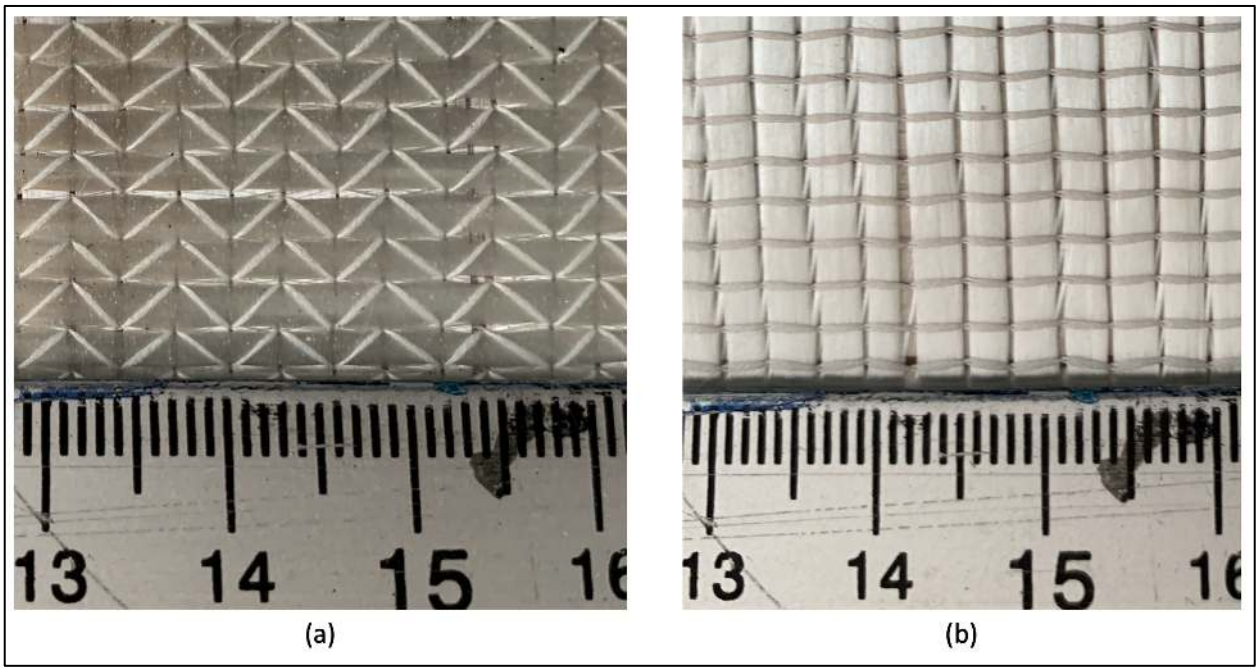

Figure 2.2 a) top view and (b) bottom view of E-glass biaxial fabric (Metyx / LT850)

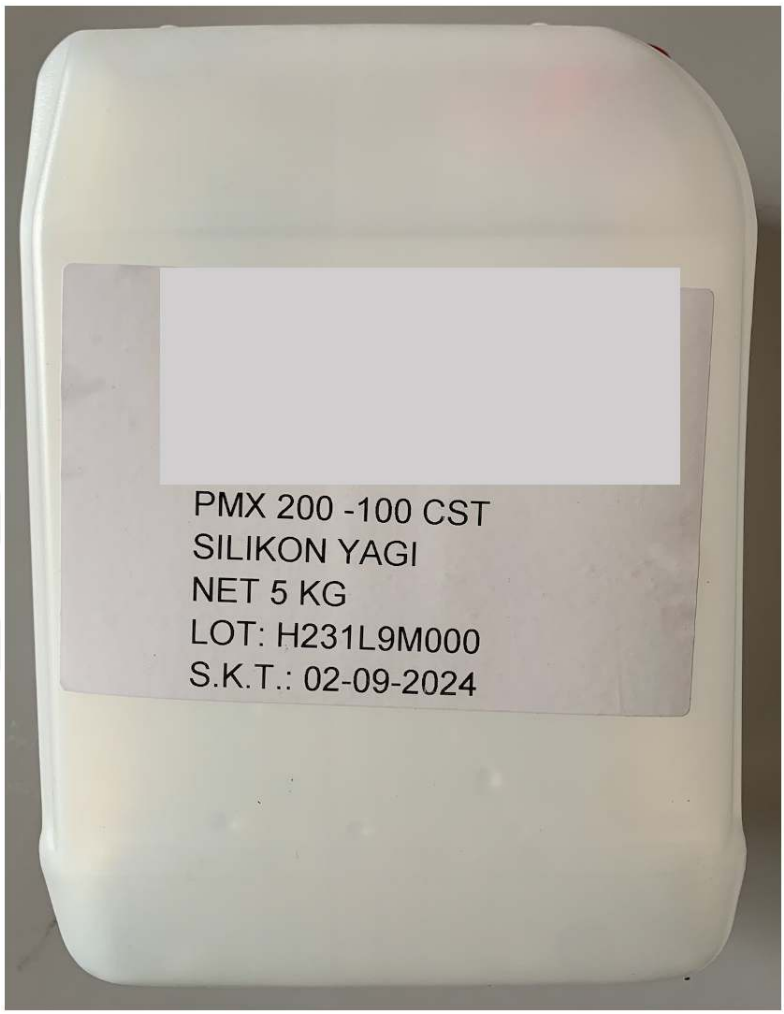

Figure 2.3 Test Fluid **(**Xiameter PMX 200 Silicone Oil)

Table 2.1 Material properties of Xiameter PMX 200 silicone oil, Saertex multiaxial non-crimp fabric and Metyx E- glass biaxial fabric

Silicone Oil (Test Fluid)	Viscosity, μ [Pa.s]	$\mu = Ae^{-E_a/RT}$ where A = 2.8858 x10^{-4} Pa.s E_a = -1.4376 x10^{-4} Joule/mol R = 8.3146 Joule/^{o}K.mol
Multiaxial Fabric (-45^{o}/0^{o}/90^{o}/+45^{o})	Superficial density per layer, ρ_{sup} [g/m^2]	444
	Number of layer in the preform, N	5
	Bulk density of glass fiber, ρ_{bulk} [kg/m^3]	2550
	Compacted thickness (a set of 3), h [mm]	4.22, 3.76, 3.53
	Nominal fiber volume fraction, V_f (experimental values were computed based on measured mass of the fabric, thus they differ from nominal values) (a set of 3) [%]	49.5, 55.7, 59.2
Biaxial Fabric (0^{o}/90^{o})	Superficial density per layer , ρ_{sup} [g/m^2]	850
	Number of layer in the preform, N	5
	Bulk density of glass fiber, ρ_{bulk} [kg/m^3]	2550
	Compacted thickness, h [mm]	4
	Nominal fiber volume fraction, V_f (experimental values were computed based on measured mass of the fabric, thus they differ from nominal values) [%]	41.5

Table 2.2 Viscosity vs. temperature data of Silicone Oil (Xiameter PMX 200) provided by Technical University of Munich [26]

Temperature [°C]	Viscosity [mPa·s]	Temperature [°C]	Viscosity [mPa·s]	Temperature [°C]	Viscosity [mPa·s]
15.00	118.54	…	…	…	…
15.00	118.40	22.86	98.70	39.08	73.91
15.00	118.48	22.94	98.15	39.16	73.71
15.00	118.42	23.03	98.06	39.25	73.7
15.00	118.34	23.11	97.82	39.33	73.36
15.00	118.44	23.19	97.86	39.41	73.27
15.00	118.24	23.28	97.66	39.50	73.34
15.00	118.38	23.36	97.58	39.58	73.14
15.00	118.25	23.44	97.19	39.66	73.20
15.00	118.18	23.53	96.95	39.75	72.96
15.00	118.29	23.61	96.99	39.83	72.73
15.00	118.11	23.70	96.78	39.91	72.82
15.00	118.20	23.78	96.72	40.00	72.62
15.00	118.10	23.86	96.62	40.03	72.71
15.00	118.05	23.95	96.08	40.04	72.64
15.00	118.15	24.03	96.12	40.05	72.62
15.00	118.01	24.11	95.90	40.05	72.77
15.00	118.09	24.20	95.85	40.05	72.64
15.00	117.99	24.28	95.80	40.05	72.76
15.00	118.01	24.36	95.35	40.05	72.72
15.00	118.15	24.45	95.27	40.05	72.71
15.00	117.90	24.53	95.03	40.05	72.87
15.00	118.05	24.61	94.99	40.04	72.75
15.00	117.98	24.70	94.98	40.04	72.88
15.00	117.88	24.78	94.75	40.04	72.86
15.05	117.96	24.86	94.54	40.04	72.88
15.12	117.71	24.95	94.28	40.04	73.03
15.2	117.73	25.03	94.21	40.04	72.93
15.28	117.09	25.11	94.20	40.04	73.16
15.36	116.95	25.19	93.98	40.04	73.08
15.44	116.88	25.28	94.05	40.04	73.17
15.52	116.57	25.36	93.52	40.04	73.3
15.61	116.55	25.44	93.48	40.03	73.18
…	…	…	…	40.03	73.32

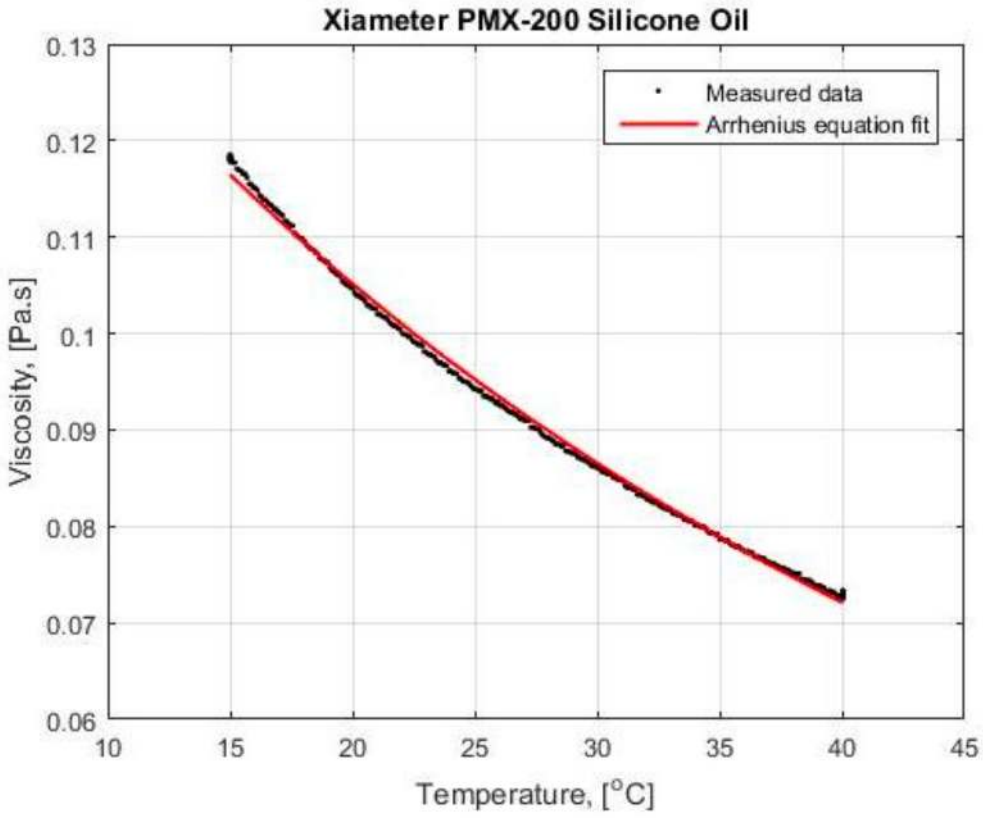

Figure 2.4 Temperature versus viscosity plot for silicone oil (Xiameter PMX 200) [26]

2.2 Calculation of Fiber Volume Fraction

For all of the experiments, fiber volume fraction of a fabric stack is calculated by using two alternatives: (1) $V_{f,n}$ based on nominal superficial density (Vendor's superficial density) and (2) $V_{f,m}$ based on measured mass of the fabric stack. The related formulations are given as follows:

$$V_{f,n} = \frac{Number\ of\ Layers\ \times\ Areal\ weight\ (kg/m^2)}{Final\ thickness\ (m)\ \times\ Fiber\ density\ (kg/m^3)} \tag{2.1}$$

$$V_{f,m} = \frac{m}{A\ h\ \rho} \tag{2.2}$$

where m is the mass of the fabric specimen [kg], A is the area of the specimen, h is the final thickness of the specimen [m] and ρ is the density of the glass fiber [kg/m^3].

2.3 Experimental Characterization of Through-Thickness Permeability (Kz)

Usually, composites are thin parts in which the resin flow is primarily in the in-plane directions, and through thickness permeability has a negligible effect on many RTM applications. However, in VARTM of large-scale parts, such as wind turbine blades, through-thickness permeability may play an important role especially when a flow mesh is used on top of the fabric preform which allows resin to flow faster at the upper region of the fabric and facilitates transverse flow in thickness direction [20]. In addition, the effect of through-thickness permeability becomes more significant as the thickness of the part increases or it has a tapered thickness (i.e., a significant thickness variation) [19-20].

2.3.1 Method

In through-thickness permeability characterization experiments, resin is driven inside the mold from the bottom of the fabric and propagates along out of plane direction (z direction). It should be noted that, this experiment is conducted only for the saturated (steady) flow regime. The main reason for that is the flow front cannot be tracked inside the relatively thin mold cavity which is created by double sided rigid mold.

Once the resin reaches to the exit (upper side of the circular mold), it continues to flow from the exit for a while to ensure steady flow is achieved. Resin is accumulated in a container at the outlet which is placed on a digital scale. Mass of the resin is recorded over time and slope of the mass vs time (dm/dt) data is calculated to determine volume flow rate (Q) as $Q = (dm/dt)/\rho$, where ρ is the density of the resin. Through-thickness permeability of the fabric preform is calculated for steady flow regime under constant injection pressure by Darcy Law using the following the expression:

$$K_z = \frac{Q\mu h}{A\,\Delta P} \tag{2.3}$$

where h is the thickness of the fabric preform, μ is the resin viscosity, A is the cross-sectional area of the flow domain (i.e., area of the top surface of the fabric preform) and ΔP is the applied pressure difference between top and bottom surfaces of the preform. To exclude the

influence of hydrostatic pressure difference between top and bottom of the setup, ΔP is expressed as follows [21]:

$$\Delta P = P_{inj,gage} - \rho g \Delta L \quad (2.4)$$

where g is the gravitational acceleration and ΔL is the vertical distance between the top of the exit tube and the middle of the exit of the sensor reservoir. It is assumed that $dP/dz = \Delta P/\Delta L$ = constant.

2.3.2 Experimental Setup for Through-Thickness-Permeability Characterization

The through-thickness permeability characterization setup is seen in Fig. 2.5.There are 6 main components in the experimental setup which can be listed as: 1) Lower mold half, 2) lower perforated disk (6000 series aluminum), 3) stainless steel lower flange (with thickness of 1mm, inner diameter of 95 mm and outer diameter of 98.2 mm), 4) a metal tube to enclose the mold parts (6000 series aluminum tube), 5) a metal ring (modified from Hasan Caglar' s study [26]), see section 2.1.3) , 6) stainless steel upper flange glued to the upper perforated plate, 7) upper mold half (6000 series aluminum).

In this experimental setup, fabric preform is further compacted by circular upper and lower flanges (thickness of each flange is 0.5mm) at the cut periphery of the preform to prevent race tracking (see Fig. 2.4 (b)). The lower flange is attached to the lower mold half which is placed inside the aluminum tube. The metal ring is placed on top of the lower flange which creates a mold cavity for the circular fabric preform. A preform is prepared by stacking 12 plies inside the metal ring. Production direction of each layer is aligned carefully. The upper flange is placed on top of the fabric preform and the upper mold half is fitted on the metal ring. To ensure that the mold is closed completely, 4 bolts and 8 nuts are used to compact the mold, and distance between the lower and upper mold is measured by a digital caliper which must be below a certain value for each metal ring (detailed in Section 2.2.3).

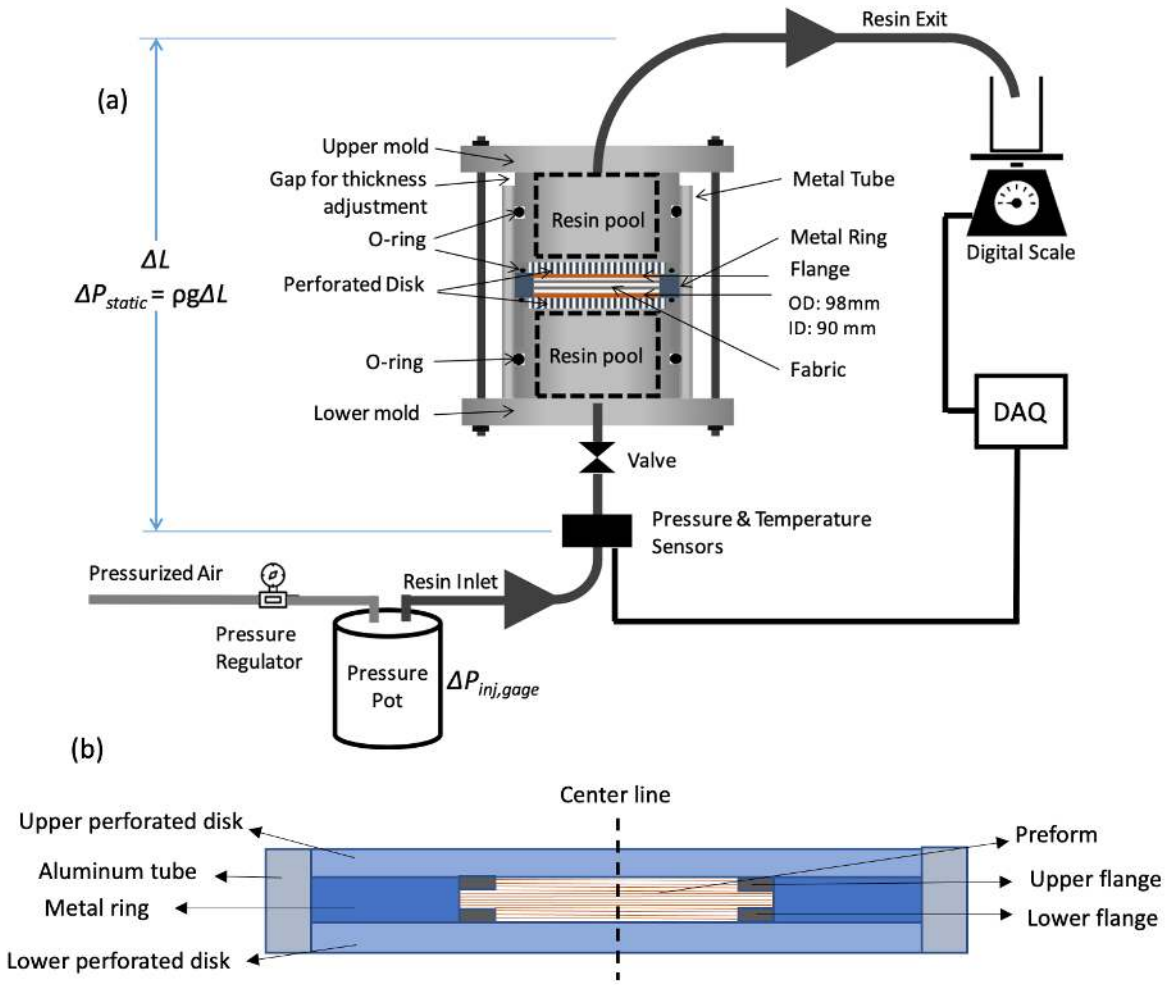

Figure 2.5 Through-thickness permeability characterization setup: (a) adapted from Hasan Caglar's MSc.Thesis [26], (b) illustration of compacted preform

The injection pressure is set to 100 kPa by using an analog pressure regulator. Inlet valve is then opened to start the resin injection. To ensure that steady flow is achieved, resin injection is sustained for 360 seconds after the resin reaches to the exit. The last 120 seconds of the mass vs. time data is used to calculate flow rate [26].

2.3.3 Modification On Cavity Height (h) of The Through-Thickness Permeability Measurement Experimental Setup

In the previous version of the through-thickness permeability characterization experimental setup [26], there was a single metal ring with the thickness of h = 10.0 ±0.1 mm which requires above 30 layers of multiaxial fabric to reach fiber volume fraction of 0.55. In addition, the fiber volume fraction is adjusted by changing the number of fabric layers and keeping h constant.

A new approach was designed for number of reasons: 1) to reduce the fabric use, 2) to eliminate the error that may be caused by misalignment of fabric layers during stacking (since the number of layers is relatively high), 3) to adjust the fiber volume fraction by changing the cavity height but keeping the number of layers the same. Thus, three different metal rings were produced with the thicknesses of 4.22 mm, 3.76 mm and 3.53 mm (with the same inner and outer diameters with the previous design: d_{in} = 98.2 mm and d_{out} = 138.0 mm). Using the same multiaxial fabric used in [26] but from a new batch in 2022, this approach allows fiber volume fractions of 50, 55, 60% to be reached using 12 layers of fabric in the thickness of 4.22 mm, 3.76 mm and 3.53 mm, respectively.

In the previous version of the setup, flanges were used to further compact the edges of the preform to prevent racetracking through the edges. There were two flanges with the thickness of 1 mm which are placed at bottom and top of the fabric stack. Since the cavity height is changed in this new version of the setup, the use of 1mm flanges resulted in unrealistic fiber volume fractions. Thus, the thickness of the flanges was reduced to 0.5 mm to reduce the fiber volume fraction at the edges of the fabric stack to a reasonably lower percentage, but still keeping them significantly above the fiber volume fraction inside the mold to prevent race tracking.

Table 2.3 shows the corresponding fiber volume fractions using flanges with a thickness of 0.5 mm. Theoretically the maximum fiber volume fraction that can be reached with NCF is around 70% at the stitched region [43]. Thus, the values above 70% are indicated as red. It is important to note that even though the fiber volume fraction of the fabric at the

flange region is above 70% for metal ring 1 and metal ring 2, the mold could be compacted to the desired thickness which is ensured by further tighten the nuts using a pneumatic nut wrench and by measuring the vertical distance between lower and upper aluminum plates by a digital caliper from all of 4 edges. The target distances between lower and upper aluminum plates are 59.27 mm, 59.50 mm and 59.95 mm for metal ring 1, metal ring 2 and metal ring 3, respectively. The components and assembly procedure of the setup is given in Fig 2.6-2.9.

Table 2.3 Comparison of fiber volume fractions obtained by using 3 molds with two 0.5-mm-flanges to further compress the edges of the fabric preform. (Fiber volume fraction, $V_{f,n}$ is calculated by nominal superficial density of the multiaxial non-crimp fabric).

	Metal Ring Mold 1	Metal Ring Mold 2	Metal Ring Mold 3
Cavity thickness, h	3.53 mm	3.76 mm	4.22 mm
$V_{f,n}$ for actual cavity	59.2%	55.7%	49.5%
Thickness of the fabric at flange region (x2 0.5 mm flanges)	2.53 mm	2.76 mm	3.22 mm
Corresponding $V_{f,n}$ for flange region (x2 0.5 mm flanges)	86.7%	79.4%	67.4%

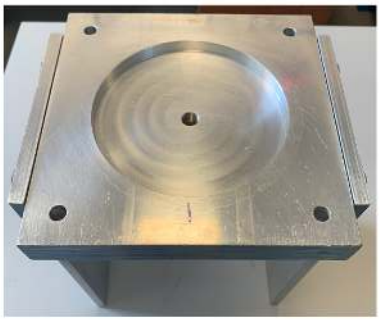

1) Aluminum lower mold half (inlet ϕ 12 mm)

4) Stainless steel lower flange (inner ϕ 90 mm - outer ϕ 98 mm, thickness of 0.5 mm)

2) Lower perforated disk (ϕ 138 mm)

5) 3 metal rings each for different V_f , (t = 3.53mm, 3.76mm, 4.22mm),(inner ϕ 100mm mm - outer ϕ 138 mm)

3) Aluminum tube (inner ϕ 138 mm - outer ϕ 158 mm, thickness of 8 mm)

6) Upper perforated disk (ϕ 138mm), stainless steel glued to the upper flange (inner ϕ 90 mm - outer ϕ 98 mm)

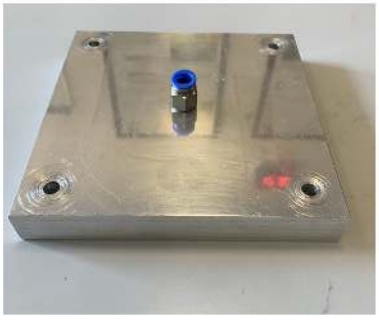

7) Aluminum upper mold half (outlet ϕ 12 mm)

Figure 2.6 Components of the through-thickness permeability characterization setup

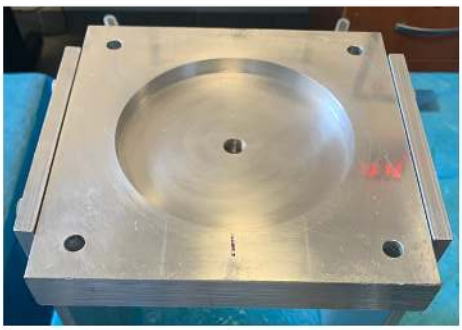

(1) Grease inner surface of the lower mold half

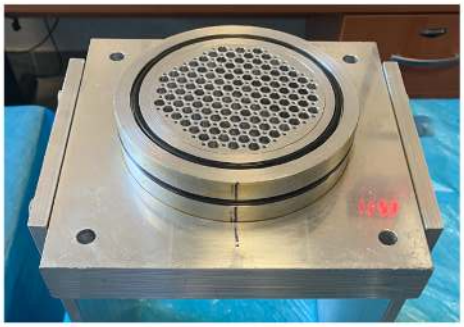

(2) Grease lower perforated disk and place on top of the lower mold half

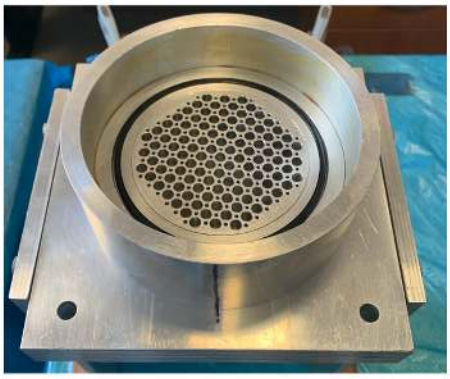

(3) Grease and place aluminum tube as it surrounds the lower perforated disk

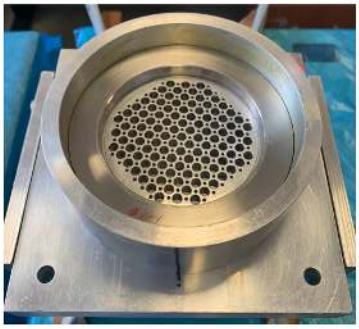

(4) Grease outer surface of the metal ring and place it inside the aluminum tube

(5) Place the lower flange inside the metal ring

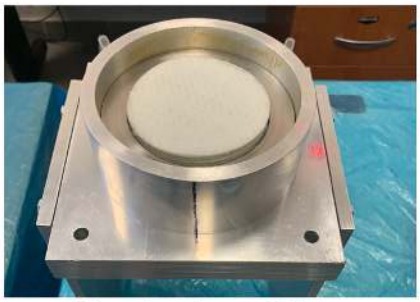

(6) Stack 12 layers of fabric

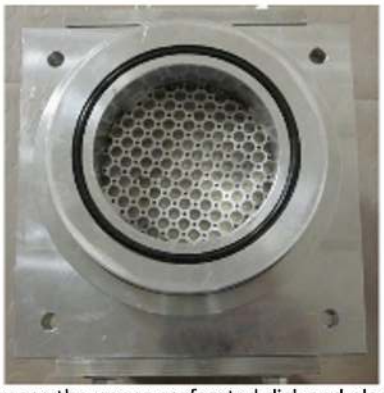

(7) Grease the upper perforated disk and place it inside the aluminum tube, compress the fabrics

(8) Place he upper mold half on top of the upper perforated disk

Figure 2.7 Assembly steps of the through-thickness permeability characterization setup

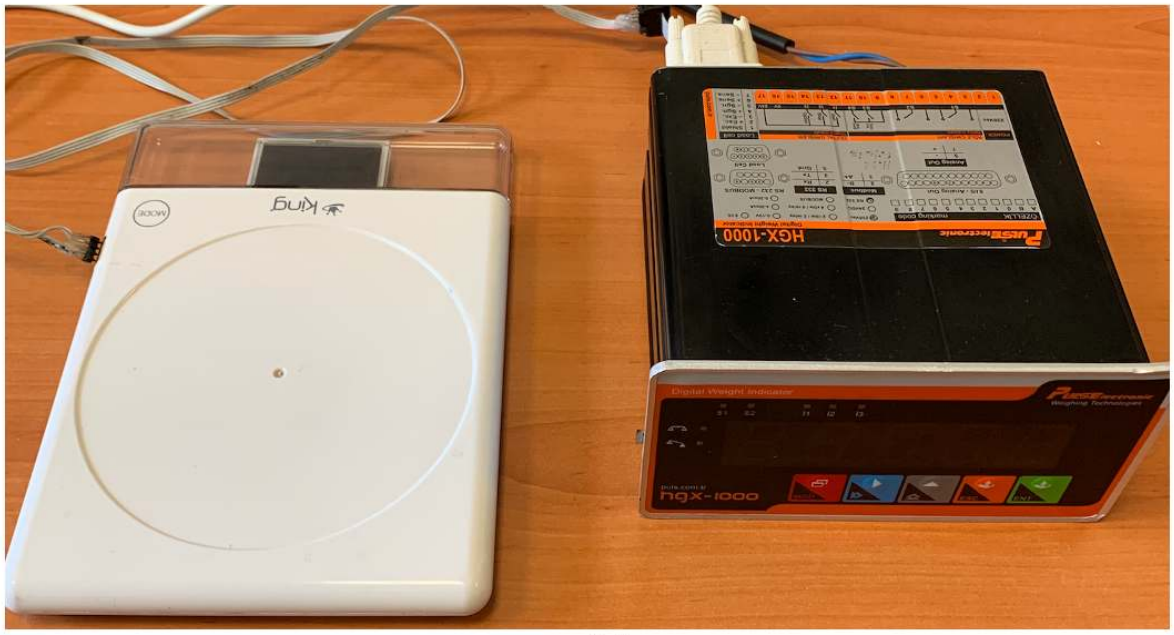

(a)

(b)

Figure 2.8 Components of the through-thickness permeability characterization setup, a) digital scale (left) and DAQ system (right), b) pressure vessel (filled with silicone oi

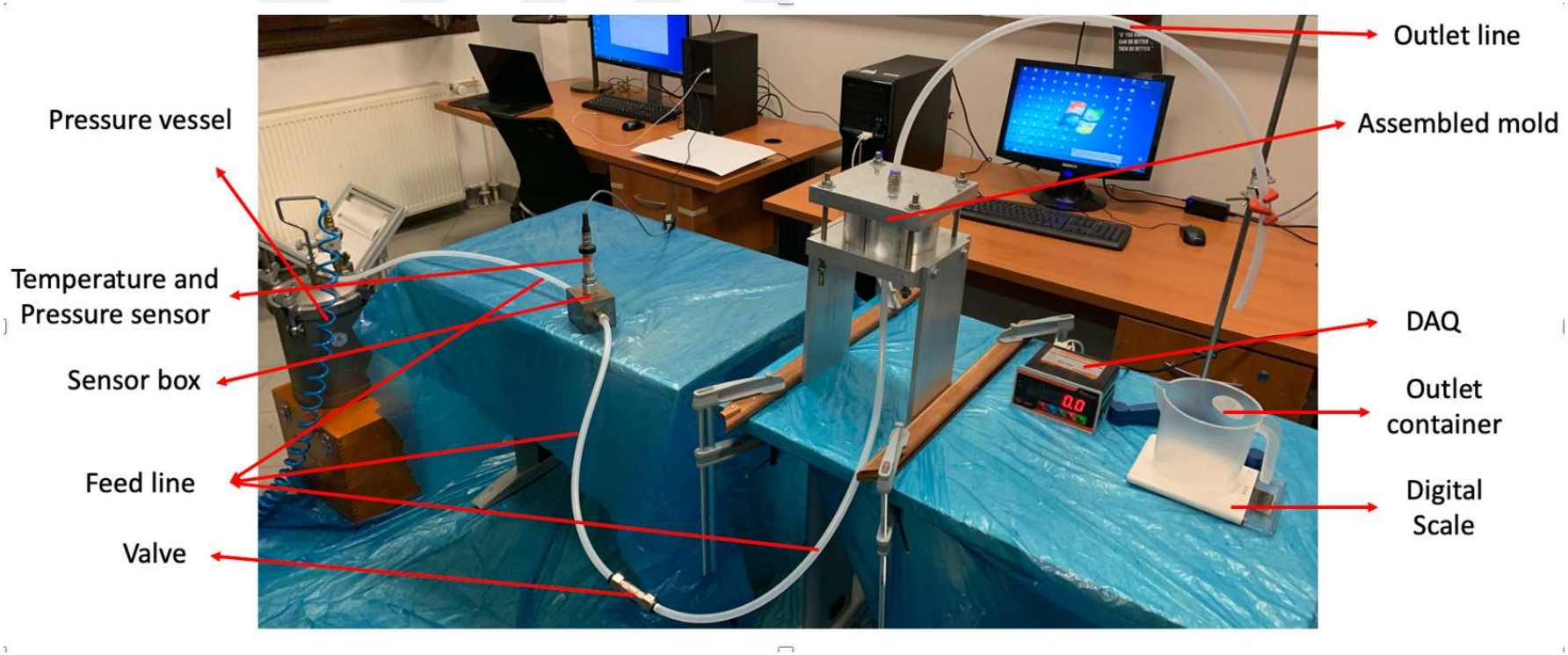

Figure 2.9 Assembled through-thickness permeability characterization setup

2.4 2D Radial Flow Experiment

Compared to 1D experiments, a 2D (radial) permeability experiment allows the determination of both principal permeability values and their orientations with a single experiment. In 2D permeability experiments, resin is driven into the mold from the center of the lower mold The outlet vent is kept open to the atmosphere during the infusion. In order to prevent the resin flow through the thickness direction at the beginning of the infusion, the center of the fabric layers is punched by a circular punch which has the same diameter with the inlet hole (ϕ = 12 mm).

For anisotropic materials, an elliptic flow front is observed in a radial flow experiment whereas for isotropic materials, the flow front becomes circular. To rephrase it, permeabilities in principal directions, $r_{0°}$ and $r_{90°}$, should be the same if the fabric is isotropic. The flow front radii along the production line of a fabric roll and along the width of the roll (i.e., transverse direction) are expressed as $R_{0°}(t)$ and $R_{90°}(t)$, respectively. Usually, when an anisotropic fabric is used, resin flows faster along the production direction (0°) than the transverse direction (90°) as shown in Fig 2.10. The main reason for that is the porosity is higher in 0° direction for the fabrics typically used in LCM processes as well as the ones used in this study which will be detailed in following chapters. In this study, anisotropic biaxial fabric preforms (See Section 2.1) was used, 0° and 90° directions were named as the principal directions since β was measured to be small (typically $\beta < 1^{o}$).

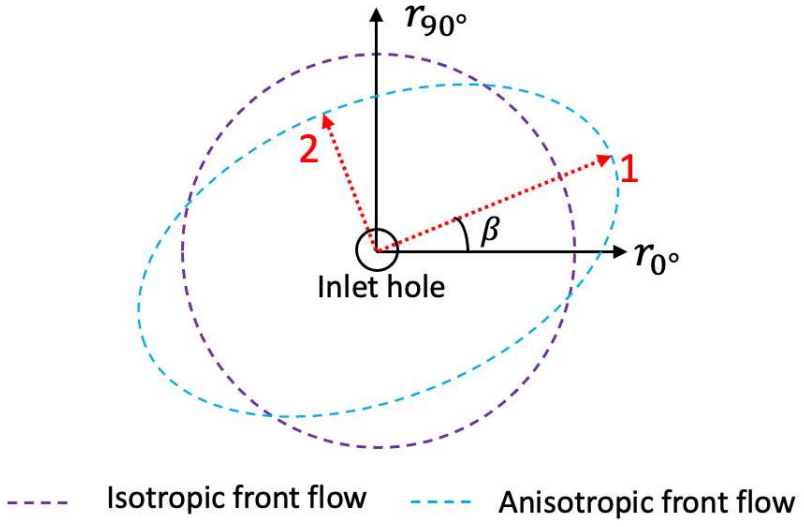

Figure 2.10 Illustration of flow propagation through an isotropic and anisotropic fabric preform

An unsteady 2D (radial) permeability measurement experiment offers several advantages compared to an unsteady 1D permeability measurement experiments: (1) permeability components in both in-plane principal directions can be measured simultaneously by a single experiment, thus it is less time consuming , (2) the effect of race-tracking is eliminated, which may take place between mold walls and fabric layers in 1D experiment that may cause a deviation from 1D flow and results in unreliable permeability computations.

In a 2D unsteady experiment, the flow front propagation for both directions (0° and 90°) are recorded by a camera which is placed over the mold. Under constant injection pressure, unsteady permeability (K_{uns}) components along 0° and 90° directions are calculated by the following expressions [1]:

$$K_{uns,0} = \frac{\mu\phi}{4P_{inj}}\left\{r_{f,0}^2\left(2\,ln\left(\frac{r_{f,0}}{r_i}\right)-1\right)+r_i^2\right\}\frac{1}{t} \tag{2.5}$$

$$K_{uns,90} = \frac{\mu\phi}{4P_{inj}}\left\{r_{f,90}^2\left(2\,ln\left(\frac{r_{f,90}}{r_i}\right)-1\right)+r_i^2\right\}\frac{1}{t} \tag{2.6}$$

where ϕ is the porosity of the fabric preform, μ is the viscosity of the resin, $r_{f,0}$ and $r_{f,90}$ are the radii of the flow front (for r_{0° and r_{90° directions), r_i is the radius of the inlet hole (0.006 m), P_{inj} is the injection pressure and t is time. Note that the right-hand side of (2.5) and (2.6) are expected to be constants, that means not to be functions of time, t. Thus, one should curve fit the right hand side to a best -fit constants and equate them to $K_{uns,0}$ and $K_{uns,90}$.

The steady permeability experiment is conducted after the complete impregnation of the fabric preform is achieved. Accumulated mass of the resin that is coming out of the eight outlets is measured over time by a digital scale. To calculate the volumetric flow rate, Q, total mass flow rate $\dot{m}$ is determined by the first order curve fit to the experimental mass vs time data, and divided by the resin density ρ.

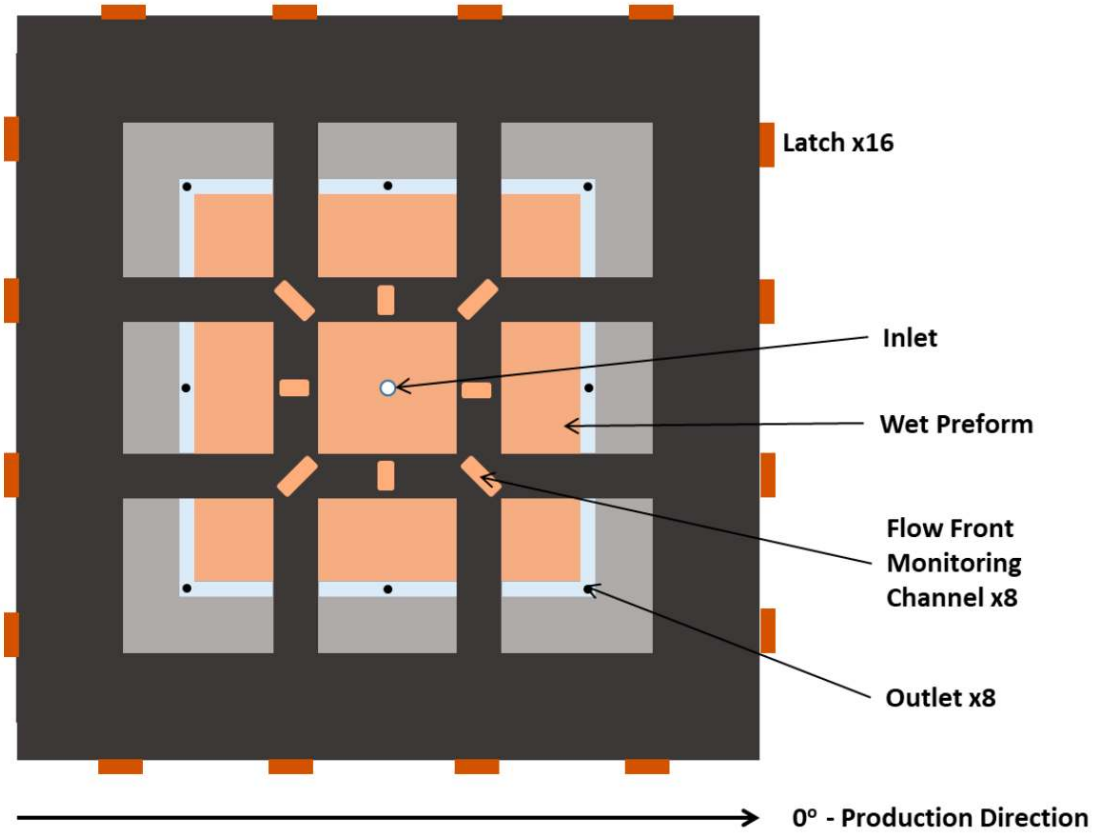

Figure 2.11 Top view of 2D (Radial) permeability measurement setup (when complete saturation of fabric preform is achieved) (adapted from Hasan Caglar's MSc. Thesis) [26]

Steady permeability components are computed by matching the numerically determined total outflow volumetric flow rate with the experimental volumetric flow rate. Conservation of mass is considered to numerically model the 2D experiment:

$$\left[\left(-\frac{K_{s,xx}}{\mu}\frac{\partial P}{\partial x}\right)_{x} - \left(-\frac{K_{s,xx}}{\mu}\frac{\partial P}{\partial x}\right)_{x+\Delta x}\right] h\Delta y + \left[\left(-\frac{K_{s,yy}}{\mu}\frac{\partial P}{\partial y}\right)_{y} - \left(-\frac{K_{s,yy}}{\mu}\frac{\partial P}{\partial y}\right)_{y+\Delta y}\right] h\Delta x = 0 \quad (2.7)$$

In order to express this equation in a finite differences form, first term on the left-hand side is multiplied by $\Delta x/\Delta x$ and similarly the second term is multiplied by $\Delta y/\Delta y$. If

Δx and Δy terms approach to infinitesimal dx and dy, respectively, (2.7) is expressed as the following differential equation:

$$\frac{K_{s,xx}}{\mu}\frac{\partial^2 P}{\partial x^2}+\frac{K_{s,yy}}{\mu}\frac{\partial^2 P}{\partial y^2} = 0 \tag{2.8}$$

Dividing both sides of the equation by $K_{s,yy}/\mu$, (2.8) takes the following form:

$$\frac{K_{s,xx}}{K_{s,yy}}\frac{\partial^2 P}{\partial x^2}+\frac{\partial^2 P}{\partial y^2} = 0 \tag{2.9}$$

Using finite difference method and the proper boundary conditions at the inlet and the outer boundaries, (2.9) is solved inside the resin filled domain as shown in Fig 2.11(a).

In this study, the ratio of the steady permeability components and the ratio of the unsteady permeability component are assumed to be the same where unsteady permeabilities were already found by the unsteady permeability characterization experiment:

$$\frac{K_{s,xx}}{K_{s,yy}} = \frac{K_{uns,xx}}{K_{uns,yy}} \tag{2.10}$$

The numerical total outflow volumetric flow rate is calculated as follows:

$$Q_{num} = \int_A U_n \cdot \hat{n}\, dA \tag{2.11}$$

where A is the outer peripheral area of the fabric preform, U_n is the velocity vector and $\hat{n}$ is the normal outward unit vector on A.

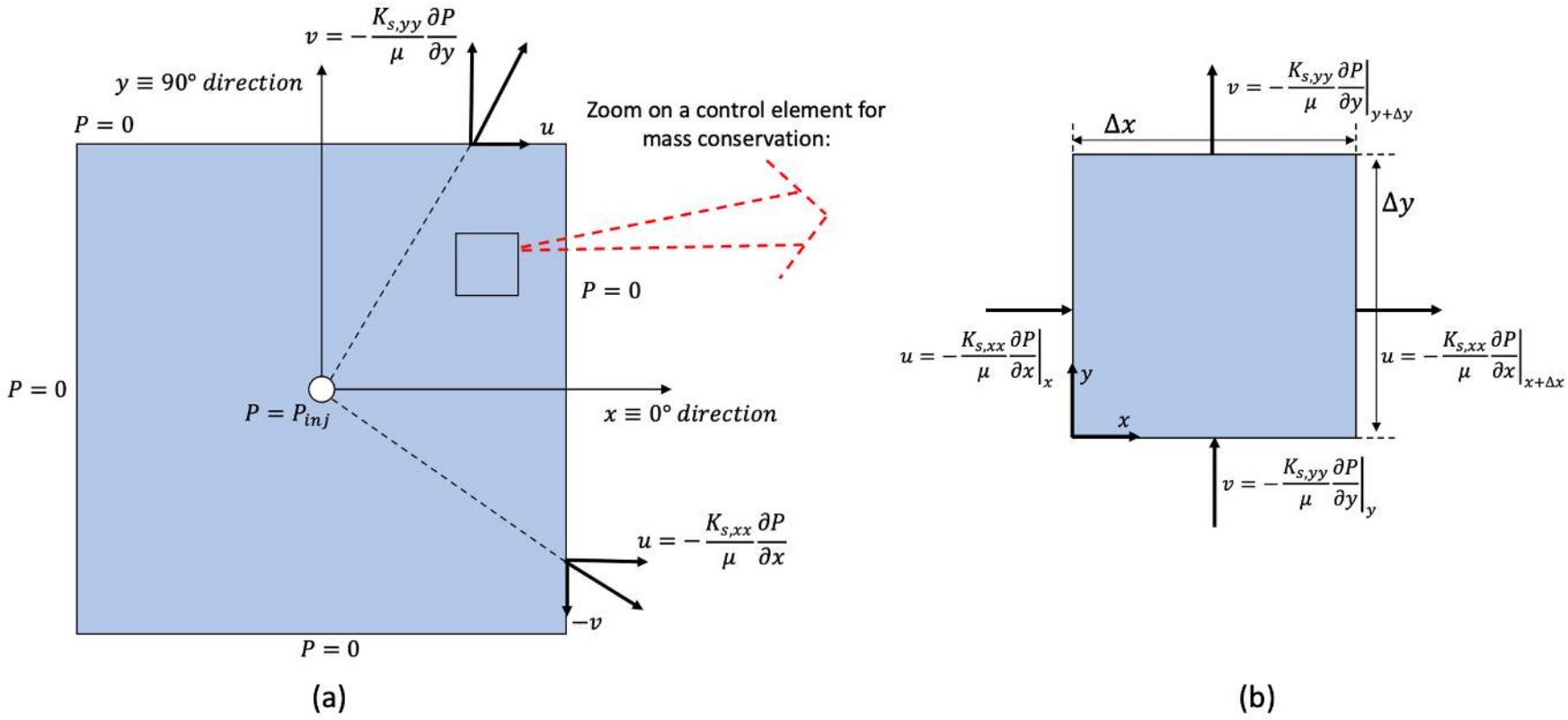

Figure 2.12 (a) Resin filled solution domain for 2D steady state flow and boundary conditions at the inlet hole and the outer boundaries, (b) Control element for deriving the mass conservation in the solution domain

2.4.1 Experimental Radial (2D) Permeability Characterization Setup

Five layers of biaxial fabric with square shape (220 x 220 mm) is cut, stacked, and punched with a radius of 6 mm (inlet radius of the mold) at their center. The fabric preform is then placed on the lower mold plate which is made from aluminum (6000 series). Thickness of the mold cavity is adjusted by eight steel spacers which have a thickness of either 3.0, 3.5 or 4.0 mm. The spacers are placed on the lower mold plate and fabric preform is compacted by the aluminum (6000 series) upper mold plate, which has glass monitoring windows, using eight clamps and sixteen latches (see Fig. 2.13).

Resin in the pressure pot is pressurized by the compressed air to the desired injection value (80 kPa gage pressure). This constant injection value is set by an analog pressure regulator (CKD RP1000).

Temperature and pressure of resin (silicone oil) are measured by a sensor (Keller PAA 35X, 0-10 bar abs, 0.002 full scale resolution). The measured values are monitored and recorded by a software called Control Center Series 30. It is important to note that no significant variation in temperature was observed during an experiment (both the mold and resin reservoir are at the room temperature) and also the silicone oil is stored at the room temperature. However, for the convenience, the viscosity of the silicone oil was calculated by using the average of the recorded temperature values during any experiment by MATLAB.

Resin is injected by opening the inlet valve. Flow front propagation is recorded until the fabric preform is completely impregnated by the resin, using a digital camera placed on top of the mold (where the flow front propagation can be clearly seen through the glass inspection region) [26].

Once the resin arrives to the outlet holes (there are 8 of them) at the edges of the lower mold plate, it continues to be flushed to the outlet resin reservoir placed on a digital scale

[26]. The mass versus time data of the resin accumulated in the outlet reservoir is recorded by a DAQ system connected to MATLAB. After the resin comes out of the outlet, resin flushing is continued for 120 seconds to reach steady state.

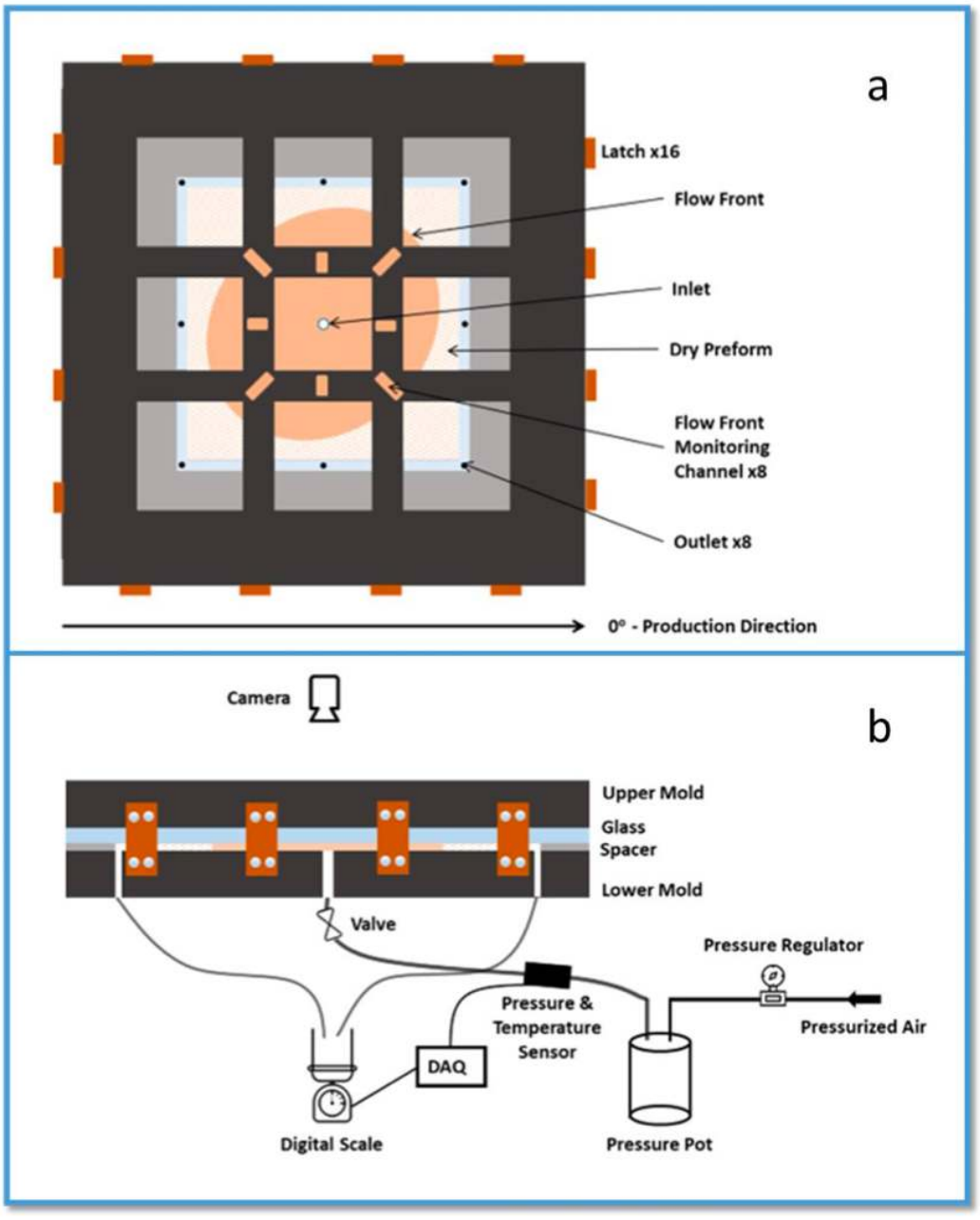

Figure 2.13 Illustration of 2D (radial) permeability characterization setup in unsaturated flow regime: (a) top view, (b) side view

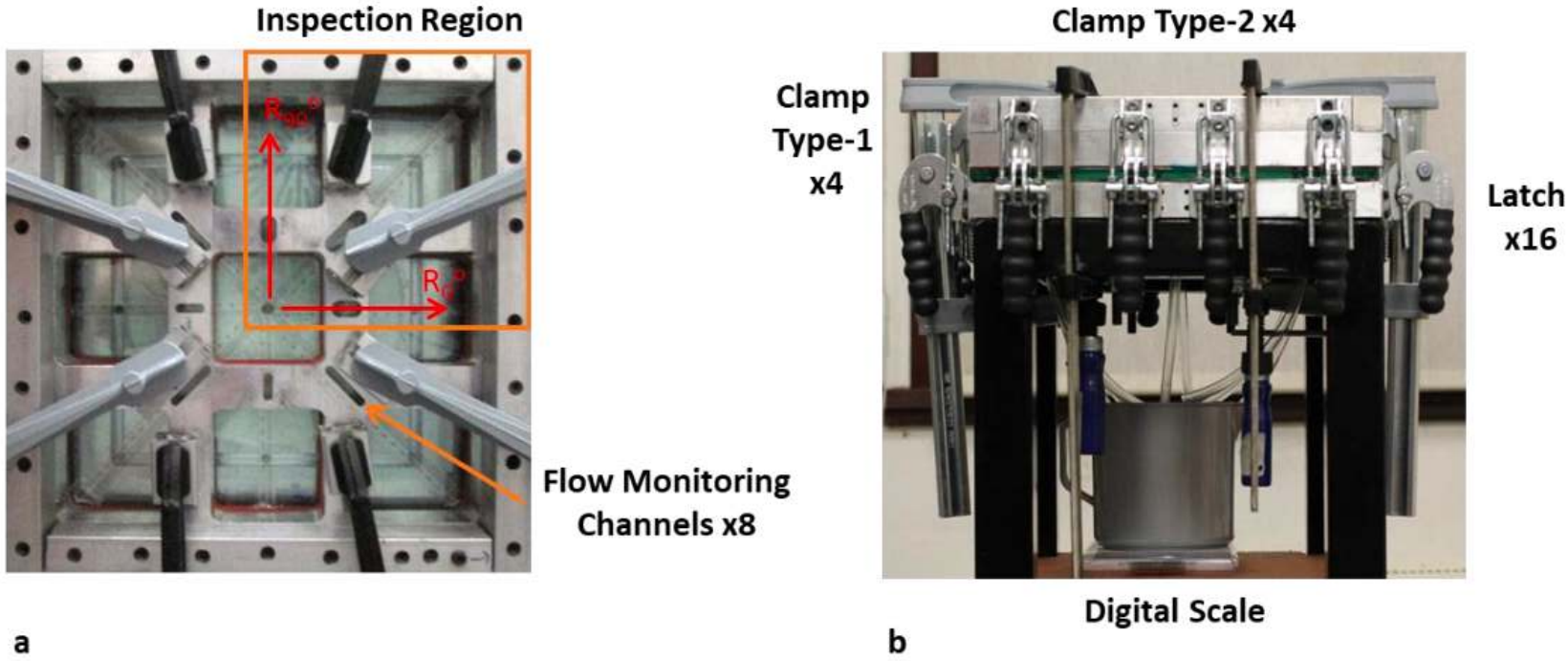

Figure 2.14 (a) top view and (b) sideview of 2D (radial) permeability characterization setup [26]

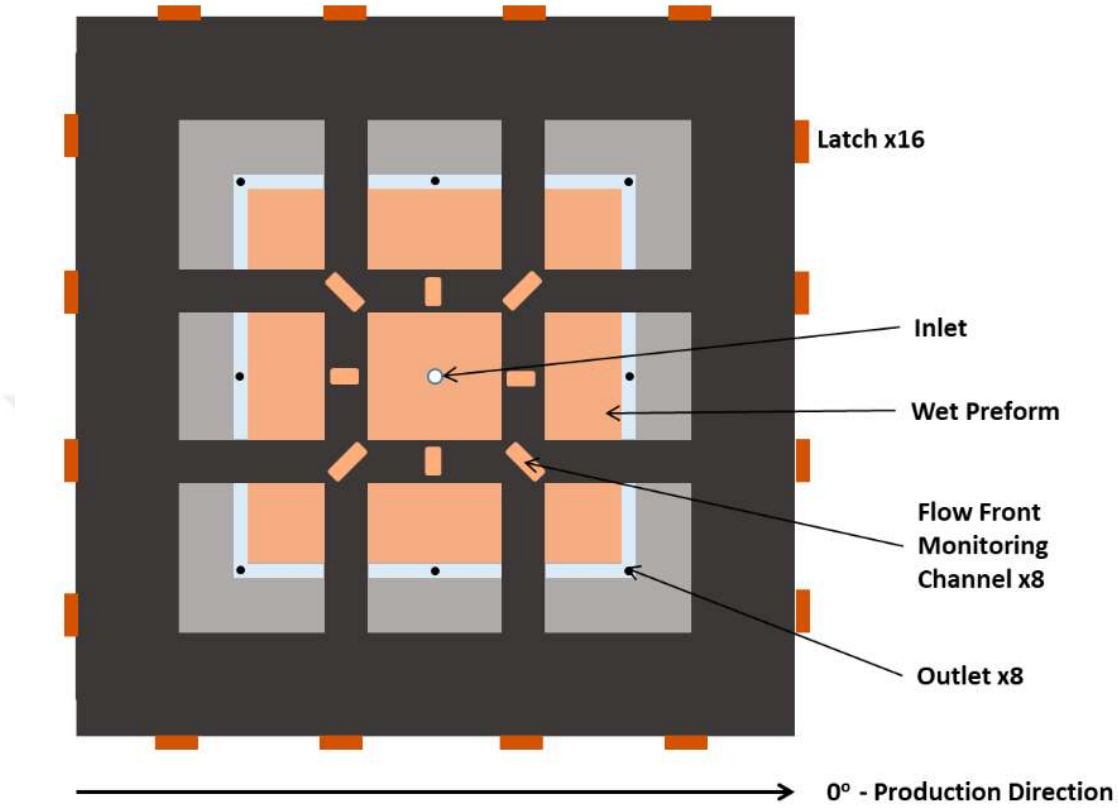

Figure 2.15 Illustration of 2D (Radial) permeability characterization setup with steady flow regime (Fabric preform is completely impregnated with resin, but the resin injection is continued for 120 seconds) [26]

2.5 Results

In the scope of a benchmark exercise total of 15 experiments were conducted using through-thickness permeability characterization setup (5 experiments for $V_f = 50\%$, 5 for $V_f = 55\%$ and 5 for $V_f = 60\%$). However, results will not be shared in this thesis due to confidentiality agreement, instead of that, the result of a through-thickness test experiment and a sample calculation will be shown in this section. Note that the fabric used in the benchmark exercise and the test experiment was the same. However, the one used in the test experiment is from the previous benchmark exercise (2018).

In addition, 3 experiments were conducted for the same V_f (41.5%) using 2D (Radial) permeability characterization setup. However, because of the potential of this data to be used

in a future academic article, results of a single experiment and corresponding sample calculation will be shared here in this thesis.

2.5.1 Sample Calculation for The Through-Thickness Permeability Characterization Experiment

Through-thickness permeability characterization experiments are conducted under constant injection pressure boundary condition. K_z (through-thickness permeability) is calculated using the input parameters listed below:

N (number of layers) = 12

m (mass of the fabric preform) = 37.9 g

h (thickness of the preform) = 3.53 mm

d (diameter of the fabric preform) = 96.0 mm

d_f (diameter of the resin flow) = 90.0 mm

μ (viscosity of the resin) = 0.0987 Pa.s

ρ (density of the resin) = 964 kg/m^3

ΔL (difference between the height of the pressure sensor and the top of the exit tube)
= 0.635 m

ΔP (pressure differential) = 88.3 kPa

S (cross-sectional area of the flow channel) = $\pi(d_f/2)^2$ = 0.006362 m^2

Mass flow rate (dm/dt) was calculated by fitting a first order curve to the experimentally measured time versus accumulated mass of the resin at the exit container (which is placed on a digital scale) and taking the slope of the curve as shown in Fig 2.16. Volume flow rate was calculated by dividing the mass flow rate by density of the resin (ρ) which was found to be 4.87×10^{-7} m^3/s. K_z is calculated by the following equation:

$$K_z = \frac{Q\,\mu\,h}{S\,\Delta P} = \frac{(4.87\ \times\ 10^{-7})(0.0987)(0.00353)}{(0.006362)(88315)} = 3.02\ \times 10^{-13}\ \text{m}^2 \tag{2.12}$$

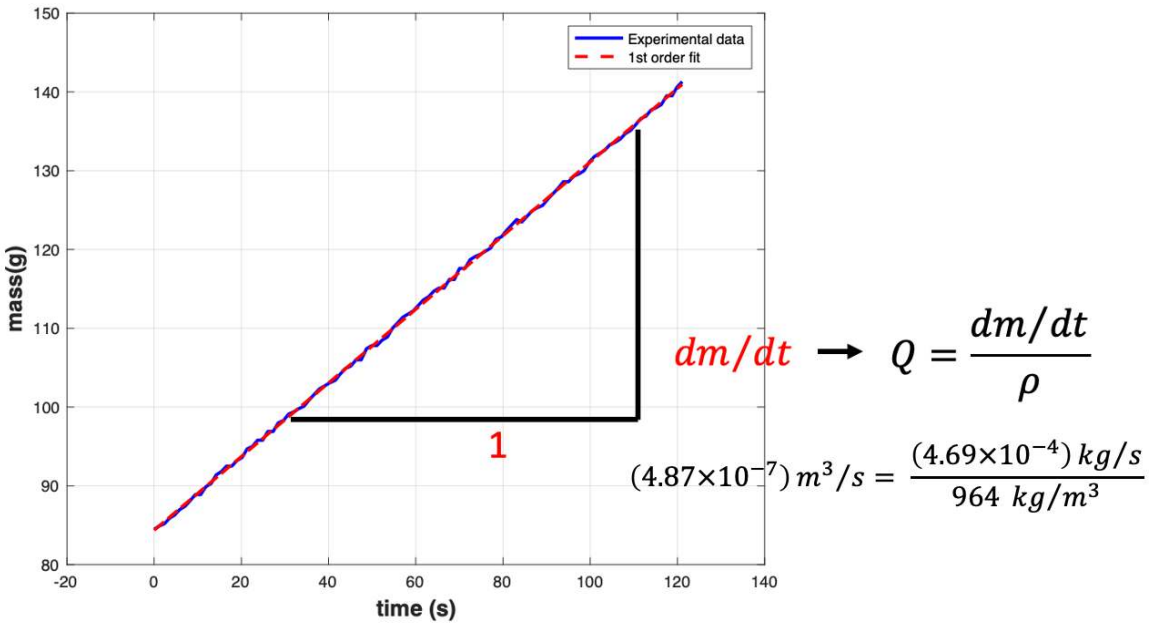

Figure 2.16 Mass of accumulated resin at the outlet container versus time data

2.5.2 Sample Calculation for 2D (Radial) Permeability Characterization Experiment

Similar to the through-thickness permeability characterization experiments, 2D permeability characterization experiments were conducted under constant injection pressure boundary conditions using the inputs given below:

N (number of layers) = 5

m (mass of the fabric preform) = 205 g

h (thickness of the fabric preform) = 4.00 mm

l (length of the fabric preform) = 220 mm

w (width of the fabric preform) = 220 mm

ρ_{fiber} (bulk density of glass fiber) = 2550 kg/m^3

ρ_{resin} (density of the resin) = 964 kg/m^3

ρ_{sup} (superficial density of the fabric) = m / (N l w) = 0.847 kg/m^2

μ (viscosity of the resin) = 0.0953 Pa.s

P_{inj} (injection pressure) = 49.7 kPa

Fiber volume fraction (based on measured mass, see equation 2.2) and porosity were calculated by using below equations:

$$V_f = \frac{0.205}{(0.22 \times 0.22)\ (0.004)\ (2550)} = 0.414 = 41.4\% \tag{2.13}$$

$$\phi = 1 - V_f = 0.585 = 58.5\% \tag{2.14}$$

2D unsteady permeability components ($K_{uns,0}$ and $K_{uns,90}$) were determined by extracting the flow front propagation versus time data from the video recording of the experiment. For 0^o direction and 90^o direction, captured data is shown in Fig. 2.17.

F_0 and F_{90} was calculated by using the data given in Fig. 2.17 and the equation below (detailed in section 4.2):

$$F_0(t) = K_{uns,0}t = \frac{(0.0953)(0.585)}{4(49700)}\left\{r_{f,0}^2\left(2ln\left(\frac{r_{f,0}}{r_i}\right) - 1\right) + r_i^2\right\} \tag{2.16}$$

$$F_{90}(t) = K_{uns,90}t = \frac{(0.0953)(0.585)}{4(49700)}\left\{r_{f,90}^2\left(2ln\left(\frac{r_{f,90}}{r_i}\right) - 1\right) + r_i^2\right\} \tag{2.17}$$

In equation (2.16) and (2.17), $r_{f,90}$, $r_{f,0}$, and t were determined by the data given in Fig. 2.17. and curve fit was applied to the data as shown in Fig. 2.18. The slope of each curve was assigned as $K_{uns,0}$ and $K_{uns,90}$.

$$K_{uns,0} = 4.96 \times 10^{-10}\ \text{m}^2$$
$$K_{uns,90} = 1.22 \times 10^{-10}\ \text{m}^2$$

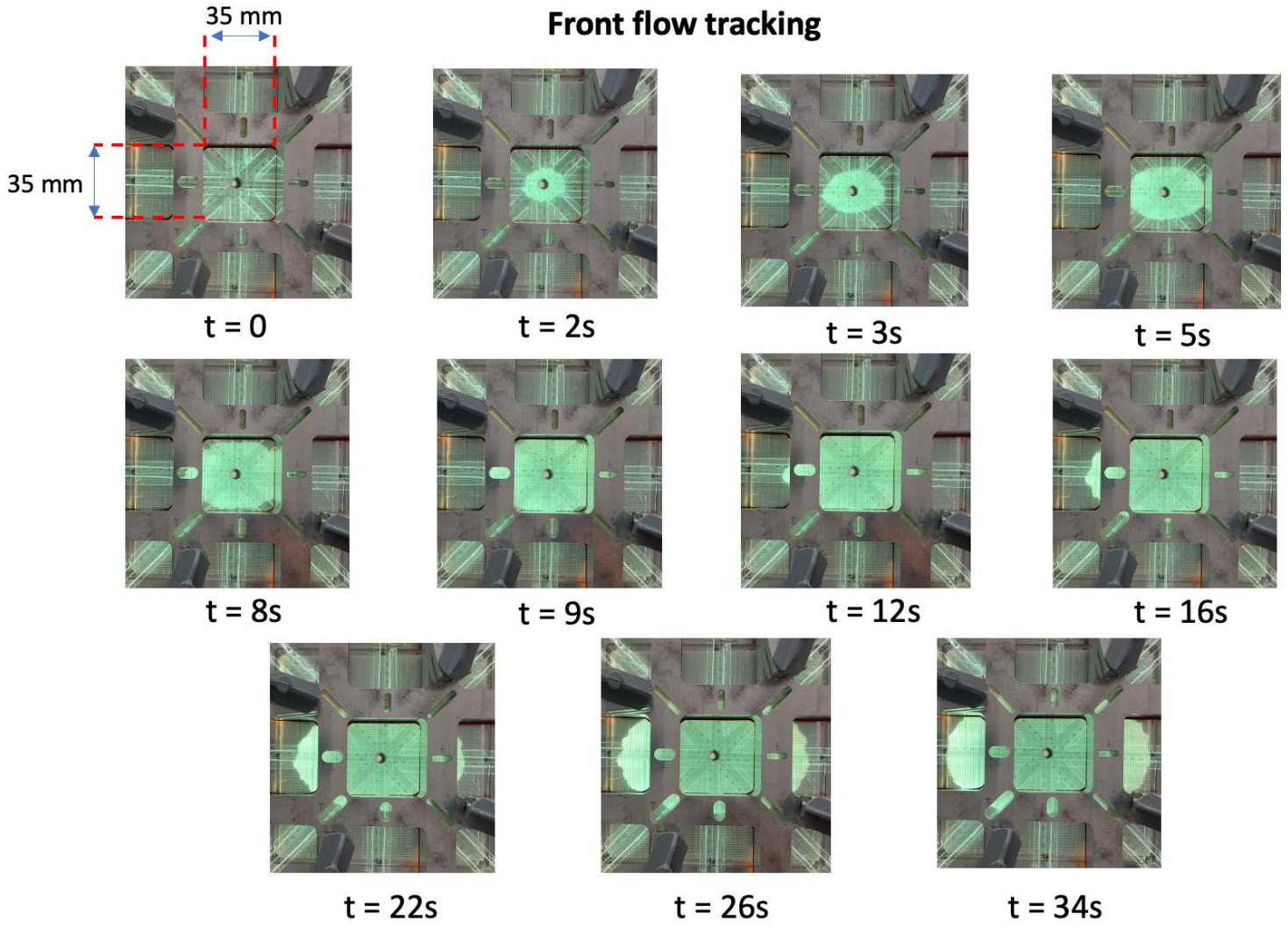

Figure 2.17 Flow front versus time recordings (captured from a video recording)

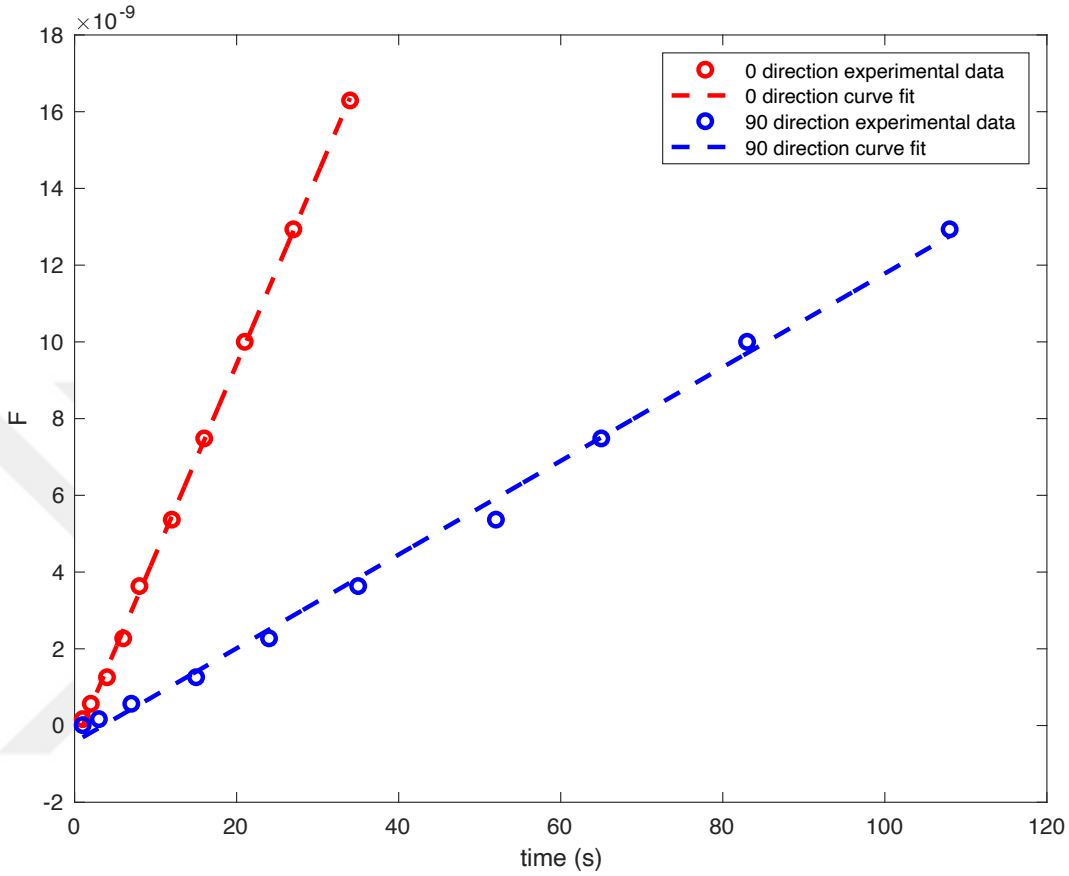

Figure 2.18 F versus time data for 0° and 90° directions (see equations (2.16), (2.17))

Chapter 3:
COMPACTION (COMPRESSIBILITY) CHARACTERIZATION OF FABRIC PREFORMS

Compaction (Compressibility) Characterization of Fabric Preforms Variation of thickness in a finished composite part is known as one of the major drawbacks of the VARTM process. This phenomenon happens due to two main reasons which can be listed as: 1) non-uniform and irregular nature of the fabric structure, and 2) change in resin pressure in a mold which induces variation of the compaction pressure. In RTM, rigid upper mold half is used, whereas a flexible vacuum bag is used in VARTM which is more prone to deformation [27-28].

Compaction behavior of the material used in composite material manufacturing plays an important role to understand the underlying physics of VARTM process which includes thickness evolution and variation in fiber volume fraction, V_f, as compaction pressure changes as a function of space (x, y) and time (t). Resin bleeding (drain of excessive resin) is one of the common solutions to decrease the variation in part thickness [27]. In resin bleeding, the inlet is closed after the fabric preform is completely impregnated by the resin while keeping the exit open to drain excessive resin. Resin pressure and thickness of the part can be settled and homogenized by this method. However, the most important issue regarding resin bleeding is that the required time for homogenization of resin pressure and part thickness is hard to estimate and resin starving regions may be formed by this post-filling application if it is applied for a long time interval [29-30]. As a result, mechanical properties of the final part can be adversely affected. Thus, it is essential to understand the relationship between the compaction pressure and part thickness in order to be able to manufacture composite parts with acceptable dimensional tolerances.

3.1 Thickness Variation in VARTM

In VARTM, air is evacuated from the mold by a vacuum pump. The mold has a rigid half at the bottom and a flexible vacuum bag at the top. This pre-injection vacuuming compacts the preform and the resin is infused. During pre-injection (dry compaction), compaction pressure, P_c, is developed by the difference between the ambient atmospheric pressure, P_{atm}, and the inner vacuum pressure, P_{vacuum}. Usually, resin pressure, P_r is assumed

to be the inner pressure after the resin infusion starts, which varies with time and location ($P_r = P_r(x,y,t)$, where x and y are spatial coordinates, t is time). Therefore, at a fixed location, the compaction pressure decreases as the resin pressure increases with time:

$$P_c(x, y, t) = P_{atm} - P_r(x, y, t) \quad (3.1)$$

The major cause of the spatially varying nature of thickness can be explained by equation (3.1) and similarly variation in thickness, h, can be expressed in terms of coordinates (x,y) and time (t), h (x,y,t). The illustration of thickness evolution during mold filling stages can be seen in Fig 3.2 illustrates the thickness evolution during mold filling stage in VARTM.

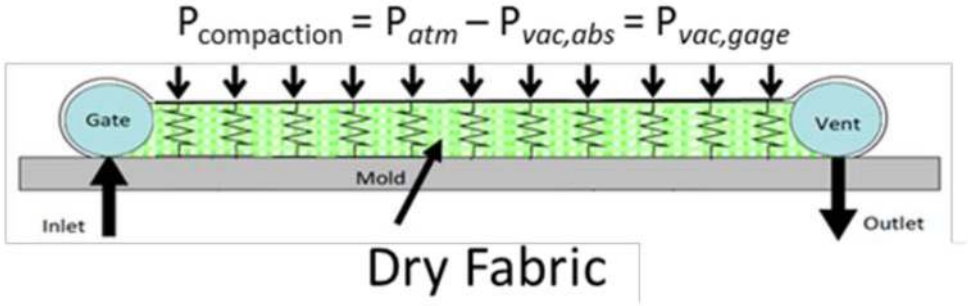

Figure 3.1 Schematic of VARTM during initial vacuuming (pre-infusion, the fabric is dry) [31]

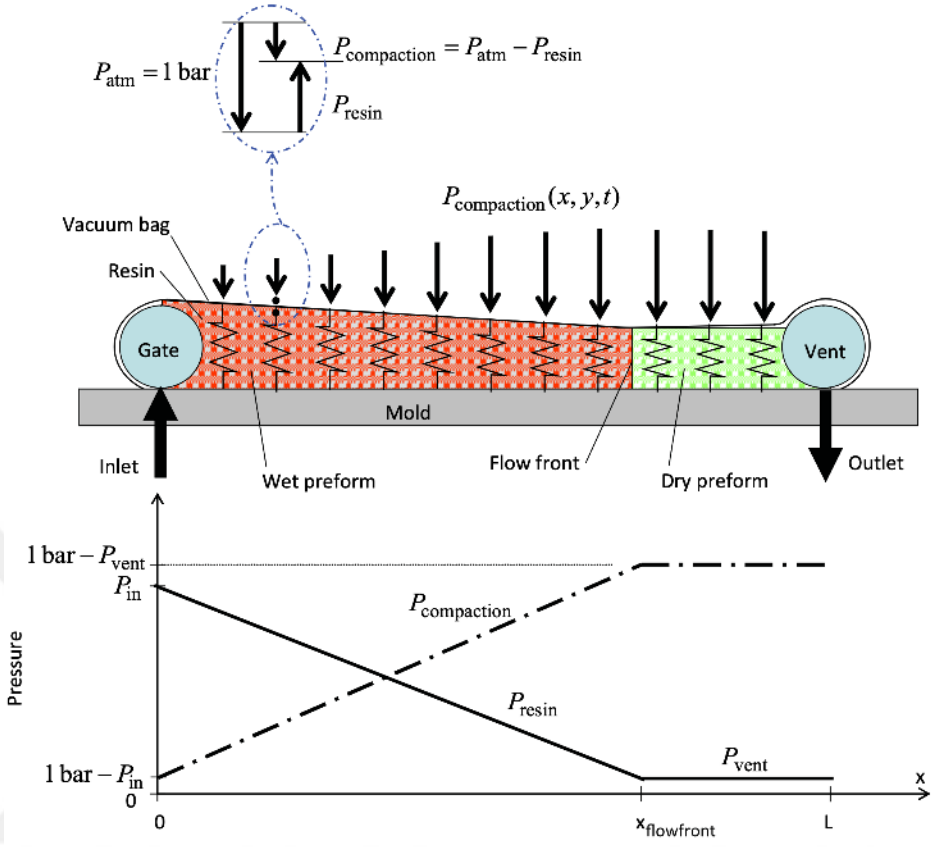

Figure 3.2 Schematic of VARTM during resin impregnation (unsaturated flow) [31]

3.1.1 Compaction Characterization Models in Composite Manufacturing

Compaction characterization experiments are conducted to observe and model the behavior of the materials used in composite manufacturing (fabric preform) by changing (i.e., controlling) compaction pressure and measuring the corresponding thickness. Two types of characterization models are present in the literature: 1) elastic models, 2) viscoelastic models. The response of the fabric is if the part thickness changes with time when the compaction pressure is kept constant. It was stated that, below 20kPa of compaction pressure, it takes significant amount of time for the thickness to reach a steady value [27]. Due to their simplicity and independence from time, elastic models are commonly used to characterize compaction behavior of many materials including fabrics. In elastic models, a static relationship between the part thickness and the compaction pressure is assumed. Thickness of the fabric preform and fiber volume fraction are inversely related: $V_f = f(1/h)$. The

response to the change in compaction pressure is instantaneous in which the part thickness is immediately changes after the compaction pressure is set to a new constant value. This elastic behavior is often expressed by fitting a power law to the experimental outcomes to obtain a relationship between compaction pressure, P_c and fiber volume fraction [38-39]:

$$V_f = AP_c^B \tag{3.2}$$

in which constants A and B are determined by fitting the curve to the experimental data.

3.1.2 Thickness Monitoring by Using Structured Light Scanning (SLS)

There are various tools and approaches employed in the literature to investigate the thickness versus compaction pressure relationship. Some of these tools are dial gages, linear variable differential transducers (LVDT), laser displacement sensors and digital speckle photography (DSP) [27-30, 36, 41, 51]. Usually, these approaches either require a contact with the part leading to an inaccurate thickness measurement due to deformation or only capable of measuring the thickness of a single point. In some of them it is uncertain if the same features will be matched in repeated measurements (as in DSP where multiple images from different angles are matched to obtain the thickness distribution with respect to a reference plane).

Structured Light Scanning (SLS) is one of the powerful optical measurement techniques that allows full-field thickness monitoring of an object without physical contact. The system consists of a projector and a camera which are operated by a software called DAVID [42]. Essentially, the amount of phase shift with respect to a reference plane is calculated to extract the thickness profile. A projector illuminates a series of fringe patters to the surface in the absence of an object which are captured by the camera and stored as a reference data. Then, an object is placed and fringe patterns are projected once again which are distorted by the part thickness as depicted in Fig. 3.3. This distorted pattern is captured by the camera and used to measure the amount of distortion by calculating the variation from the reference data to obtain full field thickness distribution.

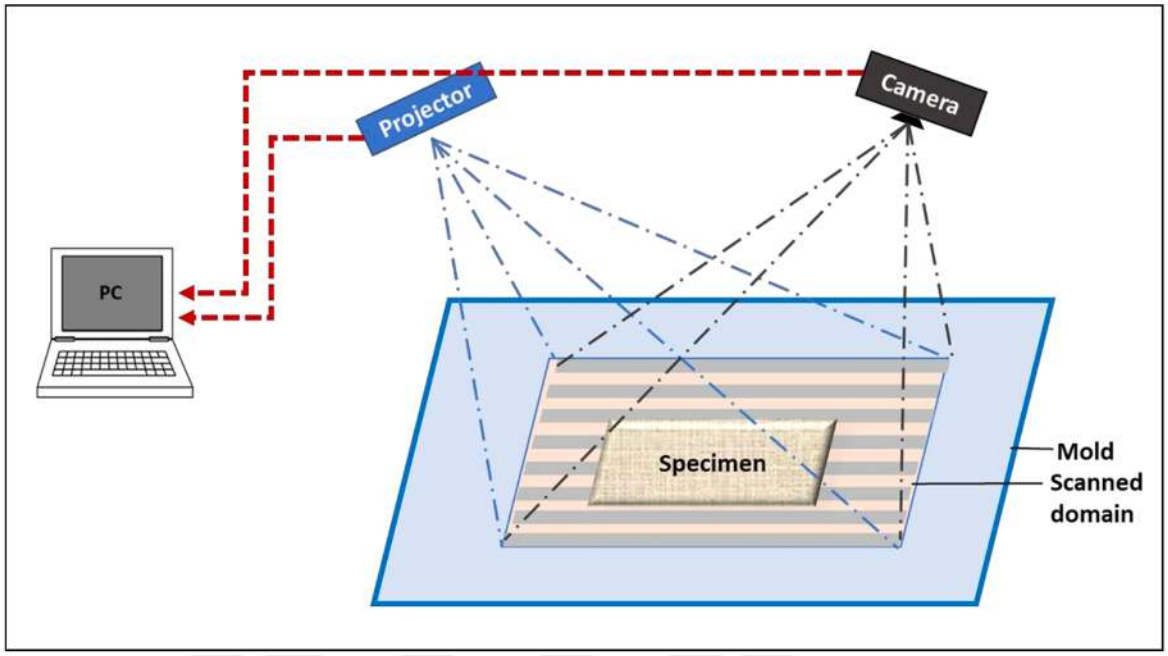

Figure 3.3 Schematic of Structured Light Scanning (SLS) setup (adapted from B. Caglar' s PhD. Thesis [36]

In this study, fringe patterns consist of vertical and black stripes (see Fig. 3.4) which are alternating continuously for 5 seconds (as illustrated in Fig. 3.5). The system is isolated from any vibration source and ambient illumination is minimized to maintain a constant level of illumination during the operation in order to obtain accurate measurements. The fringe patterns used in this study and the sequence of the patterns can be seen in Fig. 3.4.

Figure 3.4 V-shaped calibration panel of the SLS system: (a) side view, (b) top view

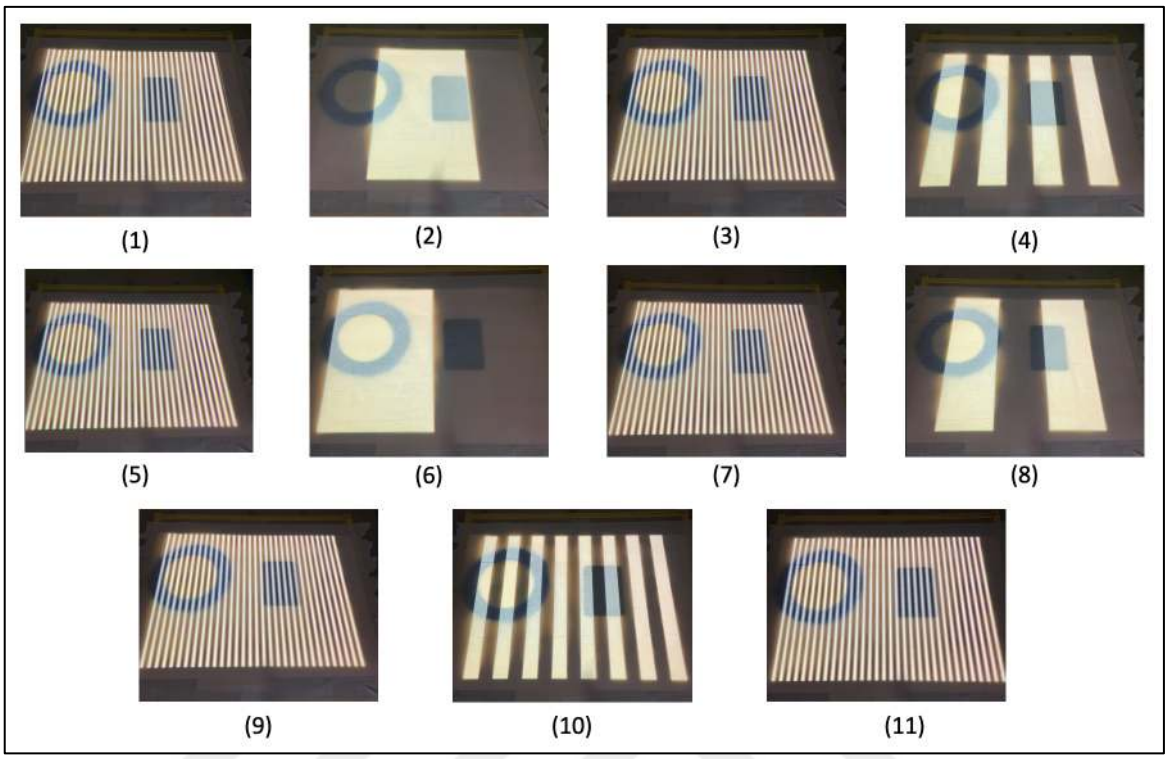

Figure 3.5 Fringe patterns: the sequence of the projected patterns is indicated by numbers 1-11 (circular object is the distribution medium wrapped around the circular fabric preform, rectangular object is the test piece)

In this study, a Canon EOS550 camera and a Casio XJ-A140 projector are used. The projector is zoomed and focused to the region where the measurement will be made, and the camera and the projector are connected to the computer before the David software is run. From the software, the connected camera and the projector are introduced to the software as the devices for scanning. In order to obtain accurate and consistent measurements, the system is calibrated. To perform the calibration, a V shaped calibration panel (see Fig. 3.5) which consists of orthogonal pair of two plates containing quadratically packed dots and 6 rings. These rings must be visible to the camera, and this is ensured by adjusting the focus and the brightness of the projector [37]. After the system calibration is completed, the scanning process can be started. The orientation of the system must be kept fixed for a reliable measurement.

3.1.3 Accuracy of the SLS system

In order to measure the accuracy of the SLS system, thickness distribution of a rectangular test piece (plexiglass), was measured by the SLS system at different locations of the scan domain. It was previously shown that covering the top surface of the scanned piece with white paper tape reduces the reflection and improves the accuracy of the SLS system [41]. Thus, the top surface of the test piece was covered with white paper tape as shown in Fig. 3.6, including the dimension measured by a digital caliper. The thickness of the test piece at its center was measured as 5.20 mm. In addition, the thickness at the center of each quarter of the test piece was measured and provided in Fig 3.6(b).

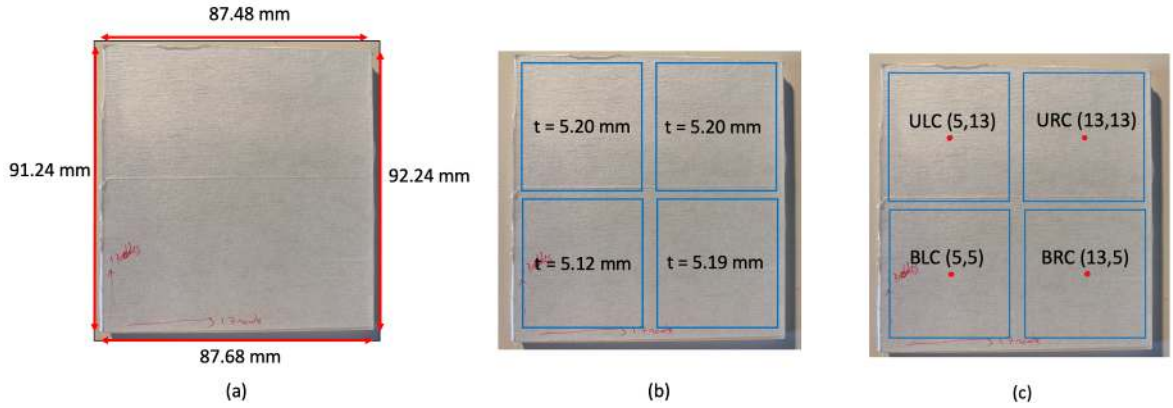

Figure 3.6 Rectangular test piece used in accuracy measurement of the SLS system (covered with white paper tape): (a) outer dimensions, (b) measured thickness (t) of each quarter region (quarter regions are indicated as blue squares, (c) with the center node of the each subdomain (ULC, URC, BLC and BRC are the names of each node i.e. ULC is upper left center node, BRC is bottom right center node, and so on).

In order to see the variation of the SLS-measured thickness depending on the location of scan, the test piece was placed at different locations of the scan domain (See Fig. 3.7) and scanned twice at each location. The average thickness of the subdomains was calculated in MATLAB by post processing the scan files. In the current setup, the size of the scan area is 220 mm x 355 mm which is discretized by a 45 x 72 mesh with 5 mm distancing in both axis. Accordingly, the test piece is represented by approximately 16 x 17 nodes. Two different approaches were used to measure the accuracy of the SLS setup: 1) the average of thickness values of the nodes that correspond to test piece (16 x 17 nodes) was calculated, 2) the thickness of the nodes that are at the center of each quarter region of the test piece were

controlled, 3) the average of the thickness of the nodes that correspond to each subdomain was calculated. The center nodes of quarter regions are given in Fig. 3.6 (c).

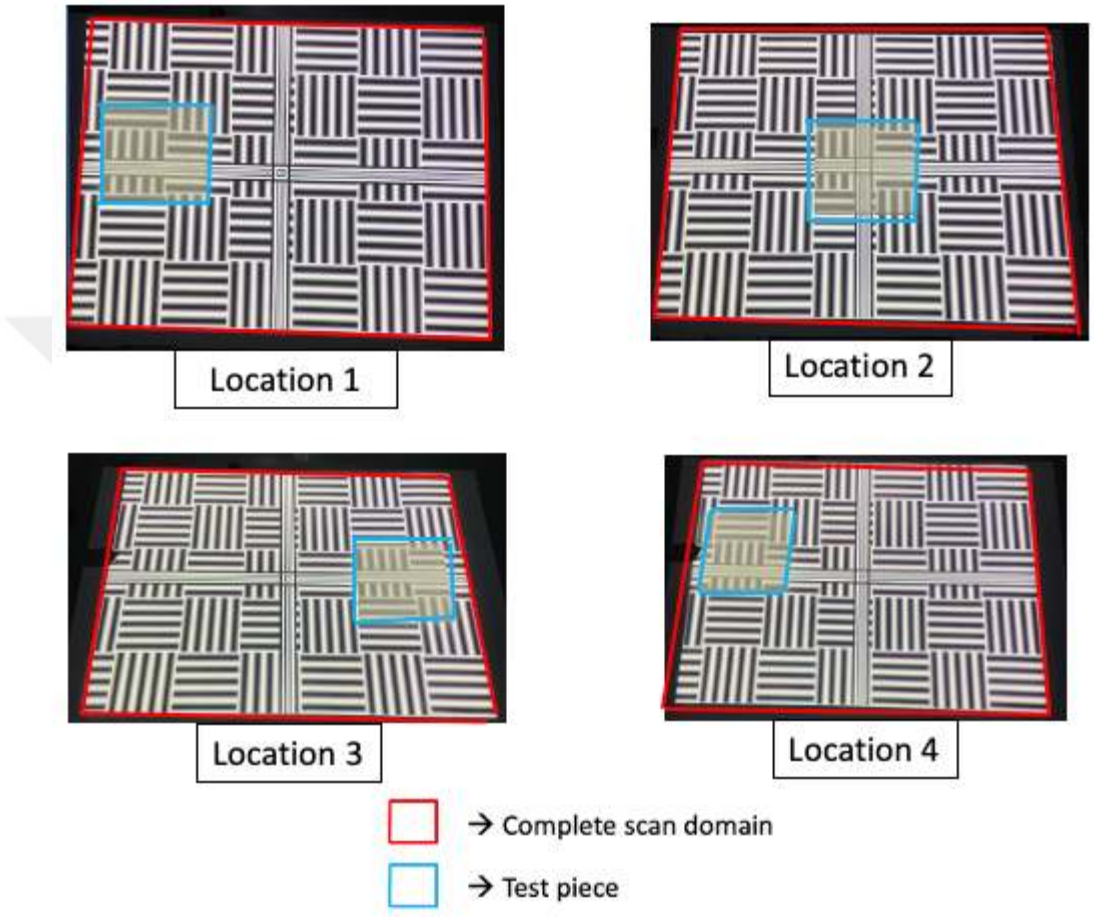

Figure 3.7 Complete scan domain vs. test piece at different scan locations. Note that Location 1 and Location 4 slightly differ from each other. Location 4 indicates the location of the fabric specimen during the compressibility characterization experiment whereas Location 1 is the middle of the right edge of the scanned area

The measured average thickness of the test piece which is scanned twice at each of the scan locations are given in Fig. 3.8. The average of 8 scans is 4.66 mm (green dashed line in Fig. 3.8), where the actual thickness of the test piece is 5.20 mm. The error between average SLS-measured thickness and the actual thickness of the test piece is significant, however, when the same test piece is scanned consecutively, the deviation between average measured thicknesses are very low (red stars in Fig. 3.8) indicating repeatability of the SLS-measurements.

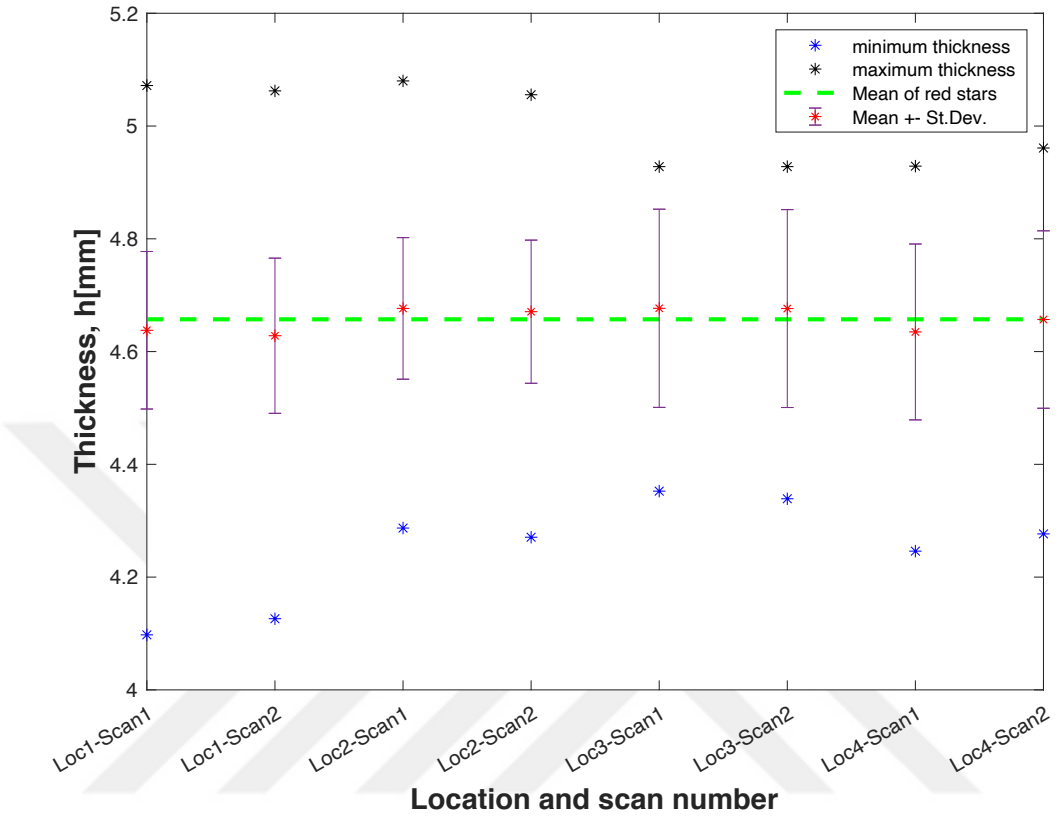

Figure 3.8 Measured thickness of the test piece for different scan numbers and scan locations

For a more detailed analysis, the center node of each quarter region (ULC, URC, BLC, BRC) was controlled (see Fig. 3.6(c)). Average thickness of each center node was plotted for Scan 1 and Scan 2 at different locations as shown in Fig. 3.9. The maximum error between Scan 1 and Scan 2-thicknesses of the same node is obtained as 1.26% (See Appendix A). The mean of the Scan 1 and Scan 2-thicknesses is also given in Appendix A for the different scan locations, showing that there is a negligible error between thicknesses of consecutive scans and also it can be concluded that the scan location has a little influence on measurements, however it is still negligible. This outcome demonstrates the performance of the SLS system in repetitive scanning operations. In short, there is a higher error between the actual thickness and SLS-measured thickness of an object, however, since the thickness of an object is repeatedly measured the error is negligibly low.

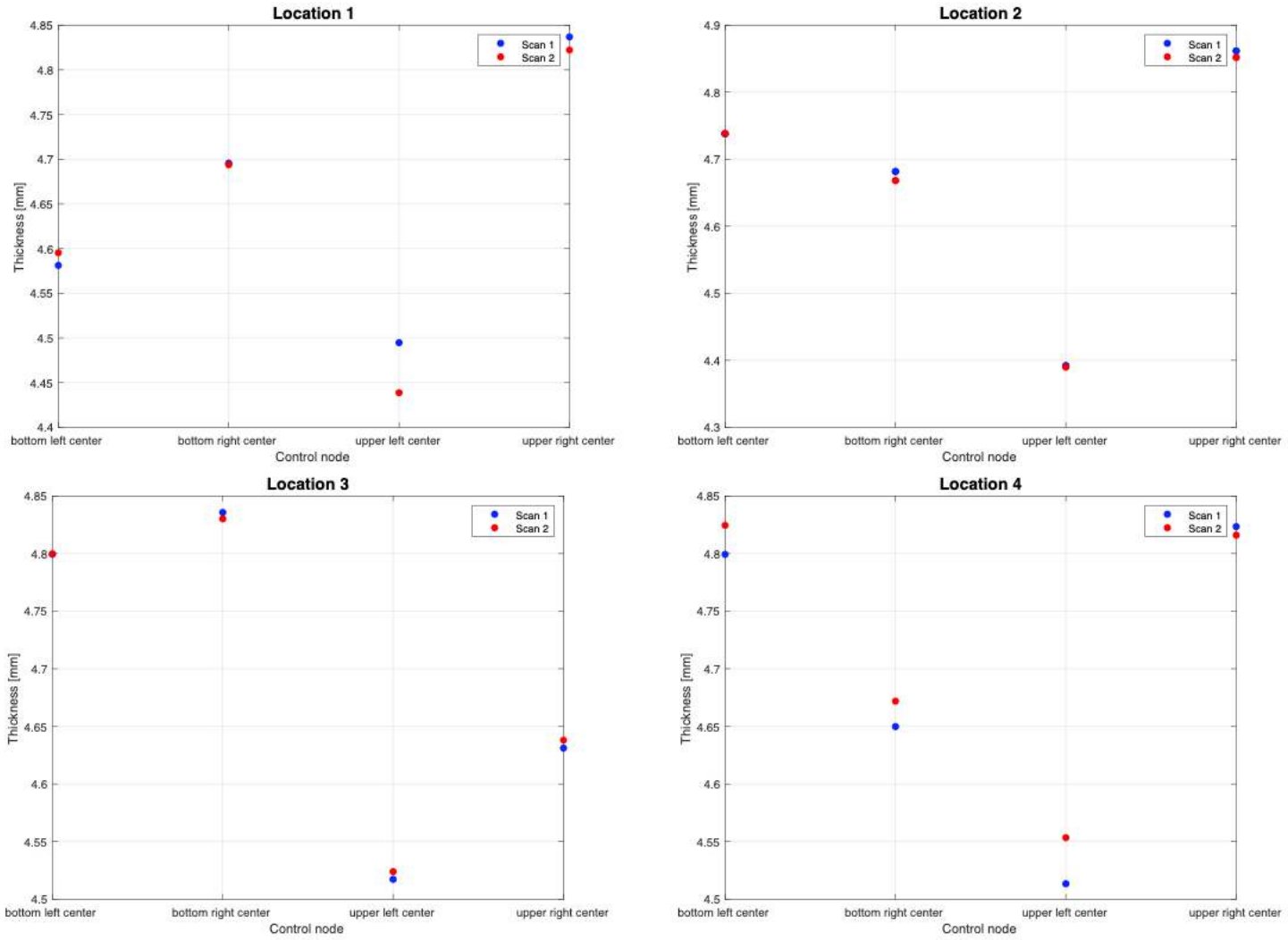

Figure 3.9 Measured thickness of the control nodes at different locations for the 1st and 2nd scan

3.2 Experimental Setup for Compaction Characterization

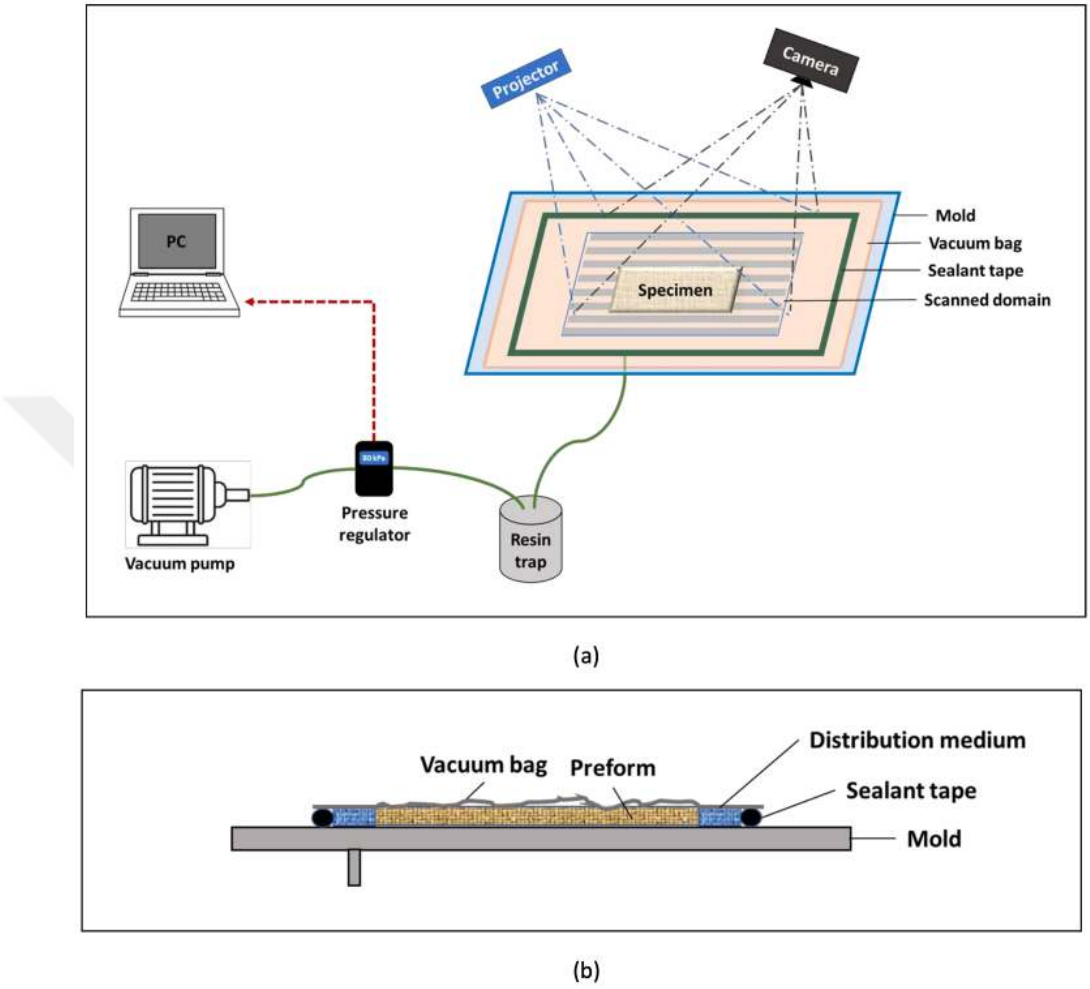

Figure 3.10 Compaction characterization setup: a) with SLS system, b) side view of the mold (adapted from Baris Caglar's PhD. thesis [36])

Compaction characterization setup used in this study is seen in Fig. 3.10, which consists of DAQ, a pressure regulator, a vacuum pump, SLS system (for thickness monitoring) and a mold. The fabric is compacted by the vacuum pump which is controlled by SMC ITV2090 pressure regulator controlled by a computer. The pressure regulator has an operational range of 1.3-100 kPa. A fabric specimen is placed on the mold and covered with a vacuum bag which is tightly sealed by a sealant tape to form a vacuum environment. The thickness is monitored by the SLS system (detailed in Section 3.3). For technical details, see Yalcinkaya's study [40].

3.3 Setup Preparation

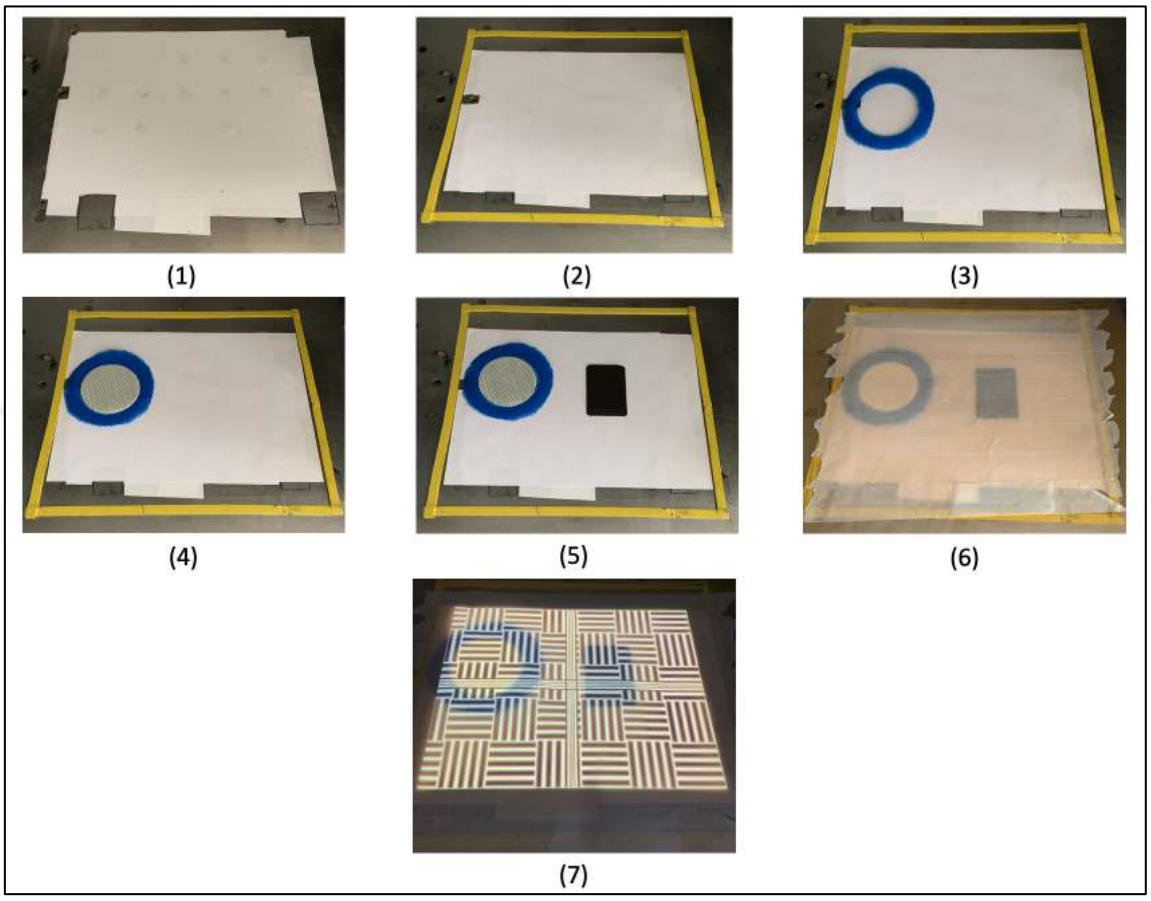

Figure 3.11 Steps of experimental setup preparation for compaction characterization (sequence is indicated by numbers 1-7)

Preparation procedure for a compaction experiment is shown step by step in Fig. 3.11. This setup has pressure sensors that are embedded in lower mold half (steel plate). These sensors are usually used in VARTM experiments but here they are useless for compaction characterization experiments. Thus, (1) they are covered with a white tape to form a flat reference plane for thickness monitoring. (2) Sealant tape is placed on the lower mold half. (3) Distribution medium (flow mesh) is used near the inlet to facilitate 1D flow. (4) Fabric preform is placed on the mold surface next to the flow mesh. (5-6) After placing the test piece (to check the accuracy of the measurements) it is covered with a vacuum bag. The surface of the vacuum bag reflects the light which can significantly affect the measurements due to high reflection through the lens of the camera used in SLS system. (7) To reduce reflection, tape

coating is applied on the vacuum bag and the fringe patterns are illuminated to the scan object before starting an experiment.

3.4 Compressibility (Compaction) Characterization Experiments

The experiments are conducted on a specimen made of 10 layers multiaxial E-glass NCF (See Section 2.1). In this study, compressibility of both dry and wet specimens will be characterized. To observe the effects of compaction and decompaction, pressure is applied at an increasing trend of 2, 5, 15, 30, 45, 60 and 75 kPa, then at a decreasing trend in backwards as 75, 60, 45, 30, 15, 5 and 2 kPa.

This setup has been previously used as a compaction characterization tool [41]. In the experimental schedule of our previous approach, 60 seconds were reserved between setting the pressure to a new level and scanning (to allow fabric to reach quasi steady state). In this new approach, 15 seconds fabric settlement time is proffered instead of 60 seconds in previous approach. Note that there are 13 pressure levels in a single compaction-decompaction cycle. The reason for this is that the camera used in SLS setup heats up due to high exposure and automatically turns of approximately 18 minutes after it is turned on. However, it's important to conduct compressibility experiment for a number of consecutive compaction-decompaction cycles to characterize the behavior of the fabric. Here, the experimental schedule is updated to achieve 3 compaction-decompaction cycles within the mentioned time limitation of the setup. Thus, before conducting a compressibility characterization experiment, required fabric settling time was tested by a test experiment where for each pressure level, the compressed fabric is scanned twice: 15 seconds and 30 seconds after the pressure level is set. No significant difference between the thicknesses at 15 and 30 seconds was observed (see Appendix B). For the sake of camera use and having as many cycles as possible, it was decided to scan the compressed fabric specimen 15 seconds after each pressure level is set.

The compaction pressure versus time graph shown in Fig. 3.12 illustrates the experimental schedule for the compaction and decompaction stages for a single cycle which

takes approximately 7 minutes. After each desired pressure level is set, it is maintained in that level for 15 seconds (black lines) and the specimen is scanned which takes 5 s approximately (red lines). After each scanning, 10 seconds is reserved for saving the scanning data (blue lines in Fig. 3.12) before setting the pressure to the next level.

Instead of using the whole specimen area (200mm × 100 mm) for the average thickness calculation, a narrower region near the center which has dimensions of 45 mm × 45 mm is selected to prevent any measurement error since the vacuum bag accumulates near the edges of the specimen. The fiber volume fraction is calculated as:

$$V_f = \frac{n\rho_{sup}}{\rho_f h} \tag{3.3}$$

where n is the number of layers, h is the thickness of the specimen, ρ_{sup} is superficial density of a single fabric and ρ_f is the bulk density of the E-glass fiber. It should be noted that h is measured for each pressure level separately. Compaction pressure versus fiber volume fraction data is fitted to an exponential curve, $V_f = AP_c^B$ where constants A and B are determined by least square method as also done in [40].

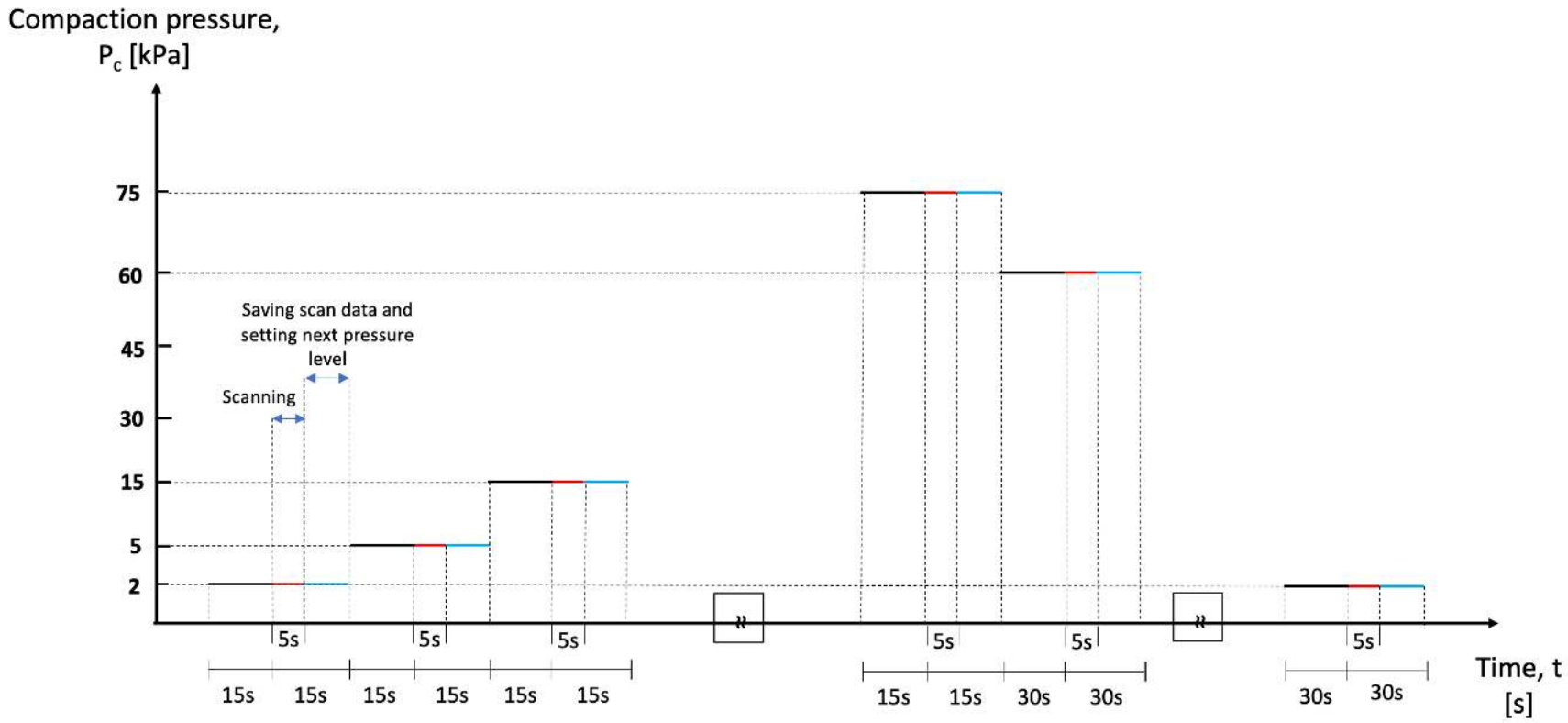

Figure 3.12 Compaction pressure (Pc) vs. time (t) schedule for a compaction characterization experiment

3.5 Analysis of the SLS System for a Compaction Characterization Experiment

To evaluate the performance of the SLS system on compaction characterization of a multiaxial NCF, two experiments were conducted using the Pc versus t schedule given in Fig. 3.12. Ten layers of dry multiaxial fabrics were stacked by carefully aligning production direction of each layer. The results of the first and second compaction characterization experiments of the same fabric stack and the percentage change between them are shown in Fig. 3.13. In addition, fiber volume fraction of the fabric preform at each pressure level is shown in Fig. 3.14 for 1st and 2nd test experiments.

Although three compaction-decompaction cycle was planned and successfully completed in the first compaction characterization experiment (see Fig. 3.13 (a)), during the decompaction of the fabric preform during third compaction-decompaction cycle of some experiments, the measurements were interrupted as the camera automatically turned off due to overheating. This clearly shows that the third compaction - decompaction cycles may not be achieved in every experiment. Available time for an experiment is dependent on the time spend for the calibration of the SLS system where the calibration time is uncertain since the camera is very sensitive to a slight change in orientation. In order to investigate the effect of the fabric settling time on average thickness, a small study was conducted in which the settling time of 15 s and 30 s were compared. The same pressure values for compaction and decompaction was used (see Fig. 3.12). The fabric stack was scanned twice for each pressure level at t = 15 s and 30 s after the pressure level is set. Appendix B shows the average thicknesses obtained for each pressure level. The thickness values at 15 s and 30 s vary slightly. However, no significant difference was observed.

It is important to note that, a similar study has been previously made by [41] for 30 s and 60 s fabric settling time using a core material. The difference between the thickness at the minimum compaction pressure (2 kPa) and maximum compaction pressure (78 kPa) is larger (up to 9 mm) due to the high porosity and low density of the core material used in those experiments. Thus, less scatter between 30 s and 60 s scans have been observed. However, for the fabric stack used in the compaction characterization experiments made in this study, the difference of the average thicknesses at the minimum compaction pressure

level (2 kPa) and maximum compaction pressure level (75 kPa) is significantly lower (≈ 1 mm) compared to the preform used in [41]. The error between 15 s and 30 s scans are shown in Appendix C.

(a)

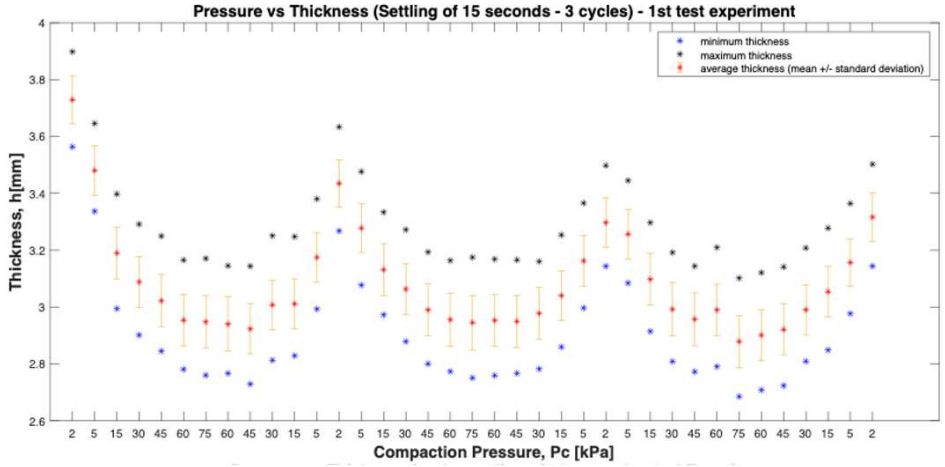

(b)

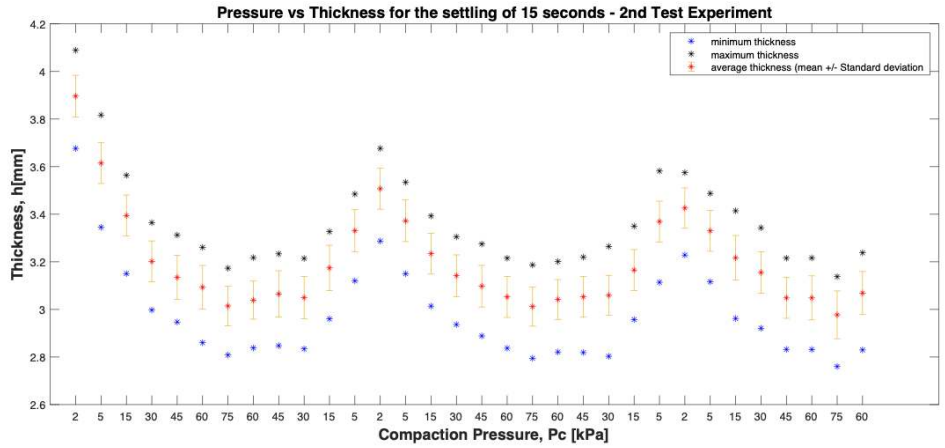

(c)

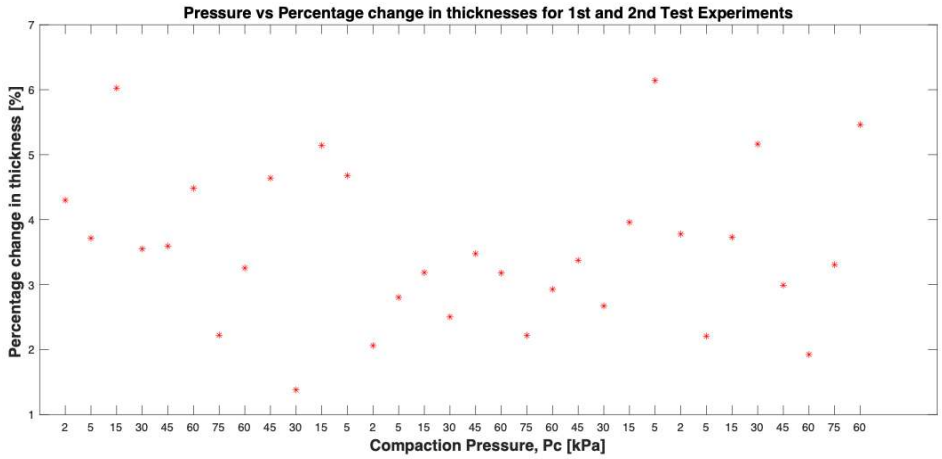

Figure 3.13 Compaction pressure (Pc) vs. thickness (h) data for: (a) first compaction characterization experiment, (b) second compaction characterization experiment, (c) percentage change between 1st and 2nd experiments

(a)

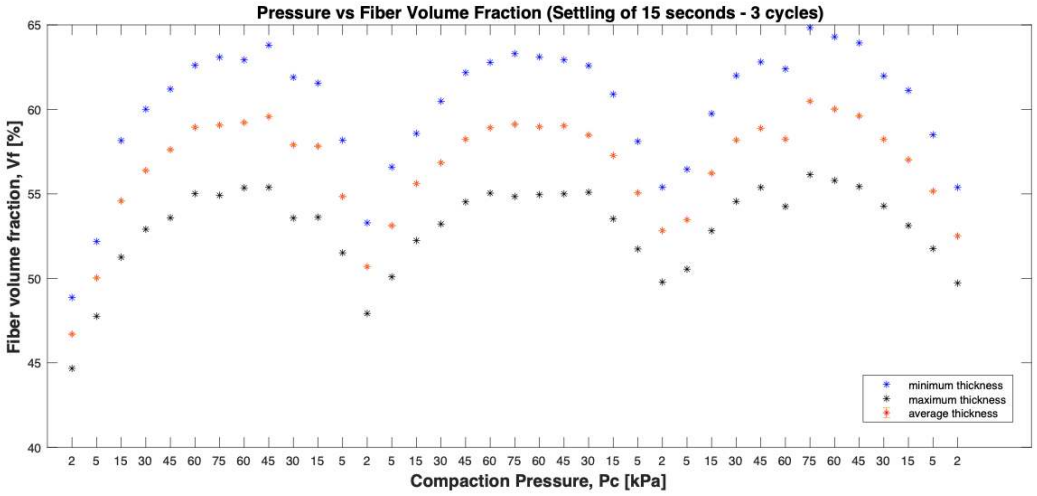

(b)

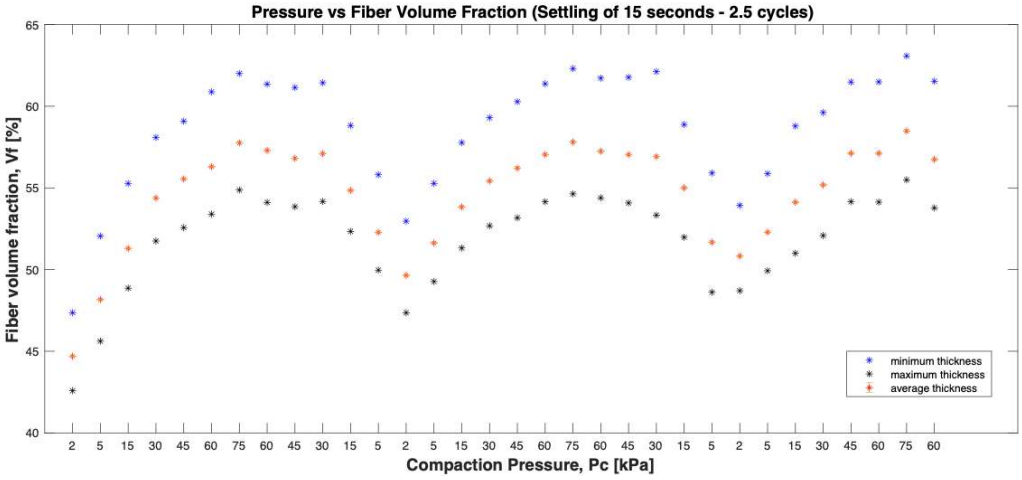

Figure 3.14 Compaction pressure versus fiber volume fraction for (a) 1st experiment, (b) 2nd experiment

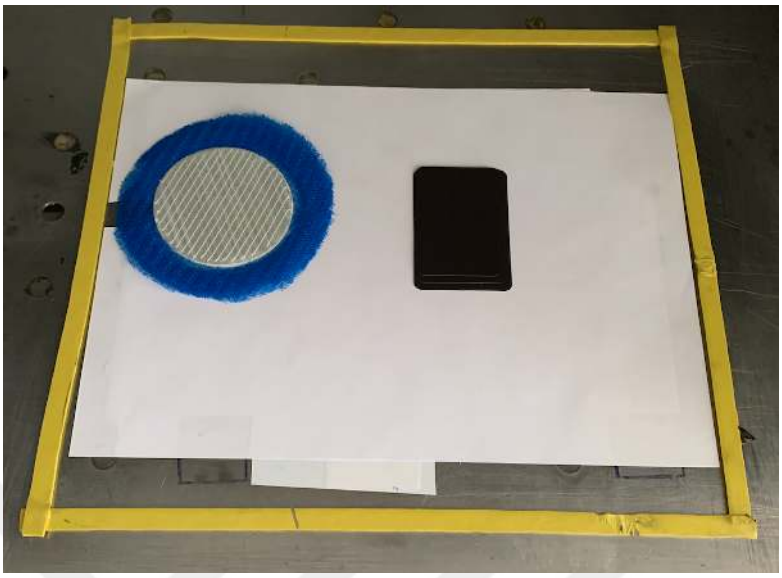

Figure 3.15 Fabric stack (white) on a flow mesh (blue) and a rigid rectangular test piece (black)

The most important issue regarding the SLS measurement is its low accuracy. As mentioned previously in Section 3.2.3, the thickness of the test piece was measured 89% of its actual thickness (with the error of 11%) . When conducting the first and second compaction characterization experiments (See Figure 3.13) another test piece with the thickness of 2.39 mm was placed next to the fabric stack as shown in Fig. 3.15. Even if the test piece is enclosed by a vacuum bag and different compaction pressures was applied on it, no deformation was expected since the test piece is assumed. Fig. 3.15 depicts the variation of the measured average thickness for each pressure level. The mean of average thickness measured by the SLS system for the test piece is 2.19 mm with the error of 8.3% (green dashed line in Fig. 3.16).

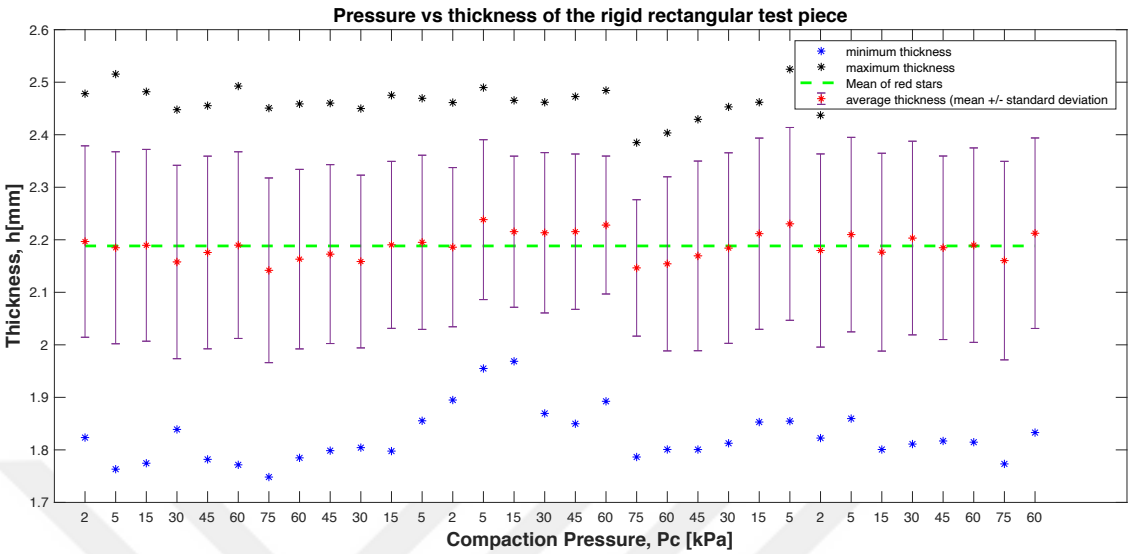

Figure 3.16 Compaction pressure vs. thickness plot of the rectangular test piece

Previously in Section 3, the error on measured average thickness of another test piece was 5-15 % in negative direction (actual thickness of the object is higher). In this study, similar trend was observed within the previously characterized margin of error. Thus, it can be said that the measurement of the SLS system deviates from the actual thickness in negative direction within the given error margin. Thus, it can be said that the thickness values measured for the first experiment and second experiment (See Fig.3.13) are actually 8-15% lower than the actual thickness of the fabric preform for each pressure level.

SLS system was used in the scope of a compressibility benchmark exercise to conduct total of 10 compaction characterization experiments (5 for dry preform, 5 for wet preform). However, results will not be shared in this thesis for the confidentiality agreement.

Chapter 4:
MODELLING OF DUAL SCALE PERMEABILITY IN FABRIC PREFORMS

4.1 Permeability Modelling of a Dual Scale Porous Medium

One of the typical examples of a dual scale flow is flow through a woven fabric structure which consists of two sub domains: (1) the interconnected network of tows (bundles) that are woven together (the region between individual fibers in a bundle of fibers, a.k.a. intra tow region), (2) channels and pores between the tows (inter tow region) [13]. This dual scale nature of a woven fabric results in micro-scale flow in intra yarn region and meso-scale flow in inter yarn region. Graphical illustration of micro and meso-scale flows can be seen in Fig. 4.1**.** Compared to large channels created between the tows in which the distance between the tows is in the order of millimeters, the distance between individual fibers within a tow results in a slower flow in intra tow region. This delayed impregnation may induce formation of voids and partial saturation of flow front [21-22]. Thus, it is important to understand flow physics in dual scale media. The most common approach to model dual scale flow is unit cell approach, where the flow domain is defined as the smallest repeatable part of the fabric architecture (representative volume element) to represent entire volume [12-13,21-24]. This method reduces the computational cost significantly.

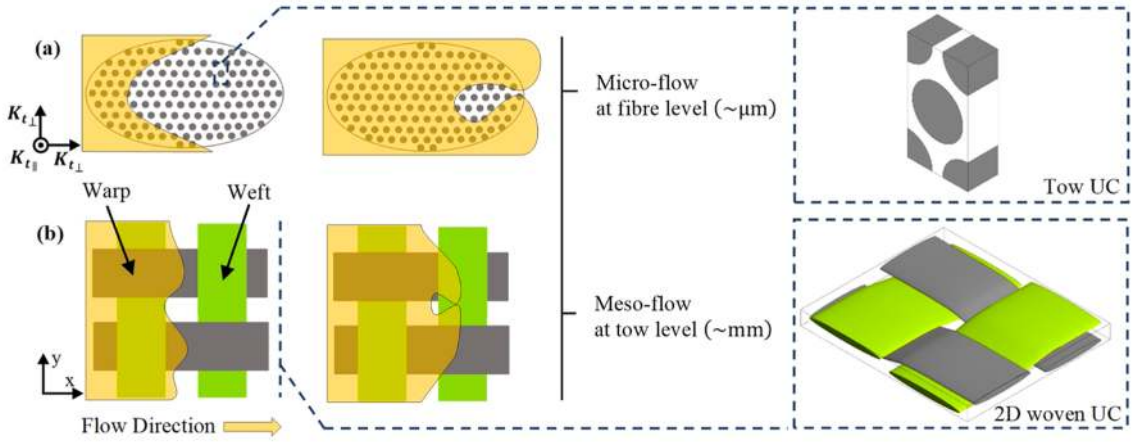

Figure 4.1 Resin impregnation in a) intra-tow region and b) between tows (inter-tow region) [22]

4.1.1 Methodology

In this chapter, we studied the same model and case study previously studied and implemented in ANSYS by Alotaibi et al. [22] was studied. They modelled a dual scale flow with two regions: 1) intra tow region, 2) inter tow region, where resin flow occurs within the individual fibers of warps and wefts (intra tows) and also in empty channels between warps and wefts (inter tow). Here the same model parameters were used as in [22]. After verifying our ANSYS solution prepared for this thesis will result in the same results as they presented in their publication [22], our study will be expanded to account for the non-uniformity in a fabric structure in the following sections.

In RTM and VARTM, the resin flow is assumed laminar since the inertial forces are dominated by viscous forces which is classified as viscous or creeping flow (where low Reynold's number is observed: Re<<1). Usually, the effect of intra tow permeability is included by adding a source term to the momentum equation which behaves as a sink. For laminar flow, the continuity and momentum equations are presented below [22]:

$$\frac{\partial}{\partial t}(\rho \mathbf{u}) + \nabla . (\rho \mathbf{u}\mathbf{u}) = -\nabla p + \nabla . \boldsymbol{\tau} + \rho \mathbf{g} + S \tag{4.1}$$

$$\frac{\partial}{\partial t} + \nabla . (\rho \mathbf{u}) = 0 \tag{4.2}$$

where $\frac{\partial}{\partial t}(\rho \mathbf{u})$ is the local acceleration term, $\nabla . (\rho \mathbf{u}\mathbf{u})$ is convective acceleration term, ∇p is the pressure gradient, $\boldsymbol{\tau}$ is the stress tensor, $\rho \mathbf{g}$ is the body force term and S is the source term. The transient term and inertial forces at the left-hand side of (4.1) is neglected for incompressible, quasi-steady, creeping flow, and ignoring the effect of gravitational acceleration (g), equation (4.1) and (4.2) are reduced to the following expressions:

$$-\nabla p + \nabla . \boldsymbol{\tau} + \rho \mathbf{g} + S = 0 \tag{4.3}$$

$$\nabla . (\rho \mathbf{u}) = 0 \tag{4.4}$$

To model the inter-tow region (where there is no porous region), equation (4.3) can be used by setting S to 0 for simulating Stoke's flow at the empty channels between the tows [22]. For the porous intra-tow region, source term S is introduced to the model which usually consists of viscous resistance as shown:

$$S = -\frac{\mu}{\boldsymbol{K}_t}\mathbf{u} \tag{4.5}$$

where μ is the viscosity of the fluid, $\frac{1}{\boldsymbol{K}_t}$ is the viscous resistance, $\mathbf{u}$ is the volume averaged velocity and $\boldsymbol{K}_t$ is the permeability tensor of the tow which can be determined analytically for idealized fiber arrangements by empirical solutions [16]. Once equation (4.5) is inserted into equation (4.3), Darcy-Brinkman equation is obtained for modelling of flow in porous media. Darcy-Brinkman equation is the generalization of Darcy's Law which matches the boundary conditions between the inter-tow and intra tow regions. Once the solution is obtained for the whole flow domain using Stoke' s flow in inter-tow domain and Darcy-Brinkman equation in intra-tow domain, Darcy's Law is reemployed to get overall permeability of the model as follows:

$$\overline{\boldsymbol{u}} = -\frac{\boldsymbol{K}_o}{\mu}\cdot\nabla p \tag{4.6}$$

in which $\overline{\boldsymbol{u}}$ is the volume averaged velocity vector, ∇p is the pressure gradient and $\boldsymbol{K}_o$ is the global permeability tensor. In terms of volume flow rate, Darcy's Law for x direction can be expressed as:

$$Q = -\frac{K_{o,xx}}{\mu}\frac{\partial P}{\partial x}A \tag{4.7}$$

where $K_{o,xx}$ is the global permeability and A is the cross-sectional area of the flow domain in x direction, $\frac{\partial P}{\partial x}$ is the pressure differential in x direction and Q is the inlet volume flow rate.

4.1.2 Intra Tow Permeability

Gebart et al. [16] presented an analytical expression, which is based on the lubrication theory for the permeability of idealized packing arrangements of fibers for: (1) flow perpendicular to the fibers, and (2) flow along the fibers (flow parallel to the fibers). The unit cell approach was employed to model the flow between fibers to represent the entire domain. The hexagonal and quadratic arrangements of unidirectional circular fibers can be seen in Fig. 4.2.

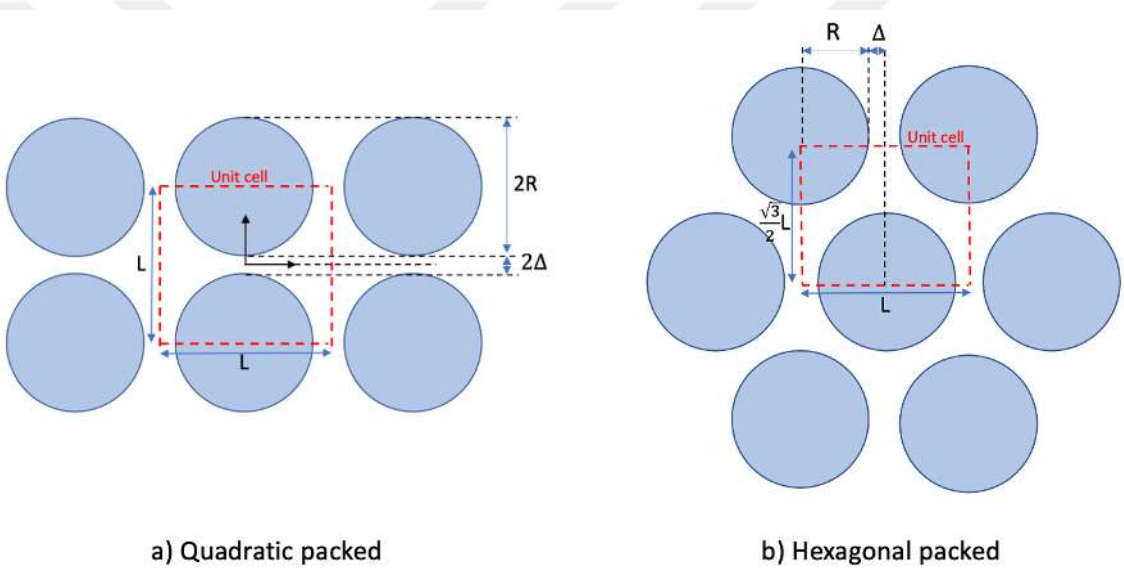

Figure 4.2 Unit cell of periodically packed fibers: a) quadratic and b) hexagonal [16]

In this study, hexagonal arrangement is assumed in intra-tow region. Analytical formulation for the flow perpendicular to the fibers and flow parallel to the fibers are expressed as shown below [16]:

$$K_{\perp\, hex} = \frac{16}{9\pi\sqrt{6}}\left(\sqrt{\frac{V_{fmax}}{V_f}} - 1\right)^{\frac{5}{2}} R^2 \tag{4.8}$$

$$K_{||\, hex} = \frac{8R^2}{c}\frac{(1-V_f)^3}{{V_f}^2} \tag{4.9}$$

in which, c is the dimensionless shape factor which takes different values depending on the duct cross section shape (for circular cross section of fibers, c is given as 57 for quadratic arrangement and 53 for hexagonal arrangement), R is the radius of a single fiber, V_f is the fiber volume fraction, V_{fmax} is the maximum fiber volume fraction that occurs when fibers are in contact with each other. Using these formulations, $\boldsymbol{K}_t$ can be calculated for different fiber volume fractions and fiber radii to be used as a model input for intra-tow region.

4.1.3 ANSYS Model for Dual Scale Permeability

Unit cell of a flat woven fabric is modeled by a commercial software package ANSYS as it was done in reference study [22]. Fig. 4.3(a) illustrates the representative volume element (RVE) used in the reference study with dimensions and appropriate boundary conditions where no-slip is assumed for top, bottom, and side boundaries of a rectangular domain. Similar RVE was designed here in our study using the same dimensions, excluding the inlet zone as shown in Fig. 4.3(b). In addition to the no slip boundary condition, symmetry boundary condition was applied to the top, bottom and side surfaces of the RVE as a second case with the intention of comparing the influence of different boundary conditions on the overall permeability.

The injection pressure of 10 kPa is assumed, and the inlet pressure was set to 10 kPa and the outlet pressure is set to 0 kPa accordingly. The density and viscosity were 1300 kg/m^3 and 0.15 Pa.s, respectively. This model assumes steady, single-phase, laminar, incompressible flow for a Newtonian fluid. Symmetry boundary condition for side walls of the rectangular domain was also assumed as an additional case study in this thesis. However, for a comparative study to determine the applicability and success of the model, results of the model in which the side walls are defined as solid walls (no-slip) will be compared to the reference study [22]. It is important to note that the boundary conditions and geometric details used here are the same with the reference study [22].

In the reference study, the size of the domain was given as 6.59 mm × 5.66 mm × 0.52 mm, and also additional 1 mm inlet region has been added as shown in Fig. 4.3(a)**.** Here, the additional inlet region was excluded from the model assuming that it is not expected to

have a significant effect on the results. The geometrical details of the woven fabric architecture used in the original study were stated as below:

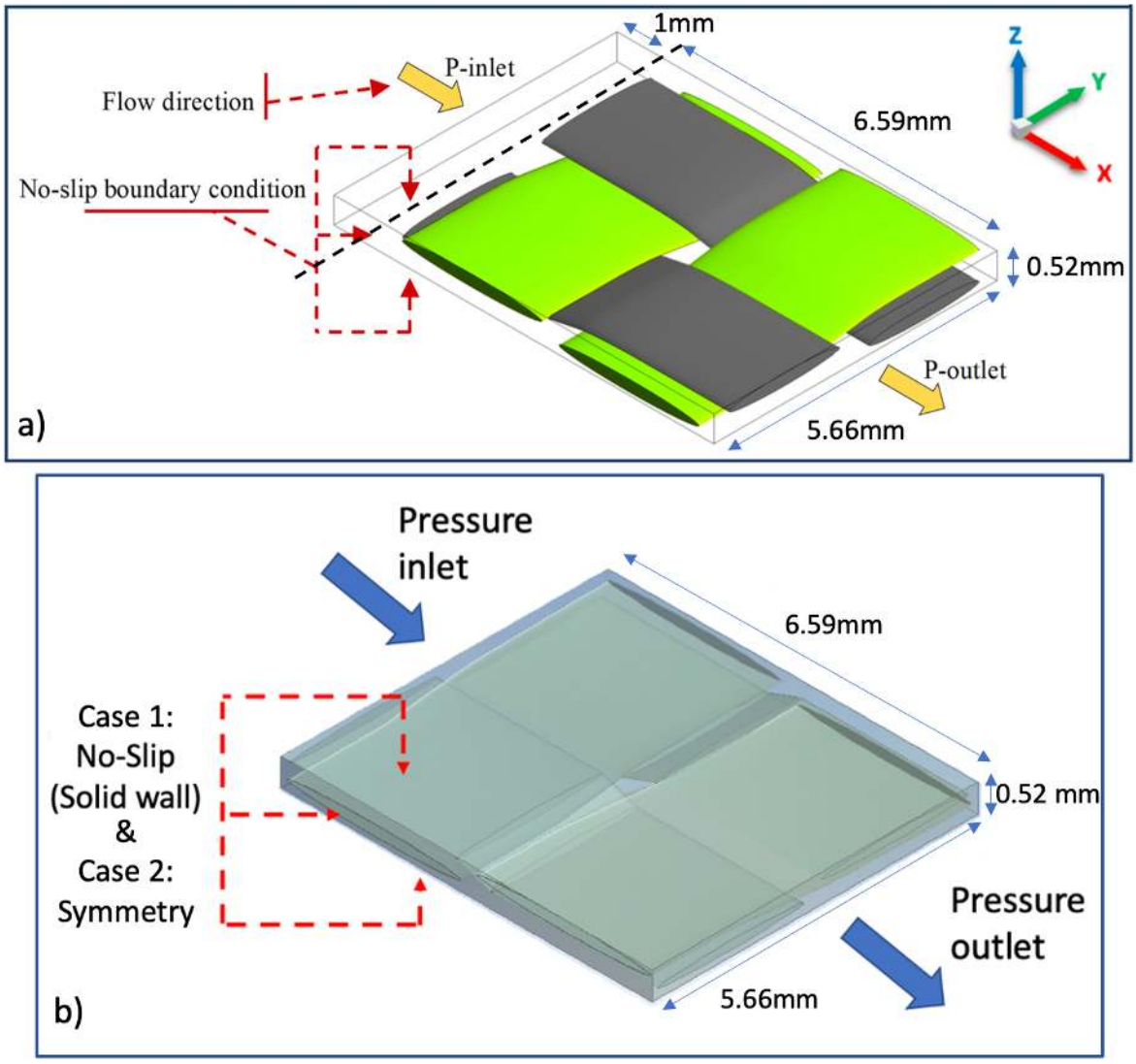

Figure 4.3 Flow domain, boundary conditions and RVE size of (a) the reference model (adapted from [22]) and (b) model prepared in this thesis

Table 4.1 Geometric details of the woven fabric architecture [22]

Parameters	Value	Units
Width warp yarns	2.21	mm
Gap warp yarns	0.58	mm
Width fill yarns	2.79	mm
Gap fill yarns	2.21	mm
Areal density	420	g/m^2
Specific density	2520	kg/m^3
Yarn tex warp	580	g/km
Yarn tex weft	600	g/km

The dimensions of the woven fabric modelled in reference [22] is shown in Fig. 4.4. The same geometry was used here too.

4.1.4 Mesh and Solution Scheme

Meshing quality determines the accuracy of the analysis. Two of the most important parameters are minimum orthogonal quality and the minimum skewness of the mesh which should be higher than 0.1 and less than 0.9, respectively [52]. Adaptive mesh was used in reference document [22] to mesh the geometry due to its capability of exhibiting proper alignment at boundaries and better element quality at local areas where high degree of geometrical complexity is observed. However, mesh settings (such as minimum element size, growth rate, etc.) were not provided in the reference document. Thus, here in our verification study, the meshing was done as aiming to obtain target values for minimum orthogonal quality (over 0.1) and maximum skewness (below 0.9). Over 12 million nodes and 7 million elements were generated where quadrilateral elements were mostly dominant. Generated mesh for the woven fabric structure and free flow domain (empty channels between the bundles are seen in Fig. 4.5 and Fig. 4.6.

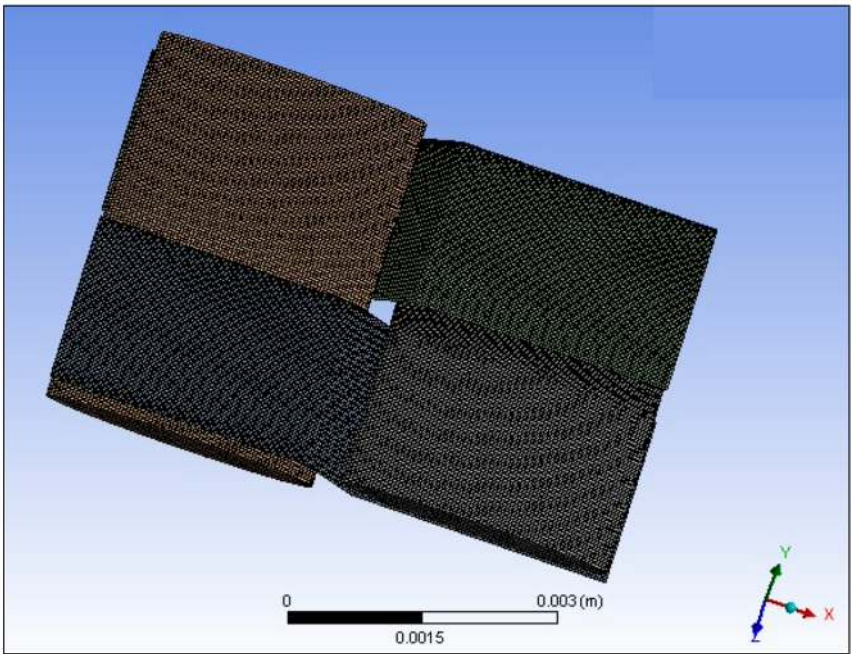

Figure 4.4 Mesh of the woven fabric structure prepared in our study (12.96×10^6 nodes and 7.23×10^6 elements)

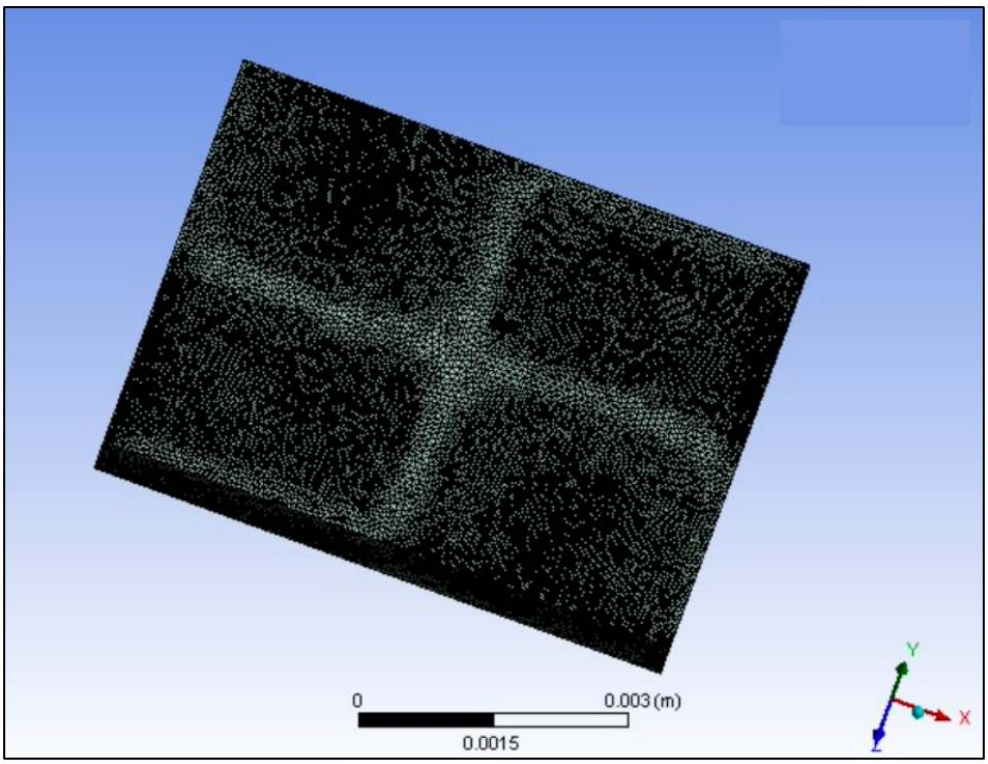

Figure 4.5 Mesh of the RVE

SIMPLE (Semi-Implicit Method for Pressure-Linked Equations) algorithm [25] was extensively used to solve Navier-Stoke' s equation using pressure correction equation. Discretization schemes were not specified in the reference document, ANSYS was used here in this study as follows: 1) second order discretization for pressure, 2) least square cell based discretization for gradient calculation, and 3) second order upwind discretization for momentum.

To solve this problem ANSYS requires viscous resistances in each direction, which can be calculated as $\frac{\mu}{\boldsymbol{K_t}}$ once the intra tow permeability (K_t) components in x, y and z direction are known. Porosity is defined as 0.44 as stated in [22] for the selected intra tow permeability. Alotaibi et al. [22] do not refer to the selected radius and unit cell dimensions to calculate the intra-tow regions using equations (4.8) and (4.9), rather $K_{t\perp}$ and $K_{t||}$ (the intra tow

permeability components perpendicular and parallel to fibers, respectively for hexagonal packing used in the original document) were specified as follows [22]:

$$K_{t||} = 6.8 \times 10^{-11}\ m^2$$
$$K_{t\perp} = 3.5 \times 10^{-11}\ m^2 \tag{4.10}$$

4.1.5 How to Model Porous Zone (Intra-Tows) in ANSYS

Before implementing a dual scale permeability model in ANSYS, it is important to know the mathematical background of the porous model of ANSYS. In this section, the derivation of the source term used in ANSYS will be reviewed.

Essentially, an empirically determined flow resistance is incorporated in a region which is defined as "porous region". It corresponds to a momentum sink (source term, S) added into the governing momentum equations [52]. When the porous model in ANSYS is used, a porous cell zone is defined in which the pressure loss in the flow is determined via inputs (such as porosity and viscous resistance).

The pressure loss across an obstruction (warps and wefts in this case) is defined as a polynomial of magnitude of velocity [53]:

$$\Delta p = C_1 U + C_2 U^2 + C_3 U^3 + \cdots \tag{4.11}$$

It is common to include only the linear and the quadratic terms and express the quadratic term as dynamic head ($\frac{1}{2}\rho U^2$) [53]:

$$\Delta p = C_1 U + C_2 \frac{1}{2}\rho U^2 \tag{4.12}$$

where Δp is the pressure loss, U is magnitude of velocity and C_1, C_2, C_3 are coefficients of the polynomial and ρ is the density of the fluid. The unit of the source term is force / volume (N/m^3).. Considering the *x* component of pressure drop:

$$\Delta p_x = C_1 U_x + C_2 \frac{1}{2}\rho |U| U_x \tag{4.13}$$

where Δp_x is pressure drop in x direction, U_x is velocity component in x direction. Force applied to the fluid by the frontal area of the porous zone in x direction is expressed as follows:

$$F_x = -\Delta p_x A = -(C_1 U_x + C_2 \frac{1}{2}\rho|U|U_x)A \tag{4.14}$$

where F_x is force applied by the frontal area of the porous zone to the fluid, A is area that the fluid encounters when it hits to the porous zone. If this equation is divided by the volume of the porous zone, the following expression is obtained:

$$S_x = \frac{F_x}{V} = -(C_1 U_x + C_2 \frac{1}{2}\rho|U|U_x)\frac{1}{t} \tag{4.15}$$

where S_x is the source term in x direction, V is the volume of the porous zone, and t is the thickness of the porous zone in the direction of the flow. This expression can also be written as:

$$S_x = -(\frac{C_1}{t}U_x + \frac{C_2}{t}\frac{1}{2}\rho|U|U_x) \tag{4.16}$$

In equation (4.16), $\frac{C_1}{t}U_x$ is the viscous loss term and $\frac{C_2}{t}\frac{1}{2}\rho|U|U_x$ is the inertial loss term. Inertial losses are neglected due to laminar, and creeping flow assumptions. Thus, equation (4.16) reduces to:

$$S_x = -(\frac{C_1}{t}U_x) \tag{4.17}$$

If this general pressure drop - velocity relationship is compared to the Darcy's Law in x direction which is given as:

$$\frac{dp}{dx} = -\frac{\mu}{K_t}U_x \tag{4.18}$$

where μ is the viscosity of the fluid, $\frac{dp}{dx}$ is the pressure gradient in x direction and K_t is the permeability of the porous zone (the permeability of the porous zone is shown as K_t here, since the porous regions in this study are the warps and wefts of the fabric and the intra tow

permeabilities of warps and weft are previously stated as K_t). The similarity between equation (4.17) and equation (4.18) can be clearly seen which leads to the following equality:

$$\frac{-\Delta p_x}{t} = \frac{C_1}{t} U_x = \frac{\mu}{K_t} U_x \tag{4.19}$$

Therefore, it can be concluded that $\frac{C_1}{t} = \frac{\mu}{K_t} = \mu \frac{1}{K_t}$. Here $\frac{1}{K_t}$ is the viscous resistance as mentioned previously and it is one of the inputs required to define a porous zone in ANSYS along with the porosity.

4.1.6 ANSYS Fluent Interface - Defining A Porous Zone

Interface of ANSYS Fluent for solution setup is shown in Fig.4.7. The steps of defining a porous zone is given as follows:

1. Click cell zone conditions.
2. Select the region where the porous zone will be defined.
3. Check porous zone box.
4. In fluid dialog box, click “porous zone”.
5. Here set viscous resistance ($\frac{1}{\boldsymbol{K_t}}$) for each direction.
6. Set inertial resistances to 0.
7. Power Law coefficients C0 and C1 are set to 0.
8. Set the porosity and click “Apply”.

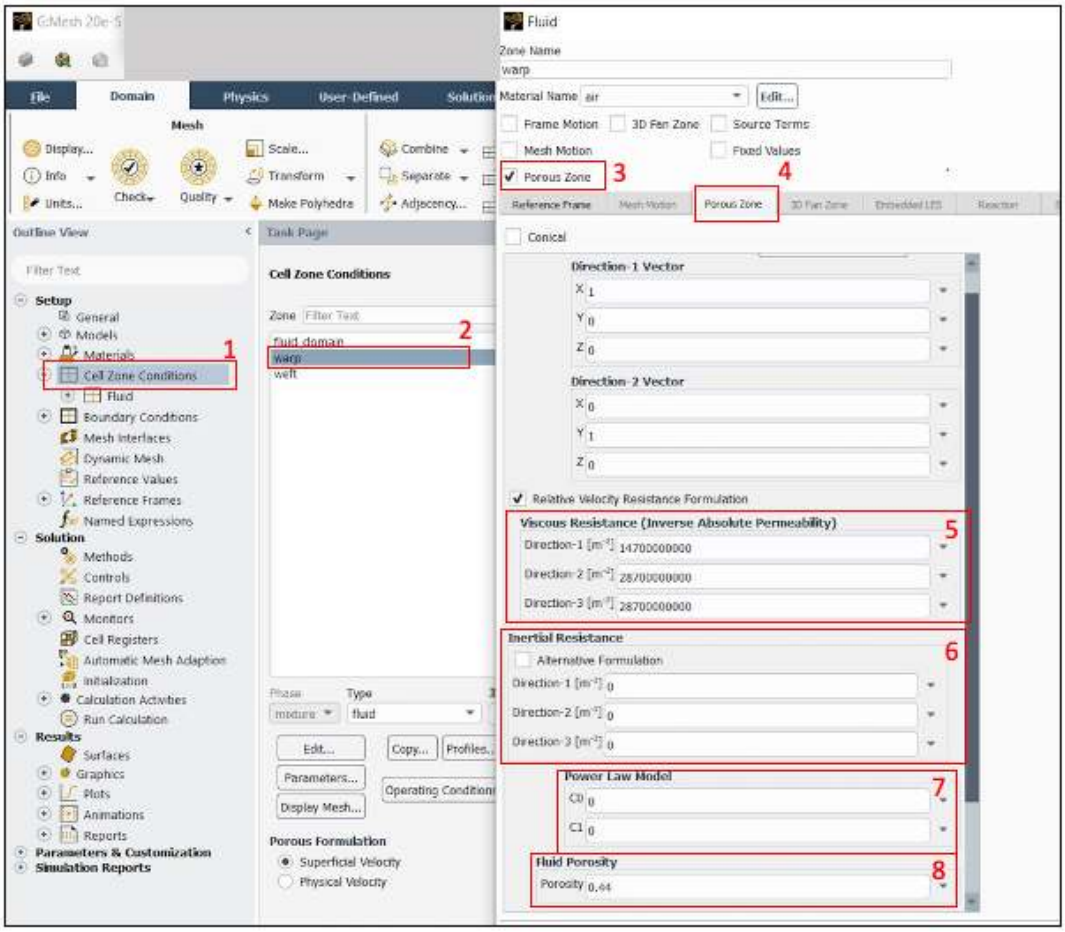

Figure 4.6 ANSYS Fluent solution setup interface: Porous model is explained step by step (red boxes indicate how to parameters are input in an order)

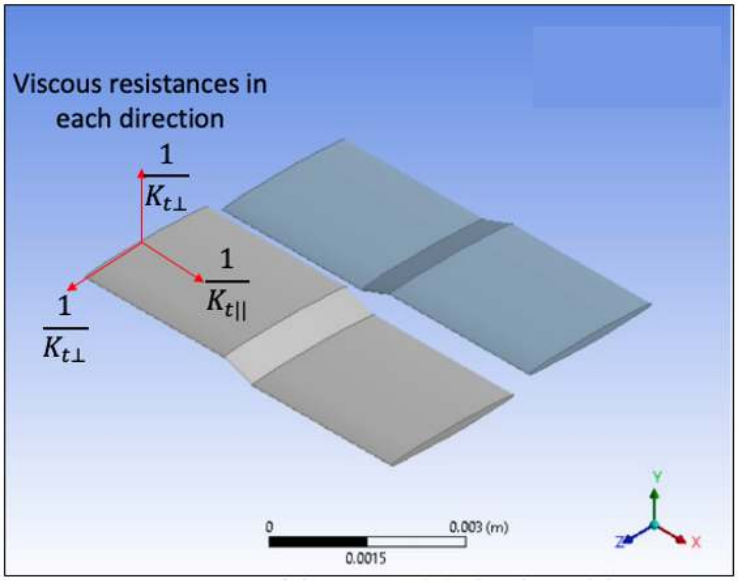

Figure 4.7 Warps of the model prepared in ANSYS; fibers are along x direction (viscous resistances defined for each direction are shown)

In the interface shown in Fig. 4.7, viscous resistances are defined using $1/K_{t\perp}$ and $1/K_{t||}$ values given in equation (4.10) assuming that the fibers are along the direction of the warps and wefts as shown in Fig. 4.8.

4.1.7 Results and Discussion

For the selected fabric and thus its geometry, the results were obtained similar to the original paper [22]. A mesh dependency study was made to ensure that the results are reliable. For the model prepared in this thesis, average inlet velocity was observed (Fig. 4.9(b)) and similar trend with the reference study (Fig. 4.9(a)) was observed as shown in Fig 4.9.

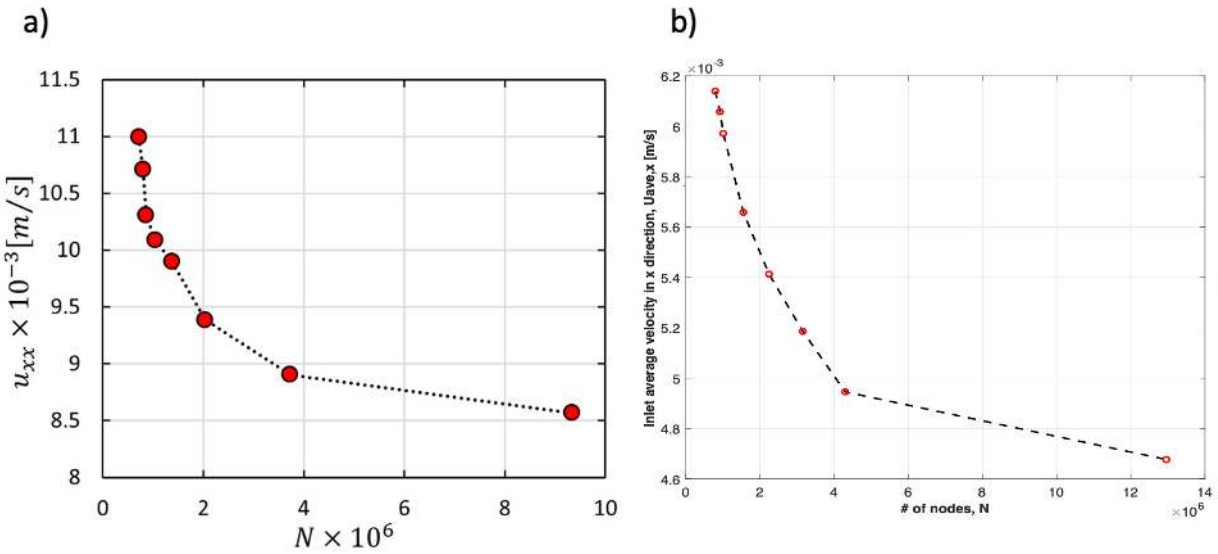

Figure 4.8 Mesh dependency study: a) the reference study [22], b) for the model prepared for this thesis

To compare our results with the results obtained in the reference study, contour plot of magnitude of velocity and pressure distribution are generated. Pressure decreases linearly along flow direction (starting from the inlet toward the exit as expected). Pressure distributions for each study can be seen in Fig. 4.10.

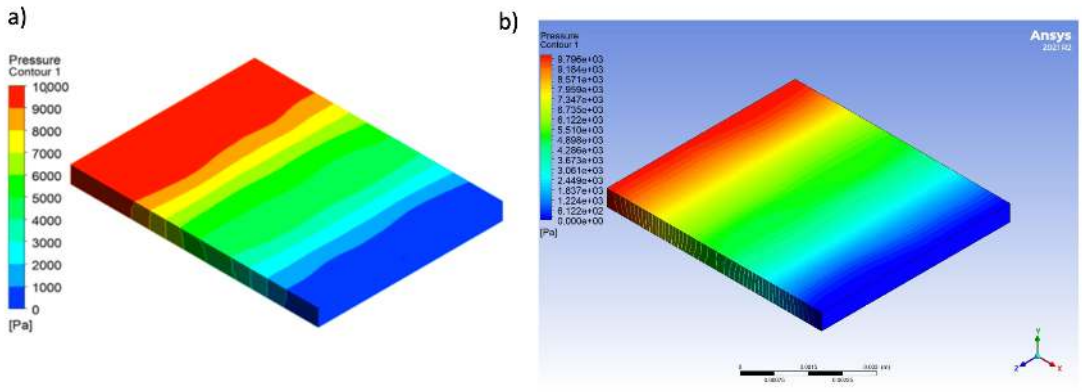

Figure 4.9 Pressure distribution of a) original study by Alotaibi et al. [22], b) our study

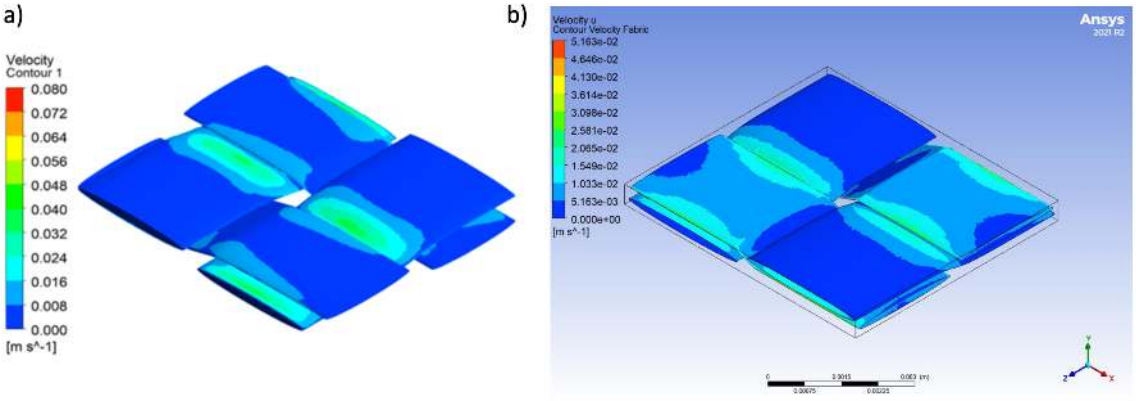

Figure 4.10 Magnitude of velocity contours from a) original paper [22], b) this study

Magnitude of velocity contours on the surfaces of permeable tows are also plotted to compare the results. Fig. 4.11(a) slightly differs from Fig. 4.11(b) due to the difference of the legend limits. However, results match significantly as detailed below.

For verification purposes, overall permeability ($K_{o,xx}$) of both models were compared. Table 4.1 shows the results obtained with: 1) our model assuming symmetry boundary condition on side walls of the rectangular domain, 2) our model assuming no-slip wall boundary condition on side walls of the rectangular domain (see Fig. 4.3), and 3) reference model previously studied by Alotaibi et al. [22] where no-slip boundary conditions assumed for the side walls of the rectangular domain. To verify our model, $K_{o,xx}$ of no-slip cases were compared (5.63×10^{-11} m^2 for our model and 5.50×10^{-11} m^2 for the reference model [22]).

It is important to note that, there were no numerical data given in the reference document regarding $K_{o,xx}$. However, the plot shown in Fig 4.12 was taken from the original document [22] which depicts the overall permeability obtained for number of intra tow porosities. Symbol x in Fig. 4.12 represents the overall permeability values obtained by Alotaibi et al. [22] for permeable tow case where the effect of local tow curvature was not included. The value of $K_{o,xx}$ (~5.50×10^{-11} m^2) was approximated from this graph. The error between two results were obtained as 2.3 %. The source of the error may be caused by: 1) there was an additional inlet zone in reference model [22] which was excluded in the model prepared for this thesis, 2) the difference in discretization schemes used which was not specified in the reference study, 3) it is stated that an adaptive mesh was used without any explanation on settings of the mesh such as element size of the mesh (where a quadrilateral dominant mesh with over 12 million nodes is used in the model prepared for this thesis). However, since the error is low and considering the uncertainties regarding the reference model solution, it can be said that our model is working properly, and boundary conditions are applied correctly. In addition, symmetry B.C. resulted in a higher permeability as expected and it can be further investigated to simulate the effect of fabric nesting.

Table 4.2 Volume flow rate Q and overall permeability of the RVE in x direction obtained by the model prepared in this study using symmetry and no-slip boundary condition separately and, overall permeability value obtained in the reference study [22], approximated from Fig. 4.12

Type of B.C. at side walls of the unit cell	Q (m^3/s)	$K_{o,xx}$ (m^2)
Symmetry B.C.	2.01×10^{-9}	6.88×10^{-11}
No-Slip B.C.	1.72×10^{-9}	5.63×10^{-11}
No-Slip BC (reference study [22])	-	$\approx 5.50 \times 10^{-11}$

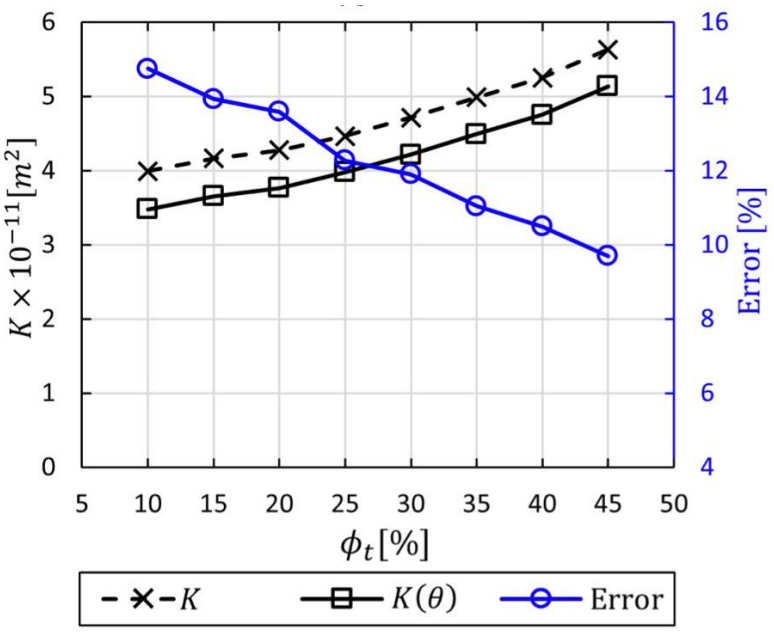

Figure 4.11 Intra-tow porosity($\emptyset_t$) vs overall permeability (referred as K) graph from [22], global permeability that will be compared with the model prepared for this thesis is indicated by black x symbols and black dashed line is the corresponding curve fit

4.2 Accounting for Non-Uniformity in a Fabric Structure

In Section 4.1, a dual scale permeability model was introduced where it was assumed that the fibers were ideally packed in a hexagonal arrangement. However, it was previously shown that the measured permeability values vary significantly, even for common fabrics [10-11, 45-46]. To account for fiber volume fraction (V_f) variation in fiber bundles, here in this thesis, we solved pressure and velocity fields by: (1) having a nominal V_f in the whole tow, and (2) having a varying V_f in tow. A porous domain (tow) was divided into subdomains and V_f was assigned either uniformly or varying in more compacted regions. Viscous resistance and porosity are defined separately for each subdomain. In this model permeabilities of subdomains were calculated by a statistically determined apparent permeability formulation which relies on a correlation between non-linearity of a fabric structure and the permeability (see Section 4.2.1).

4.2.1 Apparent Permeability

The influence of the non-uniform fiber distribution on apparent permeability of a representative volume element (RVE) was previously investigated by some researchers [47-50]. Some studies propose a correlation between the transverse apparent permeability and statistical descriptors such as average closest neighbor fiber distance (δ_1, the average of distances between each fiber and their closest neighbor fiber) or average second fiber neighbor distance (δ_2, the average of distances between each fiber and their second closest neighbor fiber) [48-50]. In most of these studies, these correlations are based on many randomly generated RVE simulations where RVEs are filled with randomly generated circular fibers. Some of these relationships can be seen in Table 4.2.

Table 4.3 Correlation between transverse apparent permeability and statistical parameters determined in different research studies [48-50]

Reference	Correlation	Notation
[48]	$K_{\perp} = K_{hex} \cdot \left(\frac{\delta_1}{\delta_{hex}}\right)^{(1.51-1.93(1-V_f))}$	$K_{\perp}$: *apparent transverse permeability* K_{hex}: *transverse permeability of hexagonally packed fibers* δ_1: *average first fiber neighbor distance* δ_{hex}: *first fiber neighbor distance in hexagonally packed fibers* V_f: *fiber volume fraction*
[50]	$K_{\perp} = 0.2 \,.\, \bar{\delta}_2^{\,2.5}(1 - 0.5e^{-3\bar{\delta}_2})d^2$	$K_{\perp}$: *apparent transverse permeability* d: *diameter of one filament* $\bar{\delta}_2$: *average second fiber neighbor distance* normalized by average fiber diameter
[49]	$K_{\perp} = 6.74\,\bar{\delta}_2 - 4.22\bar{\delta}_3 - 4.77\,\sigma\bar{\delta}_2 - 0.1\,\sigma\bar{\delta}_3 - 46.6\,V_f$	$K_{\perp}$: *apparent transverse permeability* V_f: *fiber volume fraction* $\bar{\delta}_2$: *average second fiber neighbor distance* normalized by average fiber diameter $\bar{\delta}_3$: *average third fiber neighbor distance* normalized by average fiber diameter $\sigma\bar{\delta}_2, \sigma\bar{\delta}_3$: *standard deviations of* $\sigma\bar{\delta}_2$ *and* $\sigma\bar{\delta}_3$

In the test model mentioned previously, apparent permeabilities of the subdomains, where each subdomain is filled with randomly placed fibers, were calculated in MATLAB by using the correlation presented by [48] (see Table 4.2):

$$K_{\perp} = K_{hex}\left(\frac{\delta_1}{\delta_{hex}}\right)^{(1.51-1.93(1-V_f))} \tag{4.20}$$

where δ_1 is the average first neighbor fiber distance, δ_{hex} is the first fiber distance in hexagonal packing arrangement (see Fig. 4.2(b)), K_{hex} is the permeability (perpendicular to fibers) of hexagonally packed fibers and V_f is the corresponding fiber volume fraction.

4.2.2 2D Test Model Prepared in ANSYS

To investigate how the overall permeability is affected by the local variation of fiber volume fraction within a fiber bundle (intra-tow region), a 2D test model was prepared in ANSYS as mentioned previously, where porous domain is represented as porous subdomains. The geometrical detail of the model consisting of seven subdomains is given in Fig. 4.13. For the simplicity, a rectangular domain was selected. Extra inlet and outlet regions were added to the model. Dimensions were selected considering a single layer of fiber bundle used in dual scale permeability model (warps and wefts). As shown in Fig 4.13 (b), symmetry boundary condition was assumed for the top and bottom boundaries of the domain. Injection pressure was set to 10 kPa at the inlet. A linear quadrilateral mesh with 2.48 million elements was used to discretize the domain as shown in Fig. 4.13 (c)-(d).

In order to calculate the apparent permeability values that will be assigned to each subdomain in ANSYS, an algorithm was coded in MATLAB which fills the prescribed domain with randomly placed circles (fibers) with a radius of 2 μm according to the specified fiber volume fractions which are assigned to each subdomain separately. Fiber radius of 2 μm was chosen only for the test purposes and does not represent the actual fiber dimensions. The same RVE with the same size was prepared in MATLAB as shown in Figure 4.13 (e).

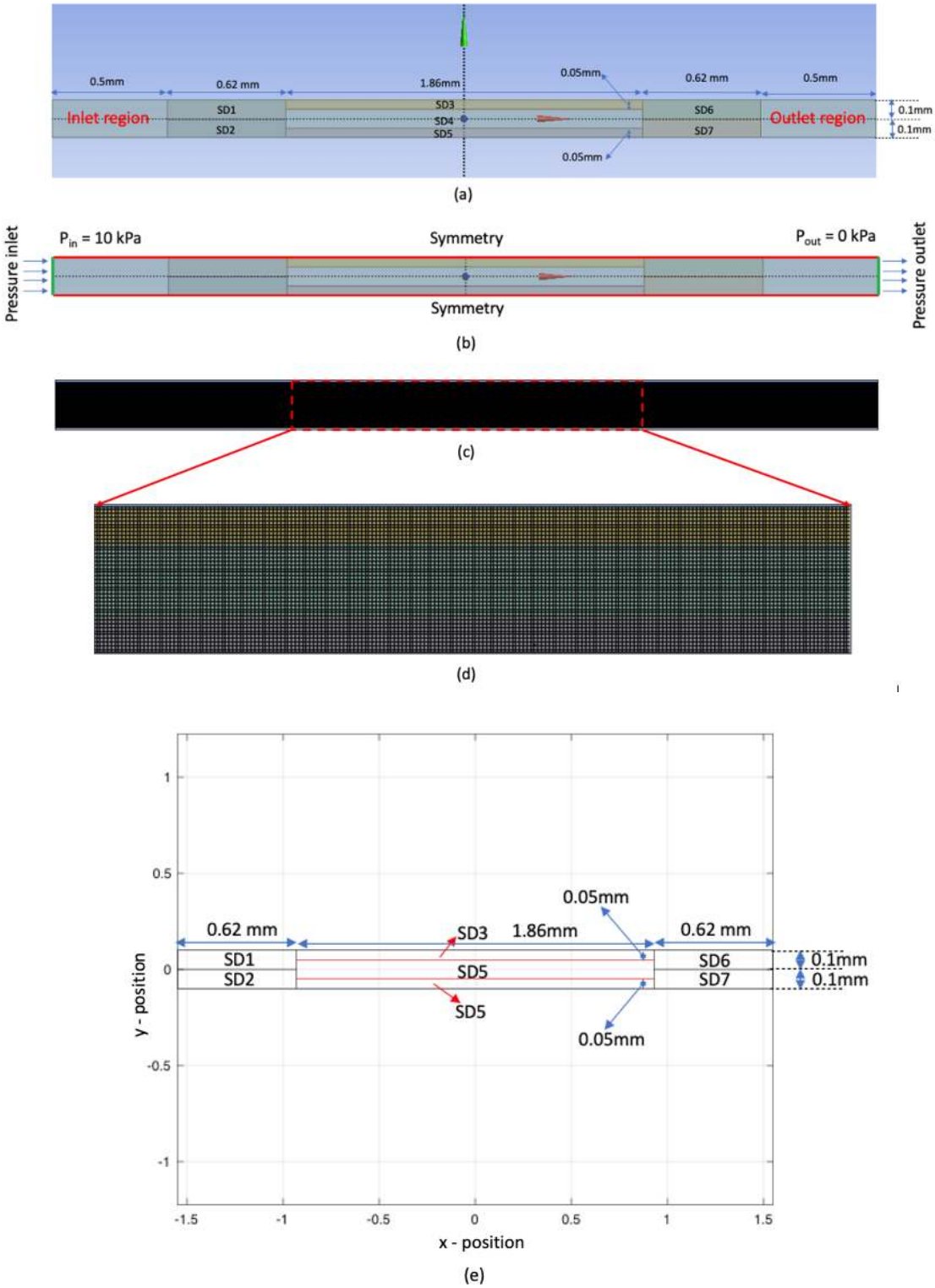

Figure 4.12 A porous rectangular domain divided into porous subdomains (SD1, SD2, SD3, SD4, SD5, SD6, SD7): (a) dimensions, (b) boundary conditions, (c) mesh of the domain (2.48 million elements, (d) zoomed view of the region shown in red square, (e) RVE to be filled with circles (fibers) in MATLAB

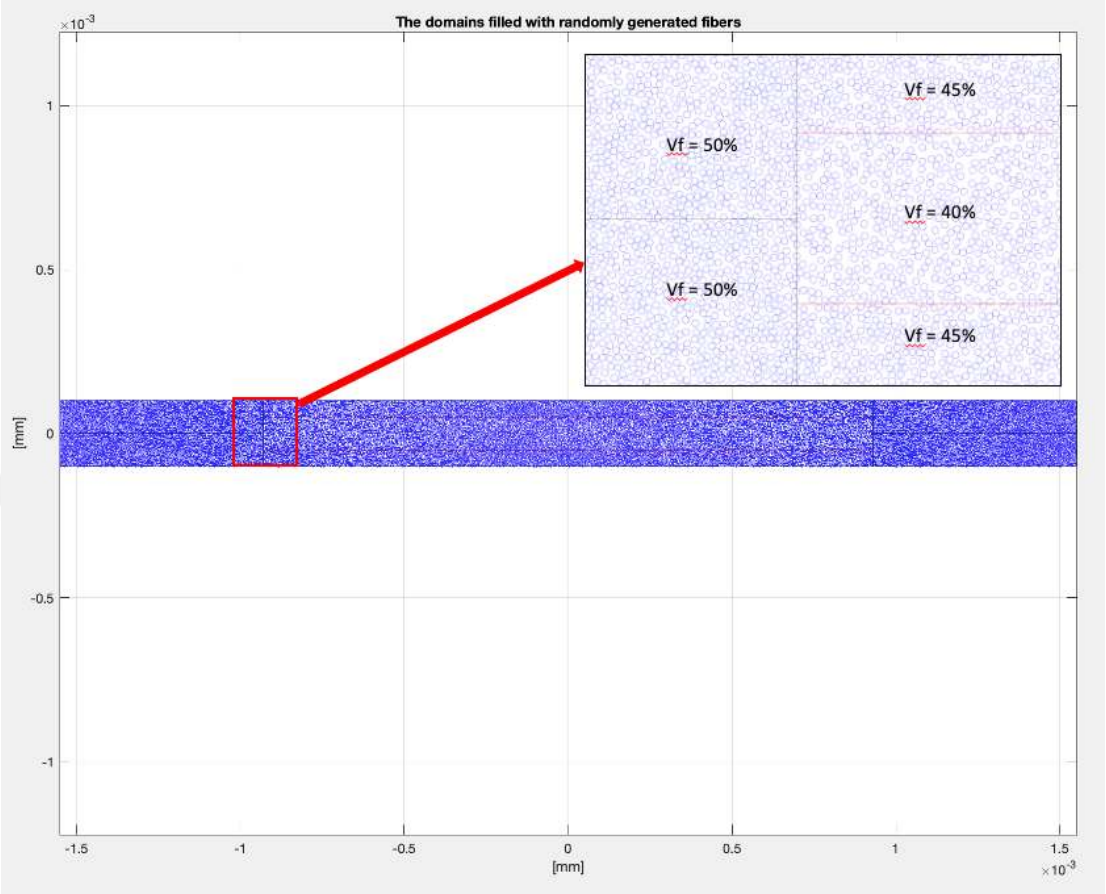

Figure 4.13 Randomly filled subdomains with corresponding V_f, region indicated with red square was zoomed to visually observe the distancing of fibers (blue circles)

In Fig. 4.14, an output visual of a single run of the MATLAB code is shown. Randomly placed fibers are indicated as blue circles. MATLAB code fills each subdomain according to the user specified V_f assigned to each subdomain. In Fig. 4.14, V_f values are assigned as 50%, 50%, 45%,40%, 45%, 50% and 50% for subdomains SD1, SD2, SD3, SD4, SD5, SD6 and SD7, respectively. Note that, these V_f values are not representing a real distribution and only assigned to test the model. A red squared region was zoomed to visually observe the distancing of randomly generated fibers of subdomains with different V_f values.

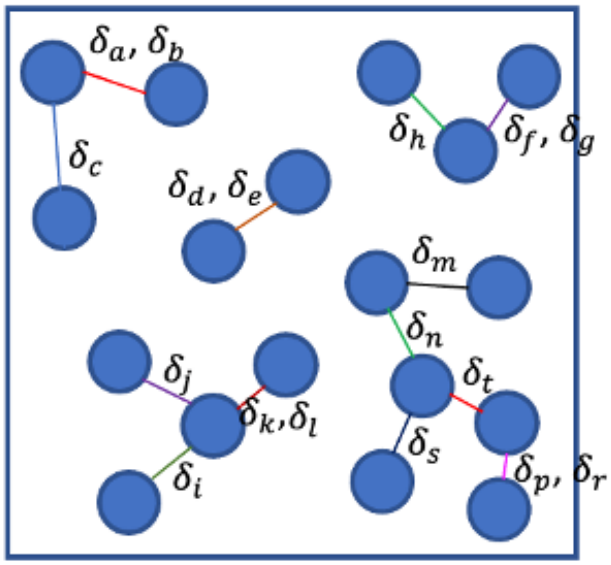

Figure 4.14 Illustration of an RVE. Fibers are indicated as blue circles and average first neighbor fiber distances is indicated as colored lines

In order to calculate the apparent permeability of each sub domain, equation (5.1) was used where mean first neighbor fiber distance δ_1 is needed. Note that equation (5.1) prepared for the example RVE is shown in Fig. 4.15. Essentially, δ_1 is the average of the distance between a fiber and its closest neighbor. As an example, Figure 4.15 illustrates an example of a RVE filled with number of fibers where first neighbor fiber distance of each fiber is shown as δ_a, δ_b, δ_c, ... , δ_t (this example RVE consists of 18 fibers). Thus $\delta_1$is calculated as:

$$\delta_1 = \frac{\delta_a + \delta_b + \delta_c + \delta_d + \delta_e + \delta_f + \delta_g + \delta_h + \delta_i + \delta_j + \delta_k + \delta_l + \delta_m + \delta_n + \delta_p + \delta_r + \delta_s + \delta_t}{N} \quad (4.21)$$

where N is the number of fibers, 18 in this example. The calculation of the average first neighbor fiber distance is implemented to the code such that the code first generates the prescribed domain (subdomains), secondly fills them with randomly generated fibers according to the specified V_f values and lastly calculates the apparent permeability of each subdomain, as well as the overall permeability of the whole domain. It is worth noting that

the overall fiber volume fraction and overall apparent permeability of the domain were not calculated by averaging the V_f and permeabilities of each subdomain. Since the location of each fiber of the domain is known, the average first neighbor fiber distance was calculated by using all of the fibers in the domain (includes all of the subdomains). Similarly, since the number of fibers in each subdomain is known, V_f is calculated by dividing the sum of the area of the fibers to the sum of the cross-sectional areas of the subdomains.

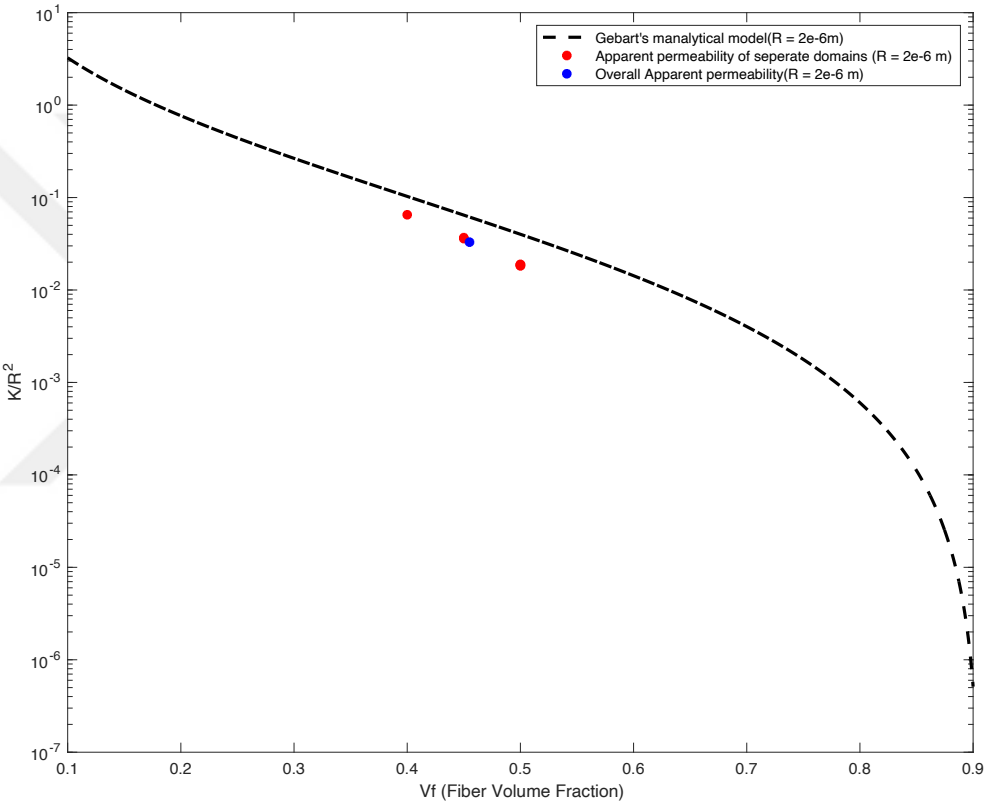

Figure 4.15 Apparent permeability normalized by fiber radius (where R = 2 E-6 m) vs. fiber volume fraction (V_f). Dashed line indicates Gebart's formulation for hexagonal arrangement (see eq. (4.8))

A comparative study was made to observe the variability in apparent permeability between random runs. Fiber radius was kept the same, 2μm. V_f of each sub domain was kept the same (50%, 50%, 45%,40%, 45%, 50% and 50% for subdomains SD1, SD2, SD3, SD4, SD5, SD6 and SD7, respectively). Appendix 1 shows the apparent permeability of each subdomain as well as the overall apparent permeability for each random run and the corresponding mean and standard deviations. Since the orientation of fibers change in each random generation, the average first neighbor fiber distance also change which alters the

apparent permeability values slightly. However, no significant variation was observed. In Appendix 2, apparent permeability of each subdomain for different random runs can be seen. Normalized apparent permeabilities of the subdomains and the overall normalized permeability calculated for a single random run are slightly lower than the ideally packed fibers for the same V_f as shown in Fig. 4.16. The similar trend was observed for repeated runs. This issue was previously stated in [48] and thus the results were as expected.

Using aforementioned tools, two case studies were conducted to investigate: 1) the performance of ANSYS when modelling the transitions between porous subdomain, 2) the effect of local fiber volume fraction variation on the overall permeability of the porous domain.

4.2.3 Case Studies

Random fiber placement was done by a code prepared in MATLAB for specified V_f. Apparent permeabilities calculated for each subdomain for given V_f values are shown in as well as the overall permeability and V_f of the domain (these are calculated by the method explained in Section 4.2.2) are given in Table 4.3.

Table 4.4 Specified V_f and corresponding apparent permeability for each subdomain and overall porous domain. Values used as an ANSYS input: (1) for 1st case study and (2) for 2nd case study

Subdomain	Specified Fiber Volume Fraction, V_f	Apparent permeability, K [m²]	
SD1	50%	7.70×10^{-14}	
SD2	50%	7.43×10^{-14}	
SD3	45%	1.50×10^{-13}	
SD4	40%	2.62×10^{-13}	(2)
SD5	45%	1.45×10^{-13}	
SD6	50%	7.33×10^{-14}	
SD7	50%	7.34×10^{-14}	
Porous Domain	45.5%	1.32×10^{-13}	(1)

Viscosity and density are defined as 0.15 Pa.s and 1300 kg/m^3 as it was done in the dual scale model. To calculate the viscous resistance ($\frac{1}{K}$) and porosity, which will be provided to ANSYS as an input, overall values are used (Table 4.3 (1), highlighted values) for the 1st case study.

In the 1st case study, the aim was to show that ANSYS can successfully model the transition interfaces between each sub domain. To demonstrate the performance of the ANSYS model, overall porosity (1-$V_{f,overall}$) and overall viscous resistance ($\frac{1}{K\ overall}$) values were assigned to all of the subdomains (Table 4.3 (1), the same values were assigned to each of the subdomains). The model is solved by SIMPLE solver using default discretization schemes of ANSYS as previously done in Section 4.1.4. The volume flow rate at the inlet was calculated by taking the surface integral of the velocity profile at the inlet region. The permeability of the overall domain in *x* direction ($K_{o,xx}$), is computed by using Darcy's Law, equation (4.7). The expected $K_{o,xx}$ was 1.32 x 10^{-13} m^2, which was used to define the viscous resistances to be used as an ANSYS input and the result was obtained as 1.32 x 10^{-13} m^2. If any deviation from this value would have been observed, then the reliability of our analysis through the ANSYS model would be questionable. However, n almost perfect match was achieved, thus, this case study was concluded as our analysis through ANSYS is capable of modelling transition interfaces between porous zones and a model that accounts for fabric volume fraction variation can be studied later in this thesis.

2nd case study included to investigate the effect of local variation in fiber volume fraction on overall permeability of the porous region. For this case, apparent permeability values and V_f values corresponding to each subdomain indicated in Table 4.3 (1) are used as the model inputs. Viscous resistances are calculated by using apparent permeability values corresponding to each subdomain and given as an input to ANSYS when defining each porous subdomains. Injection pressure, viscosity, and density. Similar to 1st case study, SIMPLE solver was used with default discretization scheme settings. The results of both case studies are shown in Table 4.4.

4.2.4 Discussion

Essentially the aim of these case studies is to determine any variation in the resulting overall permeability between 1) a model where V_f and $K_{o,xx}$ are uniformly distributed in the porous domain (1st case study) and a model where V_f and $K_{o,xx}$ vary between the subdomains of the porous domain (2nd case study). Note that in the 2nd case study the overall V_f of the porous domain is the same as the 1st case study (45.5%), but it locally varies between 7 porous subdomains. As shown in Table 4.4, $K_{o,xx}$ was lower in 2nd case study compared to the 1st case study with a deviation of around 10% (1.20×10^{-13} m^2 and 1.32×10^{-13} m^2, respectively). By looking at this outcome, it can be clearly said that for the same overall fiber volume fraction, the local variation in V_f within a porous structure affects the overall permeability of the structure, as expected, however not very significantly. Moreover, such a model can be developed in ANSYS that accounts for non-uniformity of fiber distribution and fiber volume fraction by locally mapping the domain with different V_f and permeability values.

Table 4.5 Comparison of 1st case study and 2nd case study

	Subdomain	Specified Fiber Volume Fraction, V_f	INPUT: Apparent permeability, K [m^2]	OUTPUT: Volume flow rate, Q [m^3/s]	Overall permeability, $K_{o,xx}$ [m^2]
2nd case study	SD1	50%	7.70×10^{-14}	5.17×10^{-10}	1.20×10^{-13}
	SD2	50%	7.43×10^{-14}		
	SD3	45%	1.50×10^{-13}		
	SD4	40%	2.62×10^{-13}		
	SD5	45%	1.45×10^{-13}		
	SD6	50%	7.33×10^{-14}		
	SD7	50%	7.34×10^{-14}		
1st case study	Porous Domain	45.5%	1.32×10^{-13}	5.69×10^{-10}	1.32×10^{-13}

4.3 Extended Dual Scale Model

After validating the suitability of ANSYS modelling for flow through porous domains with a variation of a fiber volume fraction, here in this section a similar case study was investigated using a 3D dual scale model. It was previously shown that fiber volume fraction is higher at the cross-over regions (where warps and wefts are overlapped) of a woven fabric [54]. Fig. 4.17 was adapted from a study [54] which depicts the variation of fiber volume fraction in a single tow of a woven fabric. It shows that the fiber volume fraction is higher (over 64%) at the cross-over regions compared to the remaining regions of the same tow (approximately 60%). The research made in [54] was taken as a reference study to account for the local variation of the fiber volume fraction in a 3D dual scale model. The aim of this section was to compute the global permeability of a dual scale model by solving pressure and velocity fields by: (1) having uniform V_f of tows, and (2) having varying V_f within the tows. It is important to note that the average V_f in case (2) was kept the same as the one used in case (1) for the convenience.

In this study, apparent permeability is calculated only for $K_{\perp}$ (perpendicular to fibers) as it was done in Section 4.2, but by randomly placing fibers into elliptical cross sections of warps and wefts for the given fiber volume fractions. $K_{||}$ will be calculated by Gebart's analytical formulation (see equation (2.9)). These permeability values will be used as an ANSYS inputs to define porous subdomains.

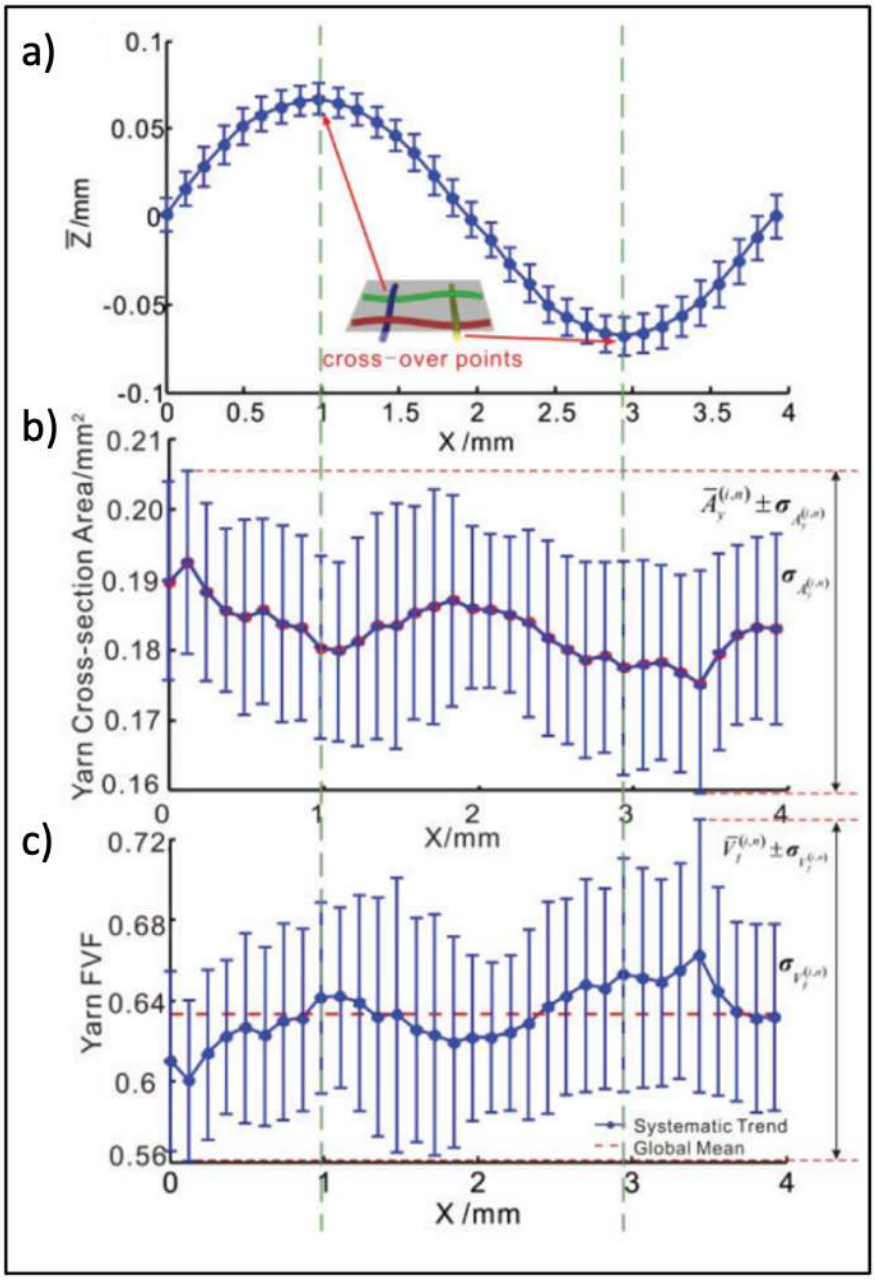

Figure 4.16 For the woven fabric studied here, stochastic deviation in a) waviness (location) of a tow (yarn), b) cross-sectional area of a tow, c) fiber volume fraction (FVF) of a tow [54]:

Fiber volume fraction can reach above 64% locally within the bundles at near cross over regions and alters through the bundles. The reason for that is the nesting effect of bundles of woven fabric.

4.3.1 Modelling approach

The same flow model through dual scale porosity used in section 4.1 was taken as a reference model, however this time, tows (warps and wefts) were divided into subdomains as shown in Fig. 4.18. Essentially fiber volume fraction varies through the bundles at different locations where maximum V_f is observed near the cross-over regions. However, for the simplicity, one third of each cross over region was assumed as "high-V_f regions" and remaining regions were assumed as "low-V_f regions" (see Fig. 4.18). In this study, overall fiber volume fraction of tows was kept the same (56.0%). For the varying V_f case, 64.0% was assigned to "high-V_f regions" and fiber volume fraction of the "low-V_f regions" were calculated as 52.5% for warps and 52.6% for wefts since the dimensions of warp and wefts slightly differ from each other. Fiber radius was assumed as 20 μm.

Density and viscosity of a liquid resin was selected as 1300 kg/m^3 and 0.15 Pa.s, respectively as it was done in section 4.1. No-slip boundary condition was assumed for the side walls of the RVE. Inlet pressure was set to 10 kPa. Quadrilateral dominant mesh with 12.4 million nodes and 7.8 million elements was used to discretize the domain (minimum orthogonal quality of 0.14 and maximum skewness of 0.85). Permeability of each subdomain was assigned as shown in Table 4.5.

To numerically observe the effect of the local variation in fiber volume fraction, 3 cases were assumed as follows: 1) V_f of 56% was assigned to all subdomains where permeability of each subdomain was calculated using Gebart's analytical formulation for hexagonally packed fibers, 2) V_f of 56% was assigned to all subdomains where $K_\perp$was calculated using apparent permeability correlation and $K_{||}$ was calculated using Gebart's analytical formulation for hexagonally packed fibers, and 3) varying V_f was assumed and assigned to each subdomain separately, and accordingly $K_\perp$was calculated using apparent permeability correlation and $K_{||}$ was calculated using Gebart's analytical formulation for hexagonally packed fibers. The distribution of fiber volume fraction for each case is seen in Fig. 4.19.

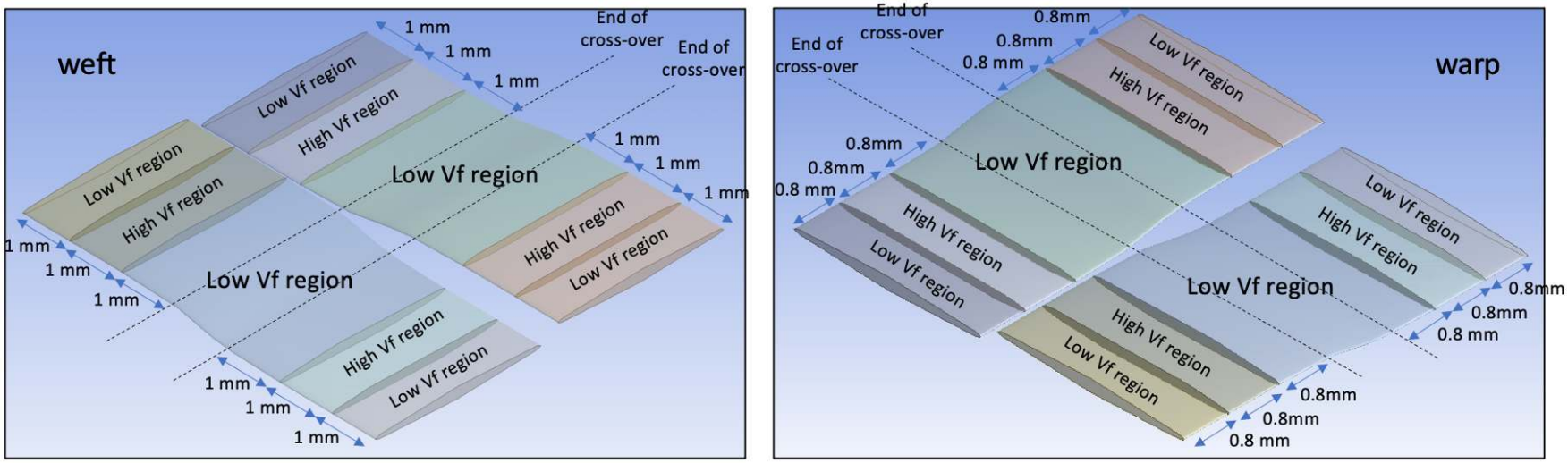

Figure 4.17 Tows of the dual scale model: a) subdomains of the warps with corresponding dimensions, b) subdomains of the warps with corresponding dimensions

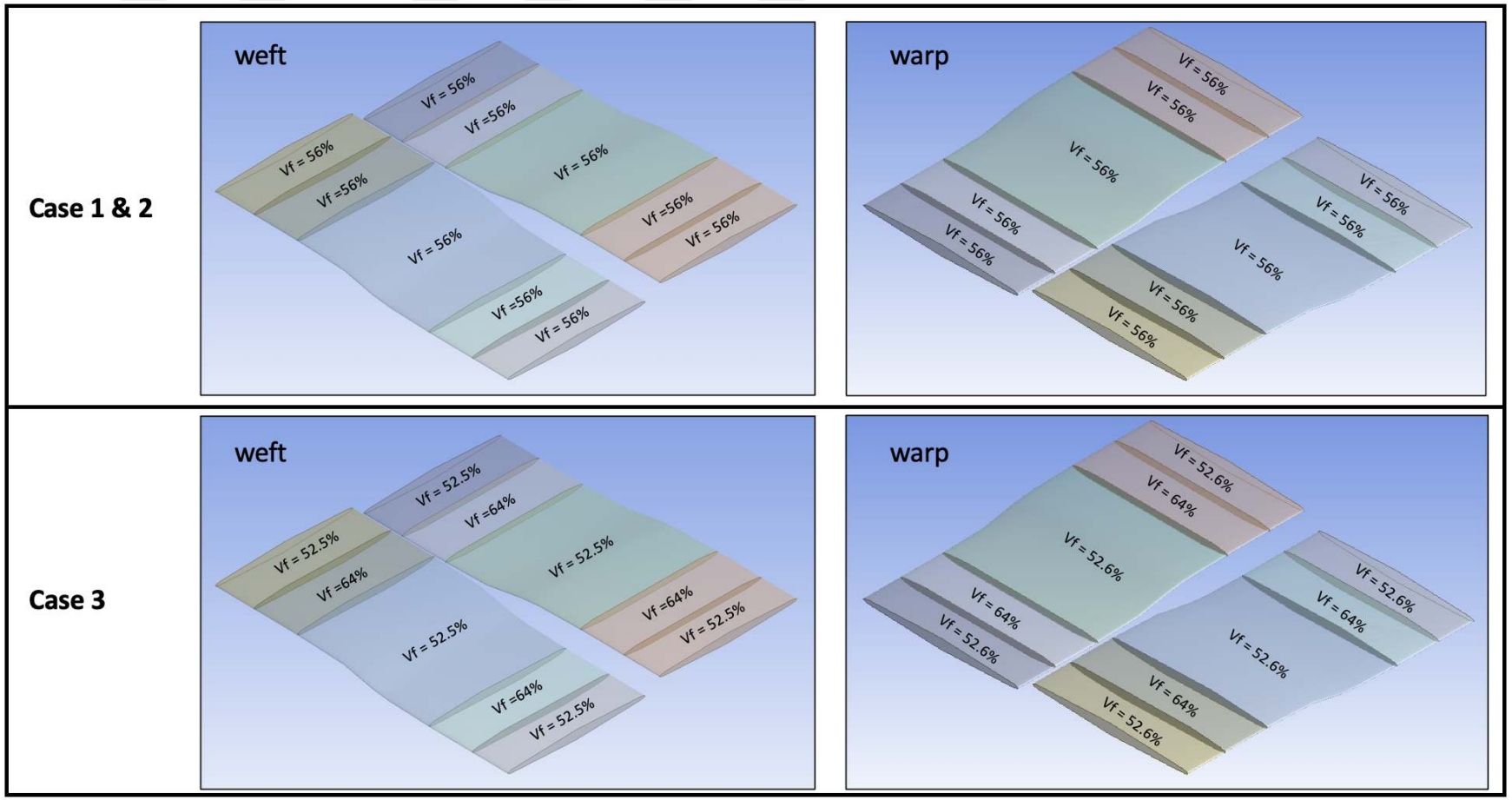

Figure 4.18 Distribution of fiber volume fraction over the subdomains of wefts and warps for each case

4.3.2 Results and Discussion

Table 4.5 shows the permeability values used to define porous domains in ANSYS, as well as the overall permeability values calculated for each case. The overall permeability for Case 1 was higher than Case 2 and Case 3 as expected since the ideally packed fibers result in higher permeability than non-uniformly distributed fibers as previously shown in Section 4.2 (see Fig. 4.16). Overall permeability obtained for Case 2 and Case 3 slightly differs with a difference of 0.1%. This indicates that even though the local variation in fiber volume fraction within the fiber bundle affects the overall permeability, the effect is small. When Case 1 and Case 3 are considered, the difference in overall permeability is larger compared to the difference between Case 2 and Case 3, with a difference of 0.4% which was expected due to the higher overall permeability of ideally packed fibers.

Table 4.6 Permeability values used in ANSYS model for uniform V_f and varying V_f cases

	Case 1 (Uniform V_f)	Case 2 (Uniform V_f)	Case 3 (Varying V_f)			
	Gebart's $K_\perp$	Apparent $K_\perp$	Warp		Weft	
Fiber volume fraction, V_f	**56%**	**56%**	**64% (High V_f)**	**52.6% (Low V_f)**	**64% (High V_f)**	**52.5% (Low V_f)**
$K_\perp$ [m²]	3.53×10^{-12}	1.84×10^{-12}	7.09×10^{-13}	2.93×10^{-12}	5.67×10^{-13}	2.91×10^{-12}
$K_{\|\|}$ [m²]	1.61×10^{-11}	1.61×10^{-11}	6.88×10^{-12}	2.32×10^{-11}	6.88×10^{-12}	2.35×10^{-11}
$K_{overall}$[m²]	4.422×10^{-11}	4.398×10^{-11}	4.403×10^{-11}			

With the model assumptions used in this approach (maximum fiber volume fraction of bundles at one third of each cross over region, use of apparent permeability correlation when calculating intra-tow permeability component, $\boldsymbol{K}_\perp$, and use of Gebart's analytical formulation for hexagonally packed fibers when calculating the permeability component $\boldsymbol{K}_{||}$), the effect of the variation in fiber volume fraction is small with a difference of up to 0.4%. This difference indirectly shows the dominance of empty flow channels between the bundles over porous bundles on the overall permeability. It is important to note that, in this approach the change in fiber volume fraction was adjusted by the number of fibers within the bundles. However, in a real-life case, the change in V_f is induced by the deformation of a bundle (in other words by the change of cross-sectional area of a bundle). In addition, apparent permeability correlations were used to calculate $K_\perp$ only, and $K_{||}$ was calculated

using Gebart's analytical formulation for hexagonally packed fibers. Eventually this approach assumes different fiber distribution within the bundles for $K_{\perp}$ and $K_{||}$.

As a result, this study shows that the porous subdomains which has different fiber volume fractions and permeabilities can be successfully modelled in ANSYS. Local variation of fiber volume fraction can be numerically observed and simulated in a commercial software. Non-linearity of the fiber distribution in bundles of a fabric structure, can be accounted in a dual scale model when determining intra-tow permeability.

It is important to note that, the result of the numerical analysis made in thesis is not validated by experiments. However, the results indicates that the non-uniformity in fiber volume fraction of bundles has a small effect on the overall permeability of a fabric structure. The effect of bundle deformation was not studied here, however it can be modelled in ANSYS.

4.3.3 Future Recommendations

Dual scale modelling approach presented in this thesis has a potential to be a more realistic permeability model in which non-uniformity is accounted. Still, the success of such a model must be validated by experiments. For a more realistic model, X-Ray image of a compressed fabric structure can be taken to extract the geometrical details of the compressed tows as well as the distribution of the fibers in a bundle).

Similar to this study, bundles of the fabric structure can be divided into subdomains and apparent permeabilities can be calculated for each subdomain (this would require an image processing to detect locations of fibers). The porous domains in ANSYS can be defined using calculated apparent permeabilities and also permeability of the fabric structure can be experimentally measured and compared with permeability calculated by ANSYS model. This modelling approach can be tested for various fabric structures (for example non-crimp, biaxial etc.), stacking and nesting of fabric layers.

A numerical analysis for $K_{||}$ (for the flow parallel to the fibers) can be studied to establish a correlation formulation (similar to $K_{\perp}$) and used as a model parameter to define porous domains in ANSYS. By this way, the orientation of fibers can be properly modeled in 3D.

References

[1] S. G. Advani, and E. M. Sozer, “Process Modeling in Composites Manufacturing,” p. 436, 2002.

[2] P. Ermanni, C.D. Fratta, and F. Trochu, "Molding: liquid composite molding (LCM)," Wiley Encyclopedia of Composites, pp. 1-10, 2012

[3] M. A. Yalcinkaya, and E. M. Sozer, Effect of part thickness variation on the mold filling time in vacuum infusion process," J. Reinf. Plast. Compos., vol. 33, no. 23, pp. 2136– 2150, 2014.

[4] L. Baichen, S. Bickerton, and Suresh G. Advani, "Modelling and simulation of resin transfer molding (RTM)—gate control, venting and dry spot prediction," Composites Part A: Applied Science and Manufacturing, vol. 27, no. 2, pp. 135-141, 1996

[5] S. Akbar, S. R. Ghaffarian, and S. M. H. Karimian, "Modeling and simulation approaches in the resin transfer molding process: a review," Polymer Composites, vol. 24, no. 4, pp. 525-544, 2003

[6] B. R. Gebart, and P. Lidström, "Measurement of in-plane permeability of anisotropic fiber reinforcements," Polymer composites vol. 17, no.1, pp. 43-51, 1996

[7] J.R. Weitzenböck, R. A. Shenoi, and P. A. Wilson, "Radial flow permeability measurement. Part A: Theory," Composites Part A: Applied Science and Manufacturing, vol.30, no. 6, pp. 781-796, 1999

[8] R. Gauvin, F. Trochu, Y. Lemenn, and L. Diallo, "Permeability measurement and flow simulation through fiber reinforcement," Polymer Composites, vol. 17, no.1, pp. 34-42, 1996

[9] M. A. Yalcinkaya, A. Sarioglu, and E. M. Sozer, “A novel mold design for one-continuous permeability measurement of fiber preforms,” J. Reinf. Plast. Compos., vol. 34, no. 11, pp. 915–930, 2015.

[10] R. Arbter, et al. “Experimental determination of the permeability of textiles: A benchmark exercise,” Compos. Part A Appl. Sci. Manuf., vol. 42, no. 9, pp. 1157–1168, 2011.

[11] N. 1, et al. “Experimental determination of the permeability of engineering textiles: Benchmark II,” Compos. Part A Appl. Sci. Manuf., vol. 61, pp. 172–184, 2014.

[12] C. C. Wong, et al. "Comparisons of novel and efficient approaches for permeability prediction based on the fabric architecture," Composites Part A: Applied Science and Manufacturing, vol. 37, no. 6, pp. 847-857, 2006

[13] P. Šimáček, and S. G. Advani, "Permeability model for a woven fabric," Polymer Composites, vol. 17, no. 6, pp. 887-899, 1996

[14] R. Dave, J. L. Kardos, and M. P. Duduković, "A model for resin flow during composite processing part 2: Numerical analysis for unidirectional graphite/epoxy laminates," Polymer Composites, vol.8, no. 2, pp. 123-132, 1987

[15] M. V. Bruschke, and S. G. Advani, "Flow of generalized Newtonian fluids across a periodic array of cylinders," Journal of Rheology, vol. 37, no. 3, pp. 479-498, 1993

[16] B. R. Gebart, "Permeability of unidirectional reinforcements for RTM," Journal of Composite Materials, vol. 26, no. 8, pp. 1100-1133, 1993

[17] Spaid, Michael AA, and Frederick R. Phelan Jr., "Lattice Boltzmann methods for modeling microscale flow in fibrous porous media," Physics of Fluids, vol. 9, no. 9, pp. 2468-2474, 1997

[18] S. Bickerton, Q. Govignon, and P. Kelly, "Resin infusion/liquid composite moulding (LCM) of advanced fibre-reinforced polymer (FRP)," Advanced Fibre-Reinforced Polymer (FRP) Composites for Structural Applications. Woodhead Publishing, pp. 155-186, 2013

[19] Y. Minyoung, et al. "Stochastic modeling of through the thickness permeability variation in a fabric and its effect on void formation during Vacuum Assisted Resin Transfer Molding," Composites Science and Technology, vol. 149, pp. 100-107, 2017

[20] M. A. Ali, et al. "Non-destructive evaluation of through-thickness permeability in 3D woven fabrics for composite fan blade applications," Aerospace Science and Technology, vol. 82, pp. 520-533, 2018

[21] D. Merhi, V. Michaud, L. Kaïmpfer, P. Vuilliomenet, and J. A. E. Mañnson, "Transverse permeability of chopped fibre bundle beds," *Compos. Part A Appl. Sci. Manuf.*, vol. 38, no. 3, pp. 739–746, 2007.

[22] H. Alotaibi, M. Jabbari, and C. Soutis, "A numerical analysis of resin flow in woven fabrics: effect of local tow curvature on dual-scale permeability" Materials, vol. 14, no. 2, pp. 405, 2021

[23] N. Kuentzer, et al. "Permeability characterization of dual scale fibrous porous media," Composites Part A: Applied Science and Manufacturing, vol. 37, no. 11, pp. 2057-2068, 2006

[24] A. Nabovati, E. W. Llewellin, and A. C. M. Sousa, "Through-thickness permeability prediction of three-dimensional multifilament woven fabrics," Composites Part A: Applied Science and Manufacturing, vol. 41, no. 4, pp. 453-463, 2010

[25] J. P. Van Doormaal, G. D. Raithby, "Enhancements of the SIMPLE method for predicting incompressible fluid flows," Numerical Heat Transfer, vol. 7, no. 2, pp. 147-163, 1984

[26] H. Caglar, "Permeability characterization of fiber reinforcements used in liquid composite molding," MSc. Thesis, Koc University, July 2018.

[27] B. Yenilmez, and E. M. Sozer, "Compaction of e-glass fabric preforms in the Vacuum Infusion Process, A: Characterization experiments," Composites Part A: Applied Science and Manufacturing, vol. 40, no. 4, pp. 499-510, 2009

[28] M. A. Yalcinkaya, and E. M. Sozer, "Effect of part thickness variation on the mold filling time in vacuum infusion process," Journal of Reinforced Plastics and Composites, vol. 33, no. 23, pp. 2136-2150, 2014

[29] B. Caglar, B. Yenilmez, and E. M. Sozer, "Modeling of post-filling stage in vacuum infusion using compaction characterization," Journal of Composite Materials, vol.49, no. 16, pp. 1947-1960, 2015

[30] B. Yenilmez, et al., "Minimizing thickness variation in the vacuum infusion (VI) process," Advanced Composites Letters, vol. 20, no. 6, 2011

[31] N. C. Correia, et al., "Use of resin transfer molding simulation to predict flow, saturation, and compaction in the VARTM process," Journal of Fluids Eng., vol. 126, no. 2, pp. 210-215, 2004

[32] Q. Govignon, et al., "Full field monitoring of the resin flow and laminate properties during the resin infusion process," Composites Part A: Applied Science and Manufacturing, vol. 39, no. 9, pp. 1412-1426, 2008

[33] H. M. Andersson, et al., "Application of digital speckle photography to measure thickness variations in the vacuum infusion process," Polymer Composites, vol. 24, no. 3 pp. 448-455, 2003

[34] J. Molimard, and L. Navarro., "Uncertainty on fringe projection technique: A Monte-Carlo-based approach," Optics and Lasers in Engineering, vol. 51, no. 7, pp. 840-847, 2013

[35] M. Lemmens, "A survey on stereo matching techniques," Int. Arch Program Remote Sens., vol. 27, pp.11-23, 1988

[36] Baris Caglar, "Experimental and numerical investigation of material characterization and flow monitoring in liquid composite molding processes," PhD. Thesis, Koc University, March 2017.

[37] D. Beach, C. Milroy, M. Kohn, and D. Somen, "David SLS-2 Tutorial," Stanford Prod. Realis. Lab, pp. 1–17, 2015, Available: http://www.david-3d.com/en/products/sls-2.

[38] F. Robitaille, R. Gauvin, "Compaction of textile reinforcements for composites manufacturing: I-review of experimental results," Polymer Compos., vol.19, no. 2, pp. 198–216, 1998

[39] F. Robitaille, R. Gauvin, "Compaction of textile reinforcements for composites manufacturing. II: compaction and relaxation of dry and H2O saturated woven reinforcements," Polym. Compos., vol. 19, no. 5, pp. 543–57, 1998

[40] M. A. Yalcinkaya, B. Caglar, and E. M. Sozer, “Effect of permeability characterization at different boundary and flow conditions on vacuum infusion process modeling,” J. Reinf. Plast. Compos., vol. 36, no. 7, pp. 491–504, 2017

[41] Nazlı Koroglu, “Monitoring and modeling part thickness in vacuum assisted resin transfer molding,” MSc. Thesis, Koc University, September 22

[42] HP 3D Structured Light Scanner. (n.d.). Retrieved from hp Web site: https://www8.hp.com/us/en/campaign/3Dscanner/overview.html

[43] V. Yavari, and M. H. Kadivar, "Fiber Volume Fraction around Stitch in NCF **Composit**es," Procedia Engineering, vol. 14, pp. 3191-3198, 2011

[44] J. R. Weitzenböck, R. A. Shenoi, and P. A. Wilson, “Radial flow permeability measurement. Part A: theory,” Compos. Part A Appl. Sci. Manuf., vol. 30, no. 6, pp. 781–796, 1999

[45] D. May, A. Aktas, S. Advani, D. Berg, A. Endruweit, E. Fauster, et al., "In-plane permeability characterization of engineering textiles based on radial flow experiments: A benchmark exercise," Composites Part A: Applied Science and Manufacturing vol. 121, pp. 100 – 114, 2019

[46] A. Yong, A. Aktas, D. May, A. Endruweit, S. Advani, P. Hubert, et al.," Out-of-plane permeability measurement for reinforcement textiles: A benchmark exercise," Composites Part A: Applied Science and Manufacturing, vol 148, 2021

[47] G. Bechtold, L. Ye, "Influence of fiber distribution on the transverse flow permeability in fiber bundles," Composites Science and Technology, vol. 63, no. 14, pp. 2069 – 2079, 2003

[48] X. Chen, T. D.Papathanasiou, "The transverse permeability of disordered fiber arrays: a statistical correlation in terms of the mean nearest interfiber spacing," Transport in Porous Media, vol. 71, no. 2, pp. 233– 251, 2008

[49] F. Gommer, A. Endruweit, A.C.," LongInfluence of the micro-structure on saturated transverse flow in fiber arrays," Journal of Composite Materials, vol. 52, no. 18, pp. 2463–2475, 2018

[50] K. Yazdchi, S. Srivastava, S. Luding, "Micro–macro relations for flow through random arrays of cylinders" Composites Part A: Applied Science and Manufacturing, vol. 43, no. 11, pp. 2007 – 2020, 2012

[51] J. Li, "Modeling, design and control of vacuum assisted resin transfer molding (VARTM) for thickness variation reduction," The Florida State University, 2006

[52] Ansys, I. N. C. "Theory reference, release 5.6.," ANSYS Inc., Canonsburg, 1997

[53] A. Wimshurst, "[CFD] Porous Zones in CFD," 2020, Video. Youtube. https://www.youtube.com/watch?v=sOQMXxoKFQM&t=648s&ab_channel=FluidMechanics101

[54]X. Yu , H. Wang, Z. Wang, "Analysis of yarn fiber volume fraction in textile composites using scanning electron microscopy and X-ray micro-computed tomography," Journal of Reinforced Plastics and Composites, vol. 38, no. 5, pp. 199-210, 2019

Appendix A:

	ULC	URC	BLC	BRC	Mean Scan 1 [mm]	Standard deviation Scan 1 [mm]	Mean Scan 2 [mm]	Standard deviation Scan 2 [mm]
Location 1	1.26%	0.30%	0.30%	0.04%	4.65	0.15	4.64	0.16
Location 2	0.04%	0.20%	0.00%	0.29%	4.67	0.20	4.66	0.20
Location 3	0.15%	0.15%	0.01%	0.12%	4.70	0.15	4.70	0.14
Location 4	0.88%	0.15%	0.52%	0.47%	4.69	0.14	4.72	0.13

*** Blue cells indicates the error between scan 1 and scan 2 for each quarter center node and corresponding location (see Fig. 3.6(c) and Fig. 3.7). Mean Scan 1 and Mean Scan 2 is the mean of Scan 1 and Scan 2 thicknesses of quarter center nodes for the given location. Standard deviations are the standard deviation of quarter center nodes for the given location.

Appendix B:

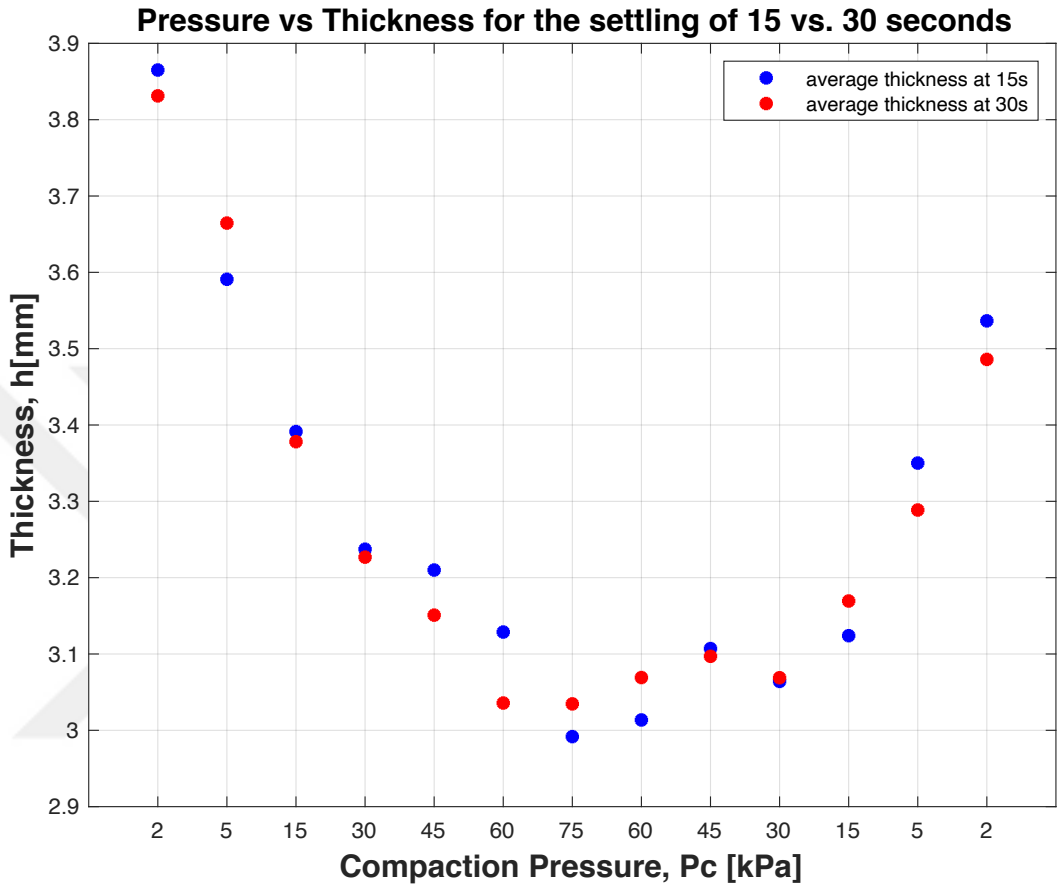

*** This graph shows that there is an error of maximum ~ 3% between the thickness of 15 seconds and 30 seconds of fabric settling time after pressure level changes. The thickness for a single pressure level may be higher either for 15 seconds or 30 seconds fabric settling time. It is uncertain but showing that there is a negligible error between 15 seconds and 30 seconds of fabric settling time in terms of measured thickness. As a result, 15 seconds of fabric settling time was used compaction characterization experiments.

Appendix C:

Pressure Level (kPa)	Error Between 15s and 30s Measurements (%)
2	-0.9
5	1.9
15	-0.3
30	-0.3
45	-1.5
60	-2.4
75	1.1
60	1.5
45	-0.3
30	0.1
15	1.2
5	-1.6
2	-1.3

How is the error computed:

$$Error = \frac{t_{30s} - t_{15s}}{t_{30s}} \times 100$$

Where;

t_{30s}: thickness for 30s scan
t_{15s}: thickness for 15s scan

- "−" indicates that 30s thickness lower that 15s thickness for that pressure level

*** This table shows the error between the average thicknesses measured for 15 seconds and 30 seconds fabric settling time at each pressure level for the results shown in Appendix B.